Barbara Lendl

Investigation of metal oxide nanolayers for highly selective gas sensors

MASTER THESIS

For obtaining the academic degree
Diplom-Ingenieurin

Diploma Programme of
Technical Physics

Graz University of Technology

Graz University of Technology

Supervisor:

Univ.-Prof. Dipl.-Ing. Dr.techn. Adolf Winkler

Institute of Solid State Physics

Graz, October 2010

Barbara Lendl

Investigation of metal oxide nanolayers for highly selective gas sensors

DIPLOMARBEIT

zur Erlangung des akademischen Grades
Diplom-Ingenieurin

Diplomstudium Technische Physik

Technische Universität Graz

Betreuer:

Univ.-Prof. Dipl.-Ing. Dr.techn. Adolf Winkler

Institut für Festkörperphysik

Graz, Oktober 2010

Abstract

Highly sensitive and fast gas sensors, which are able to operate in reducing and oxidizing atmospheres at high temperatures, are a major demand of the fuel cell industry today. To develop such a sensor system a new approach is used, consisting of gas sensing layers on top of a microbalance to increase the sensitivity. The gas sensing layers correspond to chemical gas sensors, based on semiconducting metal oxide nanolayers. For these layers two different concepts were designed and fabricated by the Austrian Institute of Technology (AIT) and the NanoTec Center Weiz (NTCW). One focus of the work at hand was to characterize and compare these two sensor-systems. The chemical gas sensors, developed by AIT, are made of SnO_2 layers, in the pure state as well as doped with antimony and indium. The sensor elements produced by NTCW are using WO_3 nanoparticles as sensing material on top of interdigital conductive paths. During this work also first tests have been conducted with MoO_3 nanoparticles, replacing the WO_3. The two different sensor concepts and different sensing materials were characterized at the AVL test bench under similar conditions, with respect to their sensitivity to hydrogen sulfide and water. The sensor response to 5 ppm H_2S was detected at temperatures between 100°C and 475°C. Comparable results concerning the sensors capability for the accurate and rapid detection of low concentrations of hydrogen sulfide were achieved. The WO_3 sensors developed by NTCW showed high sensitivities and extremely rapid response times to H_2S. However, a capability for water detection could not be proofed within the described measurements. The MoO_3 sensors on the other hand could not be measured due to sensor damages caused by the nanoparticle application process. The AIT sensors, made of pure SnO_2, $InSnO_2$ and $SbSnO_2$, showed reproducible but not reasonable responses to hydrogen sulfide. A sensitivity to humidity could not be detected in course of the characterization measurements. Additionally, the response to 2.5% H_2 was investigated for this sensor showing satisfying results.

For the integration of the chemical gas sensing layers on a piezoelectric microbalance special high temperature resonators were manufactured, made of gallium orthophosphate. To operate these resonators at temperatures up to 800°C, a high temperature sensor mounting was necessary, which was designed and fabricated by the Institute of Sensor and Actuator Systems of the Technical University Vienna. First tests were performed to characterize the oscillation behavior of assembled sensors from room temperature up to 800°C in air and in reducing atmosphere.

Zusammenfassung

Die Entwicklung von hoch sensitiven und besonders schnellen Gassensoren, welche sowohl in reduzierenden als auch oxidierenden Atmosphären und bei hohen Temperaturen eingesetzt werden können, ist ein großes Anliegen der Brennstoffzellenindustrie. In dieser Arbeit wird ein völlig neues Konzept beschrieben um ein solches Sensorsystem zu realisieren. Dazu werden gassensitive Metalloxidschichten auf einer piezoelektrischen Mikrowaage integriert. Chemische Gassensoren, genannt Chemiresistoren, bestehen bereits aus solchen halbleitenden Nanoschichten. Zwei unterschiedliche Sensorkonzepte bezüglich solcher Sensoren wurden vom Austrian Institute of Technology (AIT) und vom NanoTecCenter Weiz (NTCW) entworfen und hergestellt. Das Ziel dieser Arbeit lag unter anderem darin diese beiden Sensorsysteme zu charakterisieren und zu vergleichen. Die von AIT entwickelten Gassensoren bestehen aus SnO_2-Schichten, welche entweder in reinem Zustand oder mit Indium oder Antimon dotiert eingesetzt werden. NTCW verwendet WO_3-Nanopartikel als gassensitives Material. Diese werden auf interdigitalen Leiterbahnen platziert, wobei der Strom nur über die Nanopartikel geleitet werden kann. Zusätzlich zu den WO_3-Sensoren wurden im Laufe dieser Arbeit auch Messungen bezüglich der Eignung von MoO_3-Nanopartikel durchgeführt. Die zwei verschiedenen Sensorkonzepte und unterschiedlichen sensitiven Materialien von AIT und NTCW wurden am AVL Prüfstand unter gleichen Bedingungen charakterisiert. Das Augenmerk lag dabei auf der Detektion von H_2S und Wasser. Bei Temperaturen zwischen 100°C und 475°C wurden die Sensorreaktion auf 5 ppm H_2S registriert. Diese Messungen führten zu vergleichbaren Resultaten bezüglich der Eignung dieser Sensoren für die genaue und schnelle Detektion von geringen Konzentrationen von Schwefelwasserstoff. Die von NTCW entwickelten WO_3-Sensoren zeigten dabei sehr hohe Sensitivitätswerte und extrem schnelle Reaktionszeiten auf die Anwesenheit von H_2S im Gasstrom. Eine reproduzierbare Reaktion auf Wasser konnte mit diesen Sensoren während der beschriebenen Messungen aber nicht erreicht werden. Die MoO_3-Sensoren lieferten keine sinnvollen Meßergebnisse, da die Leiterbahnen während des Aufbringungsprozesses der Nanopartikel beschädigt worden waren. Die SnO_2-, $InSnO_2$- und $SbSnO_2$-Sensoren von AIT zeigten während der Messungen zwar reproduzierbare aber sehr unerwartete Reaktionen auf Schwefelwasserstoff. Eine Eignung dieser Sensoren zur Detektion von Wasser konnte während dieser Messungen nicht bestätigt werden. Zusätzlich konnte die Sensorreaktion auf 2,5% H_2 untersucht werden. Dabei konnten zufriedenstellende Sensorreaktionen beobachtet werden.

Um die gassensitiven Nanoschichten auf einer piezoelektrischen Mikrowaage zu integrieren, wurden spezielle Hochtemperaturresonatoren verwendet. Diese wurden aus Galliumorthophosphat hergestellt und ermöglichen einen Einsatz bei Temperaturen bis zu 800°C. Das Institut für Sensor- und Aktuatorsysteme der Technischen Universität Wien entwickelte eine spezielle Hochtemperatur-Sensorhalterung für $GaPO_4$-Resonatoren. Innerhalb dieser Arbeit wurden in diese Halterung eingebaute Kristalle bei Temperaturen von Raumtemperatur bis zu 800°C in Luft und in reduzierender Atmosphäre auf ihr Schwingungsverhalten hin untersucht.

Acknowledgments

This thesis has come into being with the support of several people. First of all I want to extend my grateful thanks to my supervisor Univ.-Prof. DI. Dr. Adolf Winkler, who had always time for advising and informative conversations. He helped me to see my work under different physical points of views and found solutions for various practical problems and theoretical considerations. Additionally, he supported me by structuring this work and improved the written thesis itself in many ways.

I want to thank DI. Dr. Peter Prenninger, who made it possible for me to write my diploma thesis together with AVL List GmbH. Additionally, he gave me good advice concerning the planning and performing of my experimental work. I also want to extend my thanks to Ing. Richard Schauperl, who was responsible for the project planning and execution. He led my steps and his advice was essential for the success of my work. I also want to thank Horst Kiegerl and Sabrina Windisch, who helped me building my experimental setup and solved some practical problems in the laboratory. Mag. Doris Schönwetter and DI. Dr. Gunther Weirum were so kind to review this work concerning the English language. My investigations concerning piezoelectric microbalances were strongly supported by Mag. Ferdinand Krispel from Piezocryst. He spent a lot of time to answer all of my questions.

This work was achieved with the help of three project partner companies. I want to thank Ao. Univ.-Prof. DI. Dr. Emil List and DI. Markus Postl from the NanoTecCenter Weiz for their fruitful cooperation. Especially Markus Postl was always very helpful when I needed advice concerning semiconductor chemical gas sensors. My collaborator from the Austrian Institute of Technology was Univ.-Doz. Mag. Dr. Anton Köck. He supported my work with great enthusiasm and was concerned to answer all of my questions. I also want to thank Ao. Univ.-Prof. DI. Dr. Werner Grogger, Sanja Simic and DI. Dr. Angelika Reichmann from the Center of Electron Microscopy (ZfE) for the excellent SEM pictures and EDX analysis presented in this work.

The very productive cooperation with the Institute of Sensor and Actuator Systems of the Technical University Vienna enabled the fabrication of a high temperature microbalance mounting. Therefore I want to extend my grateful thanks to DI. Dr. Walter Smetana and Ing. Heinz Homolka.

Table of contents

Part I: Basics

Part II: Research

Part III: Sensor design and measurements

Introduction

In the increasingly important development of fuel cells the detection of certain gas species plays a significant role. Well defined mixed gas atmospheres have to be provided to the fuel cell system. These oxidizing and reducing mixtures are generated by fuel reformers. To prevent damage of the fuel cells, the composition of these mixtures has to be monitored very precisely. If the hydrogen supply is achieved by the reformation of natural gas, hydrogen sulfide poses a severe menace to the fuel cell. H_2S acts as a catalytic poison [Dun06], which strongly decreases the catalyst activity and irreversibly damages the fuel cell. For H_2S protection a great amount of different absorber systems has already been developed. For example, the comparison of two possible absorber materials is described in [Ma05]. Yet these protection systems are missing a detection application to exactly determine the time period, after which the absorber is totally covered with H_2S. Until now, the absorber elements have only been replaced due to experience values. This procedure however is ineffective and accompanied with high costs. In addition to the detection of H_2S, also the water concentration in the according gas supply has to be monitored. Low temperature fuel cells need a certain amount of humidity at the cell membrane to guarantee optimum operation parameters. Water is also necessary to decrease the concentration of unburned carbon in the gas stream produced by fuel reformers.

Therefore the fuel cell industry demands for highly sensitive and rapid gas sensors with focus on the detection of hydrogen-sulfide and water. Chemical gas sensors consisting of gas sensitive nanolayers are very suitable for these applications. The sensors are using nano-scaled metal oxide conductive paths, which enable a measurable change in the materials conductivity caused by the presence of reducing or oxidizing gas species at the sensor surface. In this way very sensitive, small and extremely rapid sensor elements can be constructed. In comparison to these chemical nanosensors, common macrosensor systems show much larger geometries and also slower response times. Due to their dimensions, it also becomes difficult to position these macrosensors within the gas inlet system of the fuel cells.

Despite the benefits of semiconductor gas sensors, the major disadvantage is the low selectivity. Most reducing gases cause an increase of the sensors conductivity, while most oxidizing gases lead to a decrease. Thus an identification of the components in a gas stream cannot be achieved by using this sensing method. Much research has been carried out to increase the sensors selectivity. Most approaches enable the detection of one target gas by decreasing the cross sensitivities to other gas species. An overview of this kind of improvements can be found in chapter 3.

A completely new concept to increase the selectivity of chemiresistor gas sensors was developed by AVL List GmbH, the Austrian Institute of Technology AIT and the NanoTec Center Weiz NTCW. Additionally the Center of Electron Microscopy Graz (ZfE) was involved in the project, performing the microscopic analysis of the different sensor elements. The project involves the combination of semiconducting, gas sensitive nanolayers with a totally different sensing concept. Different sensing layers shall be integrated on a piezoelectric microbalance to allow the identification of different species by simultaneous detection of the layer conductivity and the mass changes due to the adsorbed molecules on the sensor surface. AIT and NTCW develop chemical gas sensors based on these semiconducting nanolayers. The sensor concepts differ according to their sensing materials and sensor geometries. Chapter 4 contains the design and fabrication methods of semiconductor gas sensors developed by AIT and NTCW. In the course of the project, these sensors were characterized at AVL under similar test conditions. In this way, comparable results containing the sensors sensitivity to hydrogen sulfide and water could be gained. The test parameters and results are described in detail in chapter 5. According to the application field in fuel cells, the sensors are intended to be suitable in temperature regions up to 800°C. Therefore a special material, developed by AVL and fabricated by the company Piezocryst, was chosen for the piezoelectric microbalances: Gallium orthophosphate has a similar crystal structure as quartz, but shows a stronger piezoelectric effect. While the piezoelectricity in quartz disappears at temperatures above 570°C, $GaPO_4$ can be used as a microbalance up to 970°C [Pie10]. To enable the appliance of these high temperature resonators at 800°C, a special sensor mounting was designed by the Institute of Sensor and Actuator Systems of the Technical University Vienna. The mounting concept is also described in chapter 4. The work at hand is a part of the development process to create a highly sensitive, highly selective and extremely rapid gas sensor system.

Part I: Basics

1. Metal oxide chemical sensors

Metal-oxide gas sensors have been used in a wide field of technical applications since the late 1960s. These sensors can be produced very cheaply and easily because of their simple electronic design. Metal oxides change their electrical resistance if they are exposed to reducing or oxidizing gases. A well known material for such chemiresistors is SnO_2.

When oxygen interacts with the gas sensitive material, it extracts electrons from the metal-oxide, which leads to a decrease of the electric conductivity. Reducing gases cause an electron injection into the sensor material. The result is an increasing conductivity.

1.1 Historical overview

Only a few chemical gas sensors had been known before the 1960s. In 1962 T. Seiyama [Sei62] and N. Taguchi [Tag62] simultaneously developed two semiconductor sensors for the detection of inflammable gases, which were not only designed for technical applications but also for the use in households. Chemiresistors have been commercially available since 1970 and rapidly became important devices in security applications. An early chemiresistor for the detection of oxygen was build of solid stabilized zirconia electrolyte and was prevalently used to control car emissions [Kiu57]. By adding Pt-electrodes to a CaO-stabilized zirconia tube it was possible to get a sensor response depending on the partial pressure of oxygen in various gas atmospheres at high temperatures. Thereby one electrode is exposed to O_2 while a reference electrode is placed in air. Another important field of application for chemiresistors was the detection of humidity. The first commercial sensor was introduced to the market in 1976 [Nit76]. It consisted of a porous composite of metal oxides. The sensing effect is a change of the AC impedance due to an increase of humidity at elevated temperatures. This development led to the manufacturing of many other humidity and dew point sensors, using ceramics or polymers as sensing material. The three mentioned sectors, sensing of inflammable gases, oxygen and humidity are the applications mostly incorporated in our daily life until now. [Yam07]

1.2 Gas adsorption on solid surfaces

The most important value for expressing adsorption of gas atoms or molecules on a solid surface is the sticking coefficient. Not every particle, arriving at the surface, is adsorbed. The sticking coefficient or sticking probability s is an indicator for the amount of adsorbed particles per impinging particles. It is a function of the coverage of the surface Θ, the condensation coefficient σ and the activation barrier for adsorption E_{act}:

$$s = \sigma \cdot f(\Theta) \exp\left(\frac{-E_{act}}{kT}\right) \qquad (1.1)$$

The function of the coverage f(Θ) is given by (1–Θ) for a non-dissociative adsorption and by (1- Θ)² for most cases of dissociative adsorptions. Generally the sticking coefficient depends on the nature of the adsorbate, the kind of solid and surface and the temperature. A simple scheme to describe adsorption processes is the Langmuir adsorption model. Therein three assumptions are made:

- Adsorption only leads to one monolayer of adsorbates on the surface
- All adsorption sites are equivalent
- Each adsorption site can only contain one adsorbed particle

The adsorption of gas atoms or molecules on a solid surface can be divided into two kinds according to the type of bond. A bonding caused by only intermolecular forces with binding energies in the range of 0.5 eV is called physisorption. This type of bond occurs due to Van-der-Waals interaction. With increasing temperature the physisorption rapidly decreases. Physisorption is a reversible process. At higher temperatures a different type of bond is responsible for gas adsorption, which is called chemisorption. In this case the molecules are bonded by chemical forces, which can also be relatively low. Thereby the bonding between the atoms in the adsorbate molecule is often weakened or even breaks, which makes it necessary to overcome an activating barrier. Because the thermal energy is often too small for activation, chemisorption can only occur at higher temperatures. The binding energy of chemisorption lies in the range of 1 eV. For this reason chemisorption is mostly an irreversible process at low temperatures. Chemisorption always leads to a monolayer of adsorbed particles on the solid surface. [Wei89, Ber05, Our03]

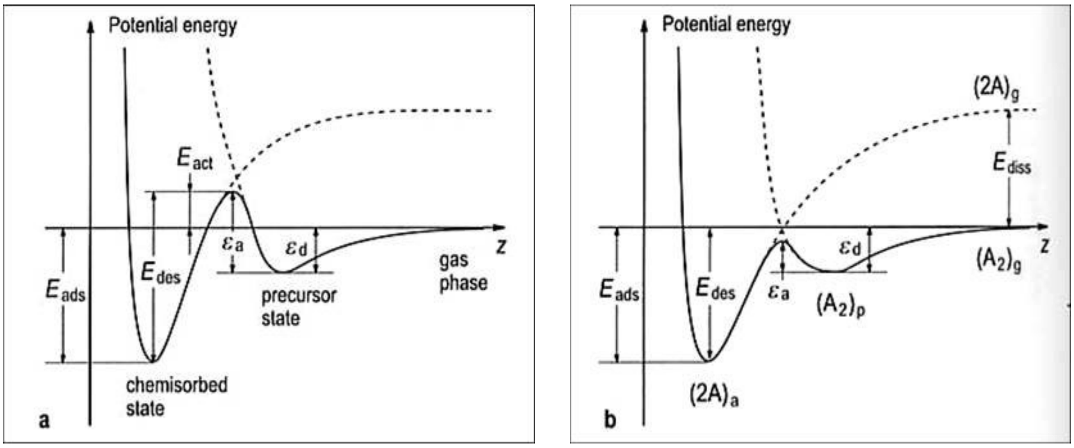

Figure 1.1: Lennard-Jones potential for (a) an activated adsorption and (b) a non-activated adsorption [Our03]

Figure 1.1 shows the potential for physisorption and chemisorption. Often a gas molecule first gets weakly bound by physisorption, what is here called the precursor state. The *z*-direction is the distance from the solid surface. The temperature dependent sticking coefficient s_0 for the activated and the non-activated adsorption is in both cases given by:

$$s_0 = \left[1 + \frac{\nu_d}{\nu_a} \exp\left(-\frac{\varepsilon_d - \varepsilon_a}{kT} \right) \right]^{-1} \tag{1.2}$$

Where *v* is the attempt frequency for adsorption and desorption. If the temperature of the system is increased the sticking coefficient for the activated adsorption increases too, while s_0 for the non-activated adsorption decreases. In the case of activated adsorption the adsorbed particle has to overcome the activation barrier. Therefore the kinetic energy has to be high enough. The sticking coefficient increases with the kinetic energy. If precursor adsorption takes place the sticking coefficient decreases with increasing E_{kin}. [Our03]

Chemisorbed particles mostly arrange on a surface in regular, two-dimensional structures. If the surface is irregular or contaminated the biggest amount of chemisorbed particles will be found at so called active centers. These centers can be edges, point defects and positions close to already adsorbed particles. Active centers can be different for various kinds of adsorbates. If chemisorption takes place on semiconductors or isolators also electrons and defect electrons, located on the surface, can act as active centers. This behavior is called the Wolkenstein theory [Wei89]. Therefore chemisorption leads to a change in the electron distribution in a surface layer, meaning a change in the energy-band model. Recapitulatory the adsorbing process strongly depends on the kind of the adsorbing particles, the surface structure of the solid and the operating temperature. [Wei89, Ber05]

1.2.1 Adsorption on metal oxides

Metal oxides can offer two different kinds of adsorption sites: positively charged metal ions are acting as Lewis-acidic adsorption sites and negatively charged oxide ions show a basic behavior. The adsorption properties at oxide surfaces are defined by the character and number of surface defects. At low temperatures in ambient air the metal oxide surface is totally coated with physisorbed water molecules. This layer desorbs with increasing temperature.

To describe the adsorption of gas molecules on a metal oxide surface one can look at the band model of semiconductors. The surface of a semiconductor is a disturbance of the periodic lattice potential and therefore generates space charges, which can not be compensated by electrons or defect electrons. Therefore it is not longer possible to speak of a neutral solid state body. For a perfectly plane and clean surface in vacuum the electric potential caused by the space charge leads to a surface band, which is placed between the valence band and the conduction band. The number, energy and character of these surface levels are strongly depending on the water molecules and foreign atoms on the surface. The occupation of the surface levels is responsible for more or less positive or negative charges at the surface. To compensate these charges an exponentially decreasing space charge occurs inside the semiconductor, which leads to band bending at the surface. Charge carriers with the same prefix are urged inside the solid while carriers with opposite prefix are dragged to the surface. This space charge layer usually has a thickness in the range of one Debey-length [Wei89] and increases with decreasing charge carrier density of the semiconductive material. The Debey-length defines the distance from an electron, in which its potential drops to 1/e.

If adsorption takes place at the semiconductor surface, the adsorbed atoms can ingest electrons from the surface. These electrons are provided by donators next to the surface. Generally the surface of the semiconductor thereby stays neutral. The number of electrons at the surface decreases. Therefore band bending occurs near the surface, which leads to a different work function $q\Phi_S$ between the vacuum energy E_{Vak} and the Fermi energy E_F. The vacuum energy describes the energy of an electron in vacuum close to the solid surface.

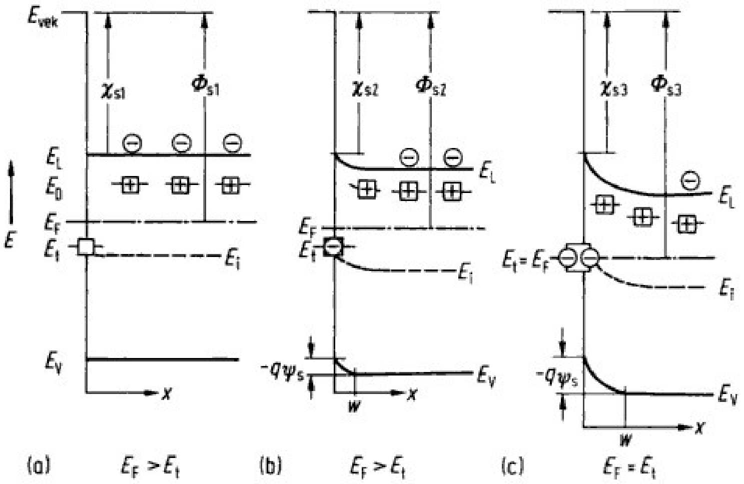

Figure 1.2: Semiconductor surface with adsorbed particles. (a) before the adsorption; state of equilibrium (b) not reached and (c) reached. [Kas05]

As can be seen in Figure 1.2 the electron energy level of the adsorbed particle E_t also gets displaced when the bands are bended at the surface. If the adsorbed atom ingests electrons from the surface, it acts as an acceptor. With increasing density of adsorbed particles a continuous increase of the band bending appears until a state of equilibrium is reached ($E_F = E_t$). This reaction can only be seen, if the electron energy level of the adsorbed atom lies beneath the Fermi energy at the beginning. If E_t becomes bigger than E_F the probability of occupation decreases. Therefore the gas atoms stop ingesting electrons but release them to the surface.

In Figure 1.2 it can also be seen that the work function $q\Phi_S$ changes with increasing number of adsorbates while the electron affinity X_S remains constant. [Wei89, Kas05]

1.2.2 Adsorption of hydrogen sulfide

Hydrogen sulfide is a strongly reducing gas. At semiconductor surfaces the sulfur atoms are bound to the metal atoms by σ-bonds. Additionally also π-bonds are possible. The plane of the hydrogen sulfide molecule is almost parallel to the surface. Figure 1.3 shows the adsorption of a H_2S molecule on a metal surface, which is quite similar to those on metal oxide surfaces.

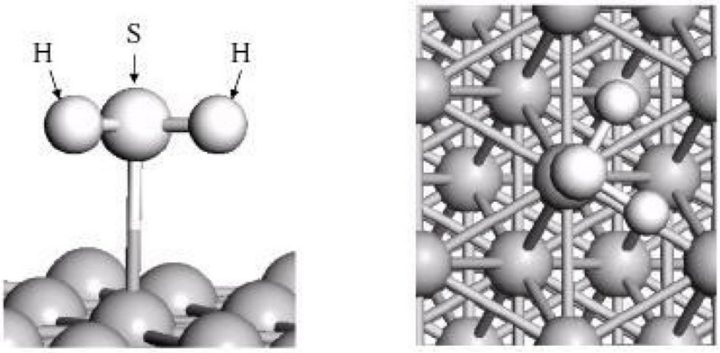

Figure 1.3: Position of an adsorbed hydrogen sulfide molecule on a metal surface [Alf08]

At temperatures below 400 K the whole H_2S molecule binds to the surface like in Figure 1.3. Additionally reactions like the following can appear:

$$2H_2S_{(gas)} + 3O^-_{2(ads)} \longleftrightarrow 2H_2O + 2SO_2 + 3e^- \tag{1.3}$$

If the temperature lies above 400 K, adsorbed H_2S molecules dissociate at the surface. This process causes the creation of HS- and OH-groups, as illustrated in Figure 1.4. [Rey06]. Dissociation is possible because the sulfur atoms are bound to the surface by a strong valence bond. In contrast the hydrogen bond is rather weak. Sulfur mostly adsorbs at lattice sites with high coordination. On fcc(100) surfaces they are four times coordinated and on fcc(111) surfaces three times. Due to the strong bond between the adsorbants and the metal oxide atoms the binding distances between the surface atoms can be changed. This may lead to a reconstruction of the surface. [Ber05]

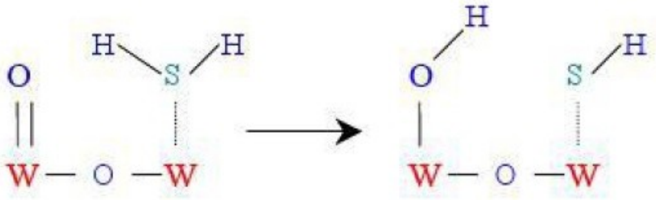

Figure 1.4: Adsorption of H_2S on tungsten oxide and following dissociation [Gal03]

The hydroxyl groups built by the dissociation process are acting as initial points for co-adsorption of other H_2S molecules. Hydrogen sulfide can desorb again by recombining to H_2S and SO_2:

$$2HS_{(ads)} + 2O_{(lattice)} \longrightarrow H_2S_{(gas)} + SO_2 \tag{1.4}$$

Another reaction, which appears when H_2S is adsorbed at a surface at high temperatures, is:

$$H_2S_{(ads)} + O^-_{(ads)} \longleftrightarrow H_2O + S + e^- \tag{1.5}$$

This reaction and the one described in formula 1.3 are only possible if enough oxygen ions are available at the surface. These ions can be created by two different reactions depending on the temperature:

$$\text{below 400 K:} \quad O_{2(gas)} + e^- \longleftrightarrow O^-_{2(ads)} \qquad (1.6)$$

$$\text{above 400 K:} \quad O_{2(ads)} + e^- \longleftrightarrow 2O^-_{(ads)} \qquad (1.7)$$

These reactions cause a thin electron-depleted layer at the surface of the metal oxide. When hydrogen sulfide is adsorbed at the sensor, electrons are injected into the conduction band and the sensor conductivity increases. [Rey06]

1.2.3 Adsorption of humidity

Surfaces under normal atmospheric conditions are always covered with several monolayers of water. Water is adsorbed at a surface in a hexagonal double layer structure. The molecules are connected to each other by hydrogen bonds. Only at very low temperatures it is possible to adsorb single water molecules. The lone pair 2p-orbitals of the oxygen atoms bind to the surface atoms. The plane of the water molecule and the surface normal draw an angle α, which can vary between 55° and 90°, depending on the solid material. [Gie05]

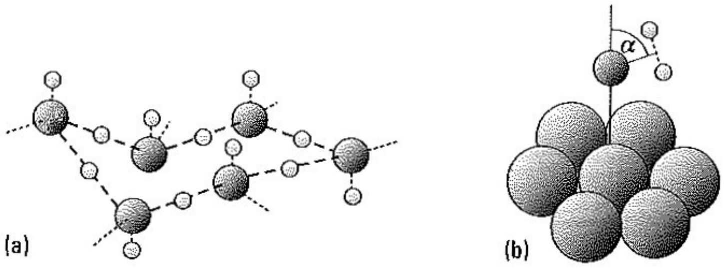

Figure 1.5: (a) Hexagonal double layer structure of water on a surface; (b) binding angle α of one water molecule [Gie05]

The adsorption of water molecules on metal oxide surfaces can take place in three different ways. Figure 1.6 shows a H_2O molecule which is directly bound to a metal ion in the surface (a). Such a water molecule is a strong adsorption center itself. (b) shows a directly bond OH-group, while (c) demonstrates an OH-group at an oxygen lattice site. Such OH^-groups, called hydroxyl groups, are created by the interaction and dissociation of water molecules with metal ions of the surface. The remaining H^+ ions unite with the oxygen ions of the surface. In case (d) one can see an OH-group binding to a water molecule with a hydrogen bonding.

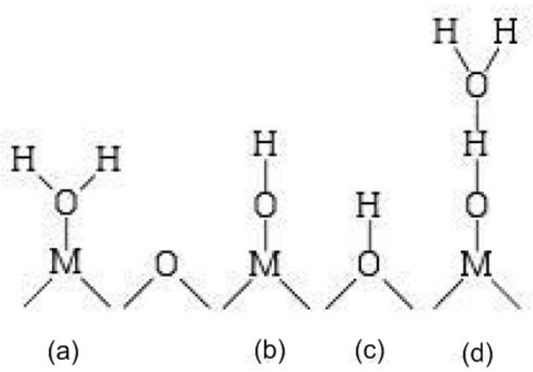

Figure 1.6: Different ways of water adsorption on a metal oxide surface [Poh00]

At temperatures below 200°C the H_2O adsorption by hydrogen bonding is the most probable one. Most adsorption reactions take place at coordinatively unsaturated metal ions. Already adsorbed OH-groups are acting as docking units for other water molecules. In this way the surface is soon covered with several layers of molecular water.

If hydroxyl groups are created at the surface, adsorption reaches a state of saturation when the whole surface is covered. If the surface is only partially covered with hydroxyl groups other particles are more likely adsorbed. This behavior is called co-adsorption. Other particles can be easily adsorbed at the OH-groups by hydrogen bonds. If these groups are already covered, an additional gas adsorption can systematically be prevented. Because the creation of a hydroxyl group is an interaction with the oxygen lattice atoms, it leads to an oxygen vacancy. These gaps are filled up again by chemisorbing oxygen out of the surrounding gas atmosphere. [Poh00, Mad89]

1.2.4 Adsorption of hydrogen

The binding of hydrogen to a solid surface is covalent. On transition metals adsorption occurs without a measurable activation barrier. Because of the very small mass of hydrogen the atoms are moving with very high oscillation amplitude. Therefore the movement of a hydrogen atom has to be described quantum mechanically as a wave packet. The vibration states are space delocalized band states. Therefore diffusion at low temperatures mostly occurs due to a tunneling process. The delocalization of deuterium is much lower because of its larger mass. [Gie05]

At temperatures between 100°C and 300°C H_2 directly reacts with adsorbed oxygen at the metal oxide surface and produces water molecule:

$$2H_2 + O_2^- \longleftrightarrow 2H_2O + e^- \tag{1.8}$$

$$H_2 + O^- \longleftrightarrow H_2O + e^- \tag{1.9}$$

$$H_2 + O_2^- \longleftrightarrow H_2O + 2e^- \tag{1.10}$$

At higher temperatures H_2 molecules can dissociate. The reaction of the hydrogen atoms with adsorbed oxygen again leads to the creation of water molecules [Gon04].

1.2.5 Desorption from solid surfaces

If the adsorbed phase and the gas phase are in an equilibrium state the numbers of adsorbed and desorbed particles are equal. The number of particles impinging onto a surface in a certain time and area can be calculated by using the kinetic gas theory. Equation 1.11 shows that the impinging rate r_{imp} depends on the pressure p, the mass of the particles m, the Boltzmann constant k_B and the temperature T.

$$r_{imp} = \frac{p}{\sqrt{2\pi m k_B T}} \tag{1.11}$$

The true number of particles adsorbed at the surface now depends on the sticking coefficient. By knowing this parameter the desorption rate at equilibrium can be defined:

$$r_{des} = r_{ads} = s(\Theta, T) \cdot \frac{p}{\sqrt{2\pi m k_B T}} \tag{1.12}$$

The pressure can also be expressed by the chemical potential and the whole equation can be referenced to the area of one surface atom. r_{des} therefore consists of an exponential term and a pre-exponential element. Generally the desorption rate can be approximated in the following way by the Polanyi-Wigner equation:

$$r_{des} = \Theta^n \cdot \nu_n(T) \cdot e^{-\frac{E_{des}}{kT}} \tag{1.13}$$

Where n stands for the kinetic order of desorption. The factor is 1 if atoms or molecules are desorbing directly from the surface. If two atoms are recombining during desorption the factor n has a value of 2. n=0 is possible if the desorption induces an autocatalytic process, desorption is not coverage dependent at a defined temperature or the surface is covered with a 2D two-phase system.

The desorption energy E_{des} is calculated otherwise according to the different kinds of adsorption. In the case of activated adsorption E_{des} is the sum of the adsorption energy E_{ads} and the activation energy E_{act}. If the adsorption occurs non-activated, E_{des} can be equated with E_{ads}. These declarations can easily be understood by looking at Figure 1.1. If adsorbed particles are interacting with each other, the desorption energy depends on the coverage.

Adsorption and desorption are connected by the Principle of Detailed Balancing. This means that if particles with high energy are adsorbed more likely, the desorption probability for highly energetic particles is also larger. Additionally the incidence angle with the highest adsorption probability will also show the largest desorption flux. [Gie05, Ren94]

1.3 Electrical conductivity of metal oxides in certain gas atmospheres

The sensing principle of chemiresistor gas sensors is a measurable change of the electrical conductivity in the presence of oxidizing or reducing gases at the sensor surface. Therefore the conductivity of metal oxides in special gas atmospheres is described below in more detail.

1.3.1 Conductivity changes of chemical gas sensors

The presence of certain gases at the surface of the sensing material causes changes in the electrical conductivity of the sensor. On the one hand this effect is caused by a partial charge transfer between the adsorbed atoms and the surface due to chemisorption and on the other hand by surface reactions with oxygen ions. The conductivity is strongly affected if oxygen vacancies are generated or annihilated. For this reaction it is important to have enough oxygen atoms available at the surface and that the mobility of the oxygen vacancies is high enough. If this mobility is rather small, the conductivity change occurs due to adsorption effects, like charge transfer or band bending.

If metal oxides are exposed to air, oxygen atoms are adsorbed at the oxide grains as anions and act as receptors. These oxygen anions lead to a space charge layer on the surface as it is described in chapter 1.2.1. If a reducing test-gas is applied to the sensing material, the adsorbed oxygen leaves the surface until a steady state level is reached. This reaction causes a decrease in the work function of the sensing material. The difference in the number of oxygen vacancies is directly connected to the change of conductivity.

For the transport of electrons through a grain barrier a double Schottky boundary has been assumed. Therefore changes in the barrier height lead to changes in the electrical conductivity of the material. If the grain diameters are bigger than a critical size D_c, the resistance and also the gas sensitivity of a sensing material is nearly independent of the grain size. The critical grain size is defined by twice the thickness of the surface space charge layer, which for example in the case of tin dioxide has a value of 6 nm. If the grain size is smaller than D_c the electrical resistance and the gas sensitivity strongly increase. Additional to this model an electron transport caused by the tunneling effect is possible.

When gas atoms are adsorbed at the surface, some of them can also diffuse into the solid. Yet if most reactions take place near the surface, the gas atoms can not reach the grains inside the solid. This causes a loss of the sensor response. Investigations about this characteristic have shown that the depth profile of the gas atmosphere atoms in the solid strongly depends on a factor m. This dimensionless factor is defined by:

$$m = L \cdot \sqrt{\frac{k}{D_k}} \tag{1.14}$$

Where L is the thickness of the sensing material, k defines the rate constant of the surface reaction and D_k names the Knudsen diffusion coefficient.

If *m* is smaller than 1 most of the gas atoms are diffusing through the whole sensing material layer. At bigger values of m, like *m*>3, the gas atoms only interact with the surface atoms. The depth profile of a thin sensing layer, according to different values of *m*, is demonstrated in Figure 1.7. *x* defines the depth considered from the surface of the sensing material. The gas concentration at a depth *x* is indicated with *C*, while the gas concentration outside the solid in the gas atmosphere is named C_S.

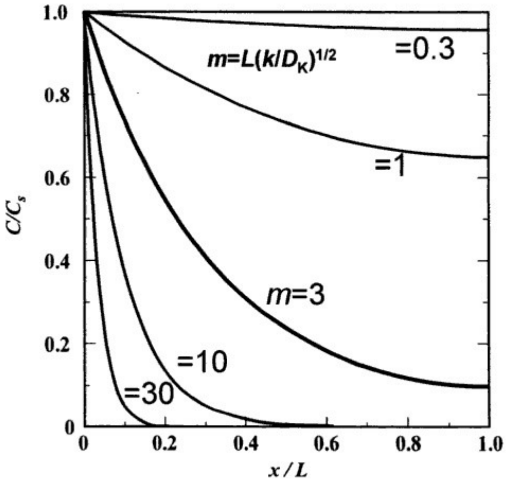

Figure 1.7: Gas concentration profiles depending on the value of factor *m* [Yam07]

The operating temperature of a chemical gas sensor also strongly influences the sensor response. At higher temperature also the rate constant *k* increases, whereas the Knudsen diffusion coefficient D_k rises proportionally to the square root of the temperature. Therefore the factor m increases nearly exponentially due to a temperature increase. In Figure 1.8 the relationship between the sensor response and the operating temperature is demonstrated for varying thickness of the sensing layer.

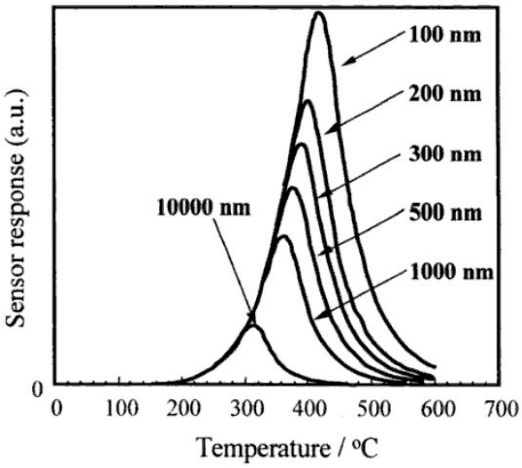

Figure 1.8: Temperature dependence of the sensor response of different layer thicknesses [Yam07]

This figure also demonstrates the shift of the maximum sensor response to higher temperatures by using thinner sensing layers. Additionally these thinner layers even lead to much higher sensor responses. [Yam07]

1.3.2 Chemiresistors in certain gas atmospheres

- **Hydrogen sulfide:**

Two different reactions of hydrogen sulfide with adsorbed oxygen atoms are probable, as mentioned in chapter 1.2.2:

$$H_2S_{(ads)} + O^-_{(ads)} \longleftrightarrow H_2O + S + e^-$$

$$2H_2S_{(gas)} + 3O^-_{2(ads)} \longleftrightarrow 2H_2O + 2SO_2 + 3e^-$$

These reactions cause the production of electrons, which leads to a decrease of the sensor resistance. Additionally the hydrogen sulfide can react with oxygen of the solid and therefore cause oxygen vacancies. The oxygen is removed from the solid lattice and thereby injects electrons to the sensing material [Rey06]. The according reaction is illustrated below:

$$2HS_{(ads)} + 2O_{(lattice)} \longrightarrow H_2S_{(gas)} + SO_2$$

- **Humidity:**

The adsorption of water on a metal oxide surface, described in chapter 1.2.3, causes a charge transfer between the water molecule and the surface atoms. This leads to an increase of the negative space charge layer at the surface and therefore to an increase of the sensors conductivity.

$$H_2O_{gas} \rightarrow H_2O_{ads} \rightarrow H_2O^{\delta+}_{ads} + \delta e' \tag{1.15}$$

If an adsorbed water molecule is dissociated, a hydroxyl group directly bound to a metal ion will be created. The remaining hydrogen atom interacts with a surface atom and creates a hydroxyl group at an oxygen lattice side. In this way an oxygen vacancy is generated. Also an adsorbed hydrogen atom and an adsorbed oxygen atom can build a hydroxyl group adsorbed at the surface [Mad89].

$$H_{ads} + O_{ads} \rightarrow OH_{ads} \tag{1.16}$$

- **Hydrogen:**

Depending on the operating temperature H_2 interacts with adsorbed oxygen at the surface in molecular or atomic form. Both reactions lead to the creation of water molecules and therefore to oxygen vacancies, which increases the electrical conductivity of the metal oxide. Additionally the resistance is decreased due to an increase of electrons, produced by the interactions mentioned in chapter 1.2.4 [Gon04]:

$$2H_2 + O_2^- \longleftrightarrow 2H_2O + e^-$$

$$H_2 + O^- \longleftrightarrow H_2O + e^-$$

$$H_2 + O_2^- \longleftrightarrow H_2O + 2e^-$$

1.3.3 Important parameters of chemiresistor gas sensors

The way a chemical gas sensor is reacting to a certain gas atmosphere depends on the sensor material (n-type or p-type semiconductor) and the gas species (reducing or oxidizing). A typical sensor response due to the presence of a certain gas atmosphere is illustrated in Figure 1.9. The measured variable thereby is the resistance of a sensing layer. [Kau07]

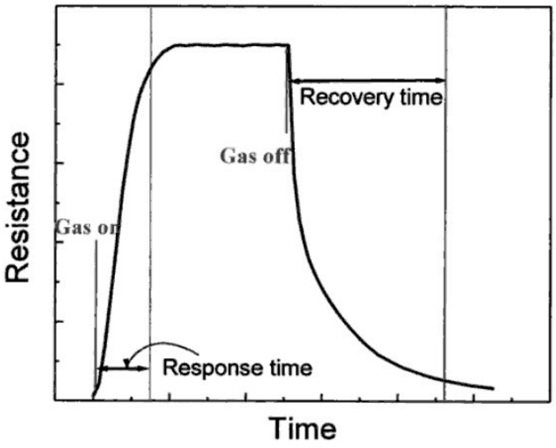

Figure 1.9: Typical resistance signal of a chemiresistor in a certain gas atmosphere [Kau07]

The response signal of a chemiresistor is described by the following five parameters:

- **Sensitivity:**

There are several possibilities to define sensitivity but usually one chooses between the following two methods:

a) A comparison of the sensor resistance in a reference gas (mostly air) and in the gas to be analyzed. Good gas sensors show high values of S.

$$S = \frac{R_{air}}{R_{gas}} \tag{1.17}$$

b) The second way to define sensitivity is to use a signal to background ratio indicated in percent.

$$S = \frac{R_{air} - R_{gas}}{R_{air}} \cdot 100 \quad [\%] \tag{1.18}$$

If R_{gas} is bigger than R_{air} the components of the numerator can be converted to get a positive value for the sensitivity. Otherwise the prefix of S defines the direction of the resistance change.

- **Response time:**

This value defines the time the response signal needs to reach a certain percentage of the final resistance in the gas atmosphere to be analyzed. The percentage value can be chosen individually. The most common definition works with a value of 90%. The quality of a gas sensor increases with decreasing response time.

- **Recovery time:**

When the sensor is again exposed to the reference gas, as for example air, the resistance will again come up to the value before the analyzing gas period. The recovery time defines the time until the signal has reached 90% of its background signal again. This parameter is very important because it indicates the dead time of the sensor. Therefore the recovery time should be very small.

- **Selectivity:**

A chemiresistor reacts to the presence of different gas species in a certain atmosphere. To define a value for the selectivity of a special gas species one can use the ratio of the sensor sensitivity for an interfering gas and the sensitivity towards the desired gas.

- **Long term stability:**

This parameter gives information about the duration a sensor can work without showing a drift of the four other parameters. Good sensors can work stably in unfavorable environments for several years. [Kau07]

1.4 Measuring methods

1.4.1 Electrical conductivity and specific resistivity

The electrical conductivity $\vec{\vec{\sigma}}$ describes the connection between the current density $\vec{j}$ and the electrical field strength $\vec{E}$. The according relation is called Ohms law:

$$\vec{j} = \vec{\vec{\sigma}} \cdot \vec{E} \tag{1.19}$$

Generally $\vec{\vec{\sigma}}$ is a tensor, but in many cases the conductivity can be regarded as a scalar. The electrical conductivity can be described by the Fermi surface, the velocity and the time of flight of the charge carrier. By using these parameters one can get to following expression for σ:

$$\sigma = q \cdot n \cdot \mu \tag{1.20}$$

n defines the charge carrier density, while q stands for the electrical charge. The charge carrier mobility μ is defined by:

$$\mu = \frac{q \cdot \tau}{m} \tag{1.21}$$

μ depends on the mean time between collisions τ, the electrical charge and the effective mass m.

The electric conductivity in a semiconductor consists of parts according to the electrons and to the holes, because both types of charge carrier contribute to the effective conductivity of the material:

$$\sigma = \sigma_n + \sigma_p = e \cdot n \cdot \mu_n + e \cdot p \cdot \mu_p \tag{1.22}$$

Where n and p stand for the density of the electrons and holes and e defines the electrical charge of an electron. [Wei89]

A characteristic property of an electrical device is its resistance. It is influenced by the geometry and the material. For a certain material it is possible to state the according specific resistivity ρ. This property can be calculated by the electrical field strength E and the current density j:

$$\rho = \frac{E}{j} \tag{1.23}$$

Therefore ρ is reciprocal to the electric conductivity σ: $\sigma = \frac{1}{\rho}$ (1.24)

In another definition the specific resistivity depends on the mean time between collisions τ, the charge q, the electron mass m and the number of conduction electrons per unit volume n:

$$\rho = \frac{m}{n \cdot q^2 \cdot \tau} \tag{1.25}$$

In order to calculate the resistance R of a conductor by knowing the specific resistivity of the material, the cross sectional area a and the length l of the device, the following equation can be used [Fra04]:

$$R = \rho \cdot \frac{l}{a} \tag{1.26}$$

1.4.2 Metal, semiconductor and insulator

The separation of materials in insulators, semiconductors and metals can be explained by considering the band model. The valence band is defined as the highest occupied energy band at the absolute zero point and always lies beneath the conduction band. This band is defined as the lowest energy band containing unoccupied states. If the conduction band is empty the Fermi energy is always located between the valance and the conduction band.

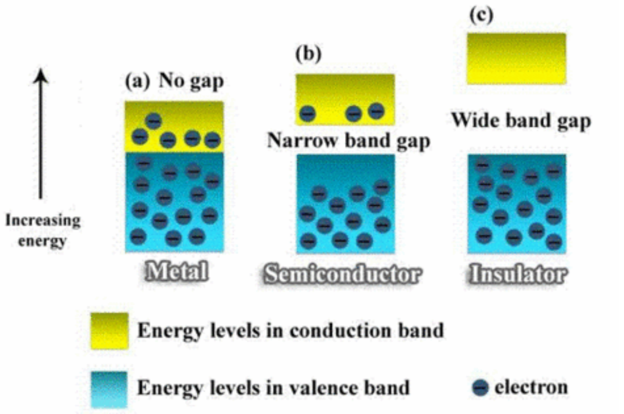

Figure 1.10: Energy bands of (a) metals, (b) semiconductors and (c) insulator [physicaplus.org.il]

The most important declaration concerning the conductivity of a material is that no current can appear in fully occupied bands. Therefore it would be necessary to lift electrons from the valence band to higher energy levels in the conduction band. In materials called insulator, this mechanism is impossible because the gap between the two bands is too big for the electrons to be excited. If the band gap is smaller we speak of semiconducting materials. In this case high temperatures or high electric fields can lead to electron excitation.

Metallic materials show a different band occupation. The conduction band is always partially filled with electrons. An overlapping of the bands is also possible. Therefore metals always show an electrical conductivity, even at very low temperatures.

If the band gap is small enough, electrons can be thermally excited to the conduction band and thereby increase the conductivity of the material. This effect leads to unoccupied energy levels in the valence band. These holes can be filled with other electrons from the valence band. In this way also the electrons of the valence band contribute to the electrical conductivity of the semiconductor. Such materials are called hole conductors. [Wei89]

1.4.3 Doped semiconductors

The word “doping” describes the implantation of foreign atoms into a defined lattice structure. These atoms change the concentration of free charge carriers in the crystal and therefore influence the conductivity. In semiconductors, doping is a common method to change electrical properties of the materials.

Foreign atoms produce local imperfections in the lattice. For example, we consider a phosphor atom implanted into a silicon lattice. The phosphor atom provides one electron which is not necessary for the covalent bonding with the silicon atoms. The other four valence electrons are strongly bound to the silicon lattice, which leads to a weak bonding between the phosphor atom and the electron. The electron can easily be excited into the conduction band and increases the conductivity. Doped atoms which inject electrons to the conduction band are called donators.

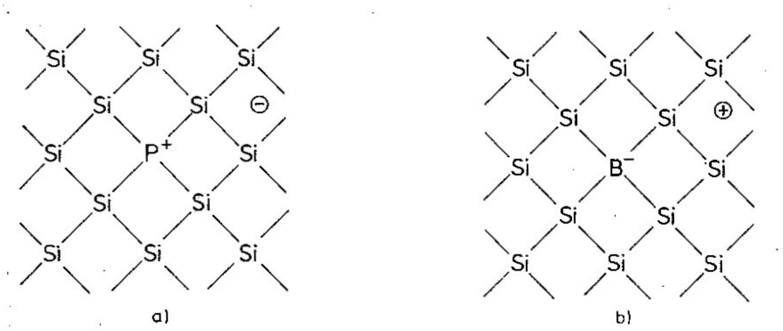

Figure 1.11: Silicon lattice doped with (a) phosphor atom or (b) boron atom [Wei89]

A second possibility is the doping of a silicon lattice with for example a boron atom. This atom misses one electron for the covalent bonding with the silicon atoms. The hole in the valence band will be filled by an electron of a nearby silicon atom. In this way a mobile defect electron has been generated. Such imperfections in the crystal lattice are called acceptors. [Wei89]

1.4.4 Limitation of electrical conductivity

The electrical conductivity can never become infinite because the charge carriers are always scattered at so called scattering centers. Several different factors can act as such scattering centers, like phonons, ionized and neutral lattice imperfections, point defects, dislocations, grain boundaries and other charge carriers.

At temperatures above room temperature the scattering caused by phonons is the most probable effect. With decreasing temperature the influence of ionized lattice imperfections increases, while at very low temperatures neutral imperfections are dominating. [Wei89]

1.4.5 The Hall effect

This effect enables the detection of the charge carrier mobility μ. If a current is applied to a metal plate and acts over its whole cross sectional area, no potential difference between the two points *A* and *B* illustrated in Figure 1.12 can be detected.

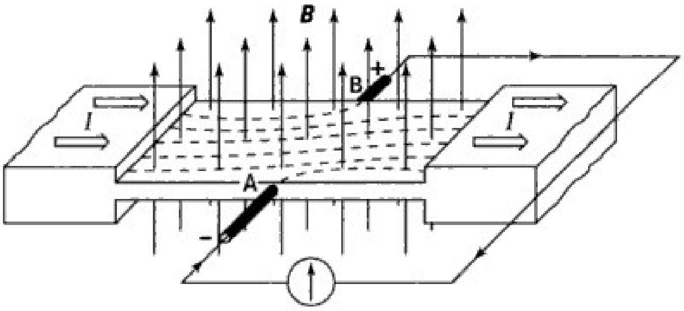

Figure 1.12: Configuration for the detection of the Hall Effect [Rai99]

If a magnetic field *B* is applied normal to the metal plate, the so called Hall voltage U_H can be measured between the two points, because the paths of the electrons in the plate are deformed due to the magnetic field. *B* causes a redirecting force called *Lorentz force*, which is given by:

$$F = -e \cdot v_{dr} \cdot B \tag{1.27}$$

where v_{dr} stands for the drift velocity of the electrons. The electron paths are deformed until a force according to the transversal electric field strength is big enough to compensate the effect. The according equilibrium condition is given by:

$$\frac{-e \cdot U_H}{b} = -e \cdot v_{dr} \cdot B \tag{1.28}$$

The factor *b* defines the width of the metal plate. By using the definition for the current density *j* in this measurement configuration $j = I/(b \cdot d) = -e \cdot n \cdot v_{dr}$ (*n*...electron density), the Hall voltage can be written as:

$$U_H = v_{dr} \cdot B \cdot b = \frac{j}{-e \cdot n} \cdot B \cdot b \tag{1.29}$$

According to the relationships mentioned above and the definition of the Hall coefficient $A_H = 1/(-e \cdot n)$, the Hall voltage U_H can be described by the following equation:

$$U_H = R_H \cdot I = \frac{A_H \cdot B \cdot I}{d} \tag{1.30}$$

R_H is the Hall resistance, A_H the Hall coefficient und d stands for the thickness of the plate. The Hall coefficient varies for different materials and can have positive or negative values. The Hall voltage is proportional to the drift velocity of the electrons and therefore also to the mobility μ. [Rai99]

1.4.6 Four point method

To measure the electrical surface resistivity of a semiconducting material with the common two point method, which corresponds to the classic Hall configuration without using a magnetic field, is often not suitable because of large contact resistances. An alternative measurement method is the so called “four point method”. Four test prods, illustrated in Figure 1.13, are arranged in one line on the material to be measured.

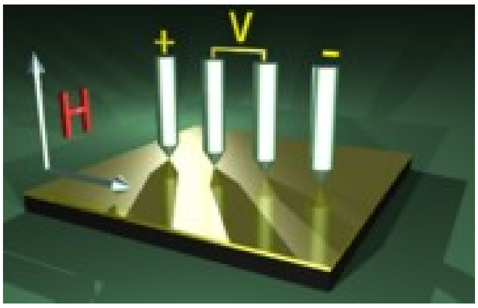

Figure 1.13: Arrangement of test prods according to the four point method [Wik10]

A defined current is applied between to two outer test prods and the potential difference between the inner ones can be detected. This voltage signal is independent of contact resistances because the internal resistance of the voltmeter is much higher. [Wik10]

The four point method in electrical circuits is demonstrated Figure 1.14.

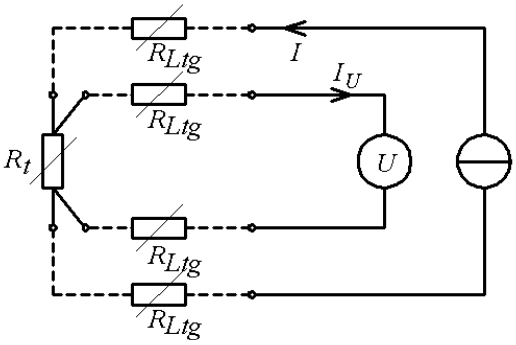

Figure 1.14: Electrical circuit for four point measurement, R_t marks the resistance to be investigated [Wik10]

If the test prods are located in exactly the same distances to each other, the specific resistivity ρ of a material can be calculated by:

$$\rho = \frac{\pi}{\ln 2} \cdot \frac{U \cdot d}{I} \tag{1.31}$$

1.5 Materials for chemiresistor gas sensors

In this section the three materials used for chemical gas sensors in this work shall be described. There are many other semiconducting oxides, catalytic oxides and mixed oxides used for the creation of chemiresistors, but they shall not be mentioned here because this would reach too far. This work only includes investigations of gas sensors using SnO_2, WO_3 and MoO_3 as gas sensitive materials.

1.5.1 Tin dioxide

SnO_2 is the most common sensing material for chemiresistor gas sensors. It is a n-type semiconductor with a band gap of 3.6 eV [Kau07]. The melting point of tin dioxide is very high with 1900°C. The crystal structure can be seen in Figure 1.15. The unit cell consists of eight tin atoms at the corners and one in the middle of the cell. Four oxygen atoms are located at cell faces, while the other two are totally inside the unit cell. Each tin atom in the lattice is surrounded by an octahedron of oxygen atoms.

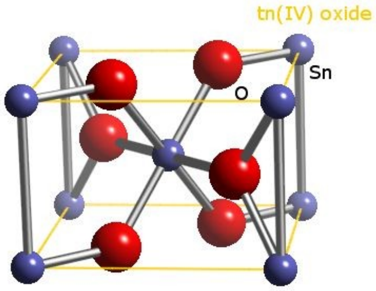

Figure 1.15: Crystal structure of tin dioxide [www.webelements.com]

The conductivity of SnO_2 is caused by a high number of lattice defects like oxygen vacancies. Tin dioxide is very sensitive to reducing gases as H_2S, H_2 and CO but also to oxidizing gases as for example O_3. Therefore SnO_2 is a highly non-selective material. [Kau07]

1.5.2 Tungsten trioxide

The heavy metal tungsten shows a high density and a very high melting point of 3422°C. The melting point of WO_3 is still at 1473°C. Tungsten trioxide is an n-type semiconductor. The electrical conductivity is caused by defects in the lattice structure.

If WO_3 is in a stoichiometric composition, the tungsten ions appear in their maximum oxidation state W^{6+}. The crystal structure of tungsten trioxide strongly depends on the temperature. From -50°C to 17°C it shows a triclinic structure, followed by a monoclinic one in a temperature range between 17°C and 330°C. From 330°c to 740°C it is orthorhombic and above this temperature becomes tetragonal.

WO_3 is a quite common material for chemiresistor gas sensors. To reach higher sensitivities tungsten trioxide is often doped with catalyst or promoter atoms as for example Au, Pt or Mo. [WiT10, Kau07]

1.5.3 Molybdenum trioxide

In MoO_3 the molybdenum ions are in the oxidation state Mo^{6+}. A MoO_3 solid consists of distorted MoO_6 octhahedra in an orthorhombic crystal. The octahedra build chains, which are again formed to layers by oxygen crosslinks. Each octahedral shows one short bond between a molybdenum and a non-bridging oxygen atom.

MoO_3 is a n-type semiconductor with a band gap of 3.2 eV. The material is not suitable for high temperature applications because of its low melting point at 795°C. MoO_3 can also not be used at room temperature because of its very high resistance at such low temperatures.

Molybdenum trioxide is not such a common material for chemiresistors as for example tin dioxide and tungsten trioxide, but investigations of its gas sensing properties are in progress. [WiM10, Kau07]

2. Piezoelectric microbalances

2.1 Historical overview:

Piezoelectric crystals were already used for ceremonies in early cultures. But it took a long time until Aepinus first described the strange behavior of tourmaline crystals in the 18th century. He named this phenomenon “pyroelectricity” because of the appearance of electrical charges in the heated crystals. Lord Kelvin later realized the connection between the pyroelectric and the piezoelectric effect. He found that the biggest part of the pyroelectrical charging was caused by the appearance of piezoelectrical surface charges, which arise from the elastic expansion of the crystal during temperature changes. Finally, in 1880 the brothers Curie discovered that mechanical deformation is able to produce a proportional electric charge. This phenomenon was named “piezoelectric effect”, where the Greek word “piezen” means “to press”. The Curies also found the inverse piezoelectric effect, where an electric charge leads to a mechanical deformation.

The first important technical application of piezoelectric quartz crystals was the use in ultrasonic locating systems (sonar) in the early 20th century. By sending electrical impulses to piezoelectric plates ultrasonic waves could be generated, which went through the water until they were reflected by an object. The returning waves could be also detected with quartz sensors using the direct piezoelectric effect. Later the radio technology was improved by the discovery of the frequency stabilizing effect of piezoelectric materials in circuits. A quartz crystal in an alternating electric field shows periodical deformation. This causes a system where electric energy is converted into mechanical energy. If the electrically defined frequency coincides with the Eigenfrequency the system resonates with very high amplitude. In addition to the radio technology this development was fundamental for the invention of the quartz watch. [Neu97]

The application range of piezoelectric crystals as microbalances became possible after G. Sauerbrey discovered the proportionality between the mass increase of a crystal due to adsorbed atoms and the decrease of the resonant frequency in 1959 [Sau59]. These new detectors were excellently capable for the measuring of small amounts of mass (down to 10^{-9}g). Today piezoelectric mass sensors are irreplaceable in thin film coating processes. [WiP10, Neu97]

2.2 The piezoelectric effect

The 32 crystallographic point groups are distinguished by the practicality of symmetry operations like reflection or rotation. These operations can be executed without changing the lattice structure. Only 20 point groups allow the appearance of the piezoelectric effect, since there must be no symmetry center in the unit cell [Wei89]. The effect appears in natural crystals, for example quartz (SiO_2), fabricated poled ceramics and some polymers [Fra04].

The direct piezoelectric effect means that mechanical pressure leads to electrical charges. When conversely electrical charges cause a mechanical deformation we speak of the inverse piezoelectric effect. Both effects are strictly proportional.

The reason for the appearance of piezoelectric behavior shall now be exemplified by the atomic structure of a quartz crystal. A. Meissner developed a model, based on the fact that the quartz crystal structure is arranged as a helix with one silicon and two oxygen atoms in turns around the helix [Mei27]. A quartz unit cell is built of three silicon and six oxygen atoms. Oxygen is combined in pairs, where each pair has four negative charges. Each silicon atom is four times positively charged. Accordingly a quartz crystal is electrically neutral under normal conditions. The polar axis of quartz is the X-axis.

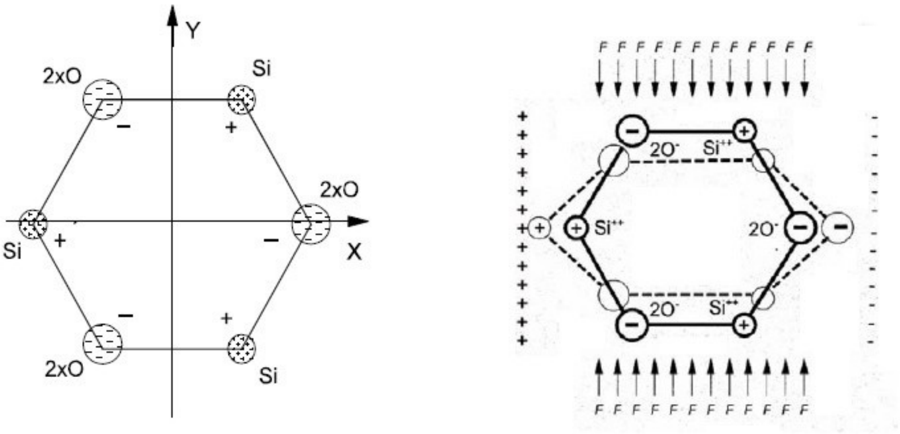

a) b)

Figure 2.1: Simplified cell structure of SiO_2, a) unstressed and b) with force acting on the crystal [Neu97]

Figure 2.1 shows a simplified sketch of SiO_2. The small circles represent the positive charged silicon ions and the big ones stand for the negatively charged oxygen ions. If a mechanical pressure deforms the crystal structure along the X-axis, a charge displacement will be the consequence. Therefore an electric polarization along the X-axis will appear and this leads to charges on the accordant surfaces of the crystal, in this case on the X-surfaces. The X-axis is called the electric axis. No polarization is possible along the Y-axis but if stress affects along this axis, a polarization in the X-direction will be the result. This behavior is called the transversal piezoelectric effect and therefore the Y-axis has the name mechanical axis. The indirect piezoelectric effect appears in this case as a deformation along the Y-axis caused by an electric charge in X-direction.

If electrodes are positioned on the crystal, at the opposite sides of the cut, the piezoelectric material acts like a capacitor with the crystal as the dielectric material. [Neu97, Fra04]

2.2.1 Pyroelectricity

Ten of the twenty crystallographic point groups, which allow the appearance of piezoelectricity, show spontaneous polarization not only caused by mechanical stress, but also by temperature changes. The appearance of surface charges due to a homogeneous temperature variation is called the pyroelectric effect. It results from the temperature dependence of the spontaneous polarization. The corresponding reciprocal effect is called the electrocaloric effect. The pyroelectric effect is utilized for the detection of infrared waves. [Wei89]

2.2.2 Piezoelectric coefficients

The matrix of elastic modules $\overleftrightarrow{C}$ acts as linear relationship between the stress tensor $\overleftrightarrow{\sigma}$ and the strain tensor $\overleftrightarrow{e}$.

$$\overleftrightarrow{\sigma} = \overleftrightarrow{C} \cdot \overleftrightarrow{e} \tag{2.1}$$

$\overleftrightarrow{\sigma}$ and $\overleftrightarrow{e}$ are both 3x3 matrices. Therefore $\overleftrightarrow{C}$ consists of 9x9 matrix elements. Because of the symmetry of $\overleftrightarrow{\sigma}$ and $\overleftrightarrow{e}$, only 36 components can be independent from each other. As a result $\overleftrightarrow{C}$ can be defined by a 6x6 matrix. The inversion of $\overleftrightarrow{C}$ is the matrix of the elastic coefficients $\overleftrightarrow{S}$:

$$\overleftrightarrow{S} = \begin{pmatrix} S_{11} & S_{12} & S_{13} & S_{14} & S_{15} & S_{16} \\ S_{21} & S_{22} & S_{23} & S_{24} & S_{25} & S_{26} \\ S_{31} & S_{32} & S_{33} & S_{34} & S_{35} & S_{36} \\ S_{41} & S_{42} & S_{43} & S_{44} & S_{45} & S_{46} \\ S_{51} & S_{52} & S_{52} & S_{54} & S_{55} & S_{56} \\ S_{61} & S_{62} & S_{63} & S_{64} & S_{65} & S_{66} \end{pmatrix} \tag{2.2}$$

It contains the elastic properties of each spatial direction of the crystal.

The polarization $\overleftrightarrow{P}$ and the strain tensor $\overleftrightarrow{e}$ for piezoelectric materials are defined as following:

$$\overleftrightarrow{P} = \overleftrightarrow{d}\overleftrightarrow{\sigma} + \chi_{el}\varepsilon_0\vec{E} \tag{2.3}$$

$$\overleftrightarrow{e} = \overleftrightarrow{S}\overleftrightarrow{\sigma} + \overleftrightarrow{d}\vec{E} \tag{2.4}$$

$\vec{E}$ indicates the electric field strength, ε_0 the electric constant, χ_{el} the electric susceptibility and $\overleftrightarrow{d}$ the matrix of piezoelectric coefficients.

$$\overleftrightarrow{d} = \begin{pmatrix} d_{11} & d_{12} & d_{13} & d_{14} & d_{15} & d_{16} \\ d_{21} & d_{22} & d_{23} & d_{24} & d_{25} & d_{26} \\ d_{31} & d_{32} & d_{33} & d_{34} & d_{35} & d_{36} \end{pmatrix}$$

Considering a crystal with high symmetry, many matrix elements become zero.
The matrix of the dielectric constants is given by:

$$\overleftrightarrow{\varepsilon} = \begin{pmatrix} \varepsilon_{11} & \varepsilon_{12} & \varepsilon_{13} \\ \varepsilon_{21} & \varepsilon_{22} & \varepsilon_{23} \\ \varepsilon_{31} & \varepsilon_{32} & \varepsilon_{33} \end{pmatrix}$$

Equation 2.3 shows that if $d \neq 0$, mechanical stress causes an additional polarization. A combination of $\overleftrightarrow{S}$, $\overleftrightarrow{d}$ and $\overleftrightarrow{\varepsilon}$ lead to a 9x9 matrix, which connects mechanics and electrics in a crystal.

$$\begin{array}{c|c|c|}
 & \mathrm{T} & \mathrm{D} \\ \hline
\mathrm{S} & \overleftrightarrow{S} & \overleftrightarrow{d}^{t} \\ \hline
\mathrm{E} & \overleftrightarrow{d} & \overleftrightarrow{\varepsilon} \\ \hline
\end{array}$$

Figure 2.2: Connection matrix composed of the elastic coefficient matrix, the piezoelectric coefficient matrix and the matrix of the dielectric constants

The tensile stress *T*, the spatial deformation *S*, the electric induction density *D* and the electric field strength *E* are linked by this matrix. [Wei89]

$$D = e \cdot S + \varepsilon \cdot E \tag{2.5}$$

$$T = C \cdot S + e \cdot E \tag{2.6}$$

By disregarding the electric field strength the polarization in a crystal can be written as:

$$\vec{P} = \vec{P}_{xx} + \vec{P}_{yy} + \vec{P}_{zz} \tag{2.7}$$

x, y and *z* are the directions of an orthogonal system related to the crystal axis. Furthermore the polarization, caused by the piezoelectric effect, consists of:

$$\begin{aligned} \vec{P}_{xx} &= d_{11}\vec{\sigma}_{xx} + d_{12}\vec{\sigma}_{yy} + d_{13}\vec{\sigma}_{zz} \\ \vec{P}_{yy} &= d_{21}\vec{\sigma}_{xx} + d_{22}\vec{\sigma}_{yy} + d_{23}\vec{\sigma}_{zz} \\ \vec{P}_{zz} &= d_{31}\vec{\sigma}_{xx} + d_{32}\vec{\sigma}_{yy} + d_{33}\vec{\sigma}_{zz} \end{aligned} \tag{2.8}$$

The constants d_{mn} stand for the piezoelectric coefficients along the orthogonal axes and form the matrix of piezoelectric coefficients.
The appearing charge in a piezoelectric crystal is proportional to the external force. In x-direction for example the charge is given by

$$Q_x = d_{11} F_x \tag{2.9}$$

The voltage between the electrodes on the crystal surface depends on the capacitance *C*.

$$V = \frac{Q_x}{C} = \frac{d_{11}}{C} F_x \tag{2.10}$$

The capacitance on the other side is connected to the thickness of the crystal *l* and the electrode surface area *a*:

$$C = \kappa \varepsilon_0 \frac{a}{l} \tag{2.11}$$

with the permittivity constant ε_0 and the dielectric constant κ.
Therefore the output voltage can be calculated by the following formula [Fra04]:

$$V = \frac{d_{11}}{\kappa \varepsilon_0 a} \cdot F \cdot x \tag{2.12}$$

2.3 Piezoelectric resonators

2.3.1 Modes of oscillation

Usually piezoelectric resonators are designed as crystal plates with electrodes placed on the opposite sides. If a current is provided to the electrodes, a deformation of the crystal plate appears. An alternating current causes a mechanical oscillation. A resonation can be produced by adapting the current frequency to the Eigenfrequency of the piezoelectric material. Between the two electrodes a standing wave occurs.

The range of possible oscillation frequencies in piezoelectric crystals is limited by the resonators dimensions and the fabrication process. Depending on the designated frequency value, one can choose between four different modes of oscillation:

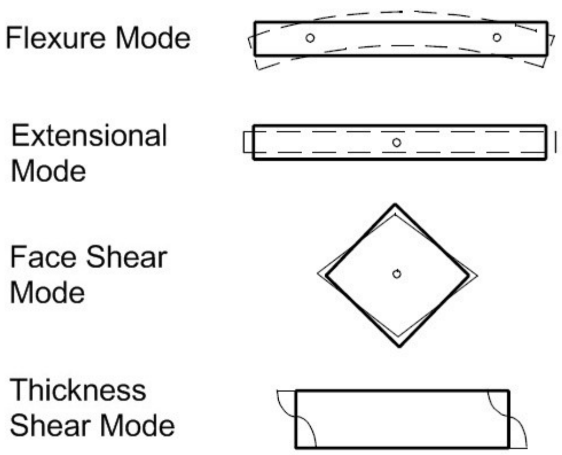

Figure 2.3: Modes of oscillation of a piezoelectric resonator [Neu97]

The Flexure Mode oscillates with the lowest frequency, while the Thickness Shear Mode offers the highest one. Additionally this oscillation mode guarantees high stability. For this reason, today most of the technical interest is directed towards thickness shear mode resonators.

Another type of resonators consists of fork-like formed piezoelectric crystals. In this case the oscillation mode can be allocated to the Flexure Mode. [Neu97]

Thickness Shear Mode Resonators:

As the crystals described in this report are resonating in thickness shear mode, this very important and mostly used oscillation mode will be discussed more closely.

The orientation of the standing waves in such a resonator is normal to the surfaces. Therefore the nodal points are always located inside the crystal and can not be used for a resonator mounting. The fundamental mode and the 3rd overtone of a thickness shear mode resonator are illustrated in Figure 2.4.

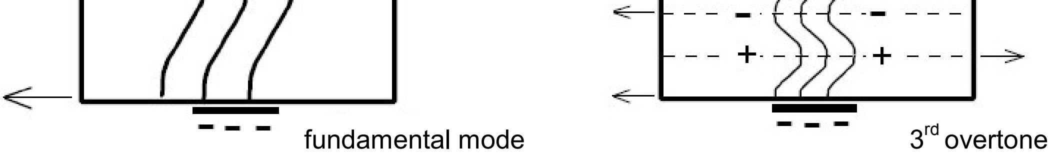

Figure 2.4: Fundamental mode and 3rd overtone of a thickness shear mode resonator [Neu97]

By using large crystal geometries and very small electrodes the oscillation can be located in the middle of the crystal. Therefore a mounting at the edge of the resonator becomes possible. Alternatively lenticularly curved surfaces are used, which enable small crystals with low frequencies. The distribution of the oscillation amplitude for different resonator designs can be seen in Figure 2.5. [Neu97]

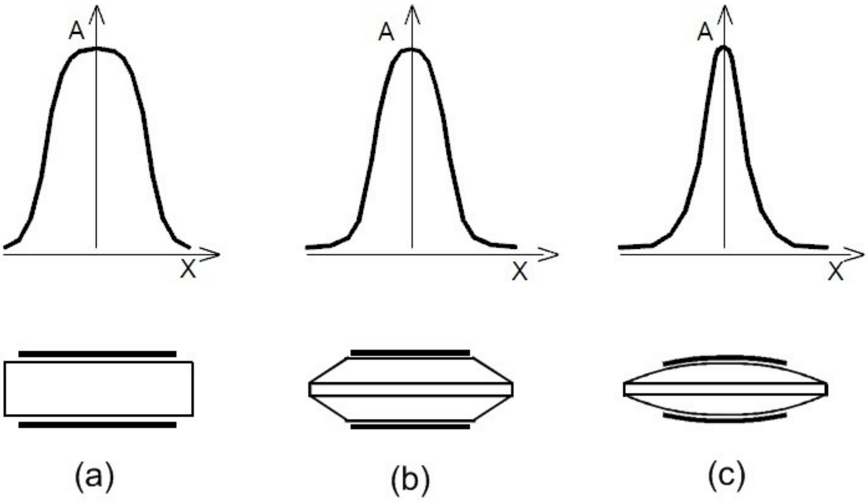

Figure 2.5: Distribution of oscillation amplitude for (a) a plane-parallel, (b) a plane-facet and (c) a lenticular resonator [Neu97]

Relationship between mass and frequency for thickness shear mode resonators:

The equation found by G. Sauerbrey [Sau59] describes the connection between the mass increase of a crystal caused by adsorbed atoms and the decrease of the oscillation frequency. As can be seen in Figure 2.4, the oscillation frequency directly depends on the thickness of the crystal *d*. Always half the wavelength *λ* is located between the electrodes. Therefore the frequency *f* can be calculated by:

$$f = \frac{c}{\lambda} = \frac{c}{2 \cdot d} \tag{2.13}$$

c describes the phase velocity of the acoustic wave.

If the thickness of a resonator grows due to the adsorption of atoms at the crystal surface, the frequency shift *Δf/f* also increases. If the attached film is thin enough, the adsorption can be deemed to be a thickness increase of the crystal material itself. The frequency shift can now be described by:

$$\frac{\Delta f}{f} = -\frac{\Delta d}{d} = -\frac{\Delta m}{d \cdot \rho \cdot A} \tag{2.14}$$

A is the area on the crystal surface where the oscillation takes place and ρ stands for the density of the crystal material. The mass increase is denoted Δm.

The Sauerbrey equation is fundamental for all microbalance applications but it is only valid for inelastic thin films ($\Delta m/m$ up to 2%), because the elastic properties of the film are not included.

2.3.2 Crystal cuts

To increase some of the desired properties, like a minimal temperature dependence for example, the resonator is cut out of the piezoelectric crystal under a defined angle. There are two methods of notation for different cuts. The first one works with the alphabetic itemization of crystal cuts, leading to a minimal temperature coefficient at room temperature. The additional letter T stands for “temperature compensated”. An example for this notation is the AT-cut, which is shown among others in Figure 2.6. There are also some special cuts available, such as the SC-cut (“stress-compensated”), which shows a very low frequency change due to mechanical stress.

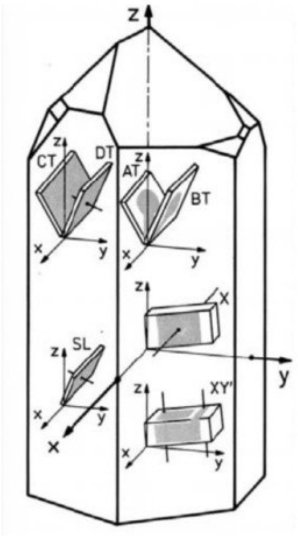

Figure 2.6: Some conventional quartz cuts [Neu97]

Figure 2.6 also contains the second method of notation, where the cuts are named according to the crystallographic axis, which stands orthogonal to the main surface of the crystal. The X-axis in Figure 2.6 describes the electric axis, while the Y-axis is the mechanical one. The Z-axis is the optic crystallographic axis, which means that birefringence can be observed along this axis.

For quartz and also for gallium orthophosphate Y-cuts are preferred. The scheme of an optional Y-cut is illustrated in Figure 2.7. The cut is made along a plane, which is oriented orthogonally to the Y-axis at the beginning and is then rotated about the X-axis with a certain angle θ. Properties of the crystal, like temperature and pressure dependence, can be optimized by choosing a well defined cut angle θ. The angle is then added to the notation to get an exact definition of the cut. The total description is written as: $Y \pm \theta$-Cut. [Neu97]

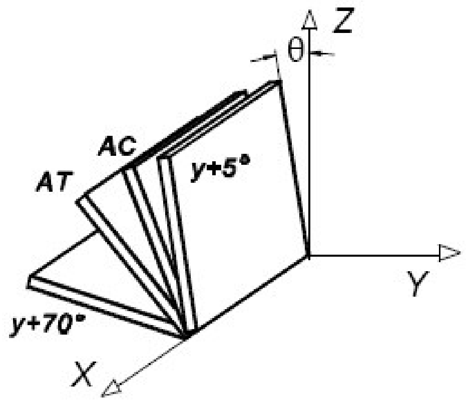

Figure 2.7: Schema of an optional Y-cut [Neu97]

2.3.3 Quartz (SiO_2) as resonator

Quartz is the most important natural piezoelectric material, but can also be man-made. The chemical formula of quartz is SiO_2. Each elementary cell consists of three SiO_2 molecules. The threefold symmetry axis is the optical crystallographic axis, mentioned above in chapter 2.3.2. There are different modifications of quartz, but only the α-modification shows piezoelectric behavior. This modification belongs to point group 32. SiO_2 is a common component of the earth's surface (14%), but in pure form (called quartz) it does not occur very often. Only a few naturally grown quartz crystals are free of crystallographic defects. Because of this quality problem and the shortage of natural quartz crystals in the middle of the last century, the development of a synthetic manufacturing became extremely important. The large-scale production of synthesized SiO_2 crystals was introduced in 1964.

In spite of the excellent piezoelectric behavior of quartz crystals they are limited by the operating temperature. Over a crystal temperature of 573°C the α-quartz is transformed into β-modification. This phase change is connected to a symmetry increase, which leads to the disappearance of the piezoelectric behavior. [Neu97]

2.3.4 Gallium orthophosphate ($GaPO_4$)

To enable the use of piezoelectric resonators in temperature ranges above 573°C, other quartz like materials were developed. A very capable material is gallium orthophosphate, which shows the same mechanical strength as SiO_2 and a twice as high piezoelectric effect. The electro-mechanical coupling is even better than the one of quartz. But the most important improvement is the appearance of piezoelectric behavior up to a temperature of 970°C.

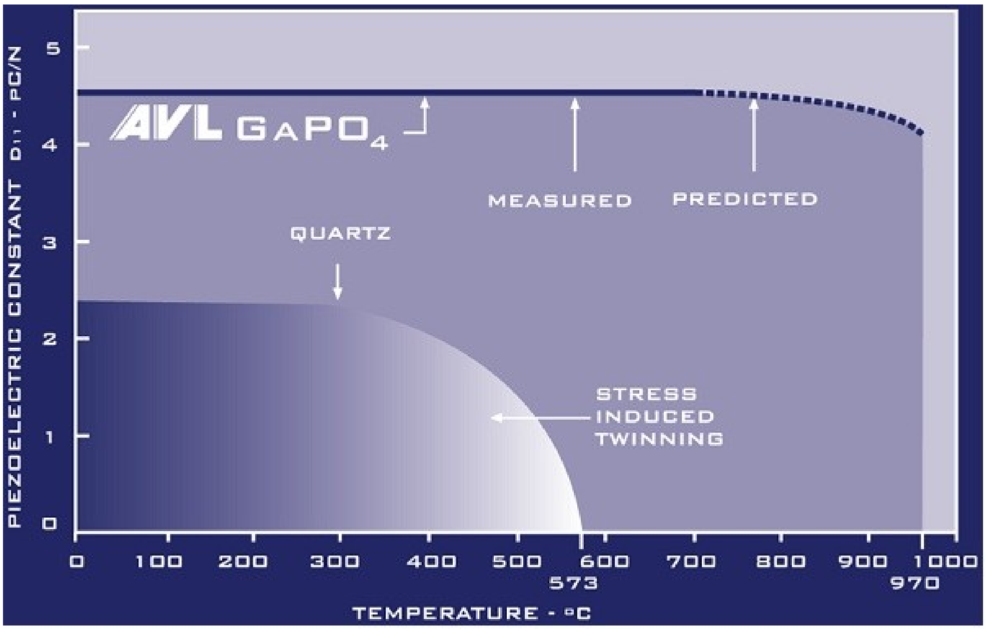

Figure 2.8: Temperature dependence of the piezoelectric constant for SiO_2 and $GaPO_4$ [Pie10]

These high operation temperatures are possible because the α-β phase change of SiO_2 does not appear in gallium orthophosphate. The piezoelectric effect is limited by a phase change into a cristobalite like structure at temperatures above 970°C. Figure 2.8 also shows that the piezoelectric constant of $GaPO_4$ is twice as large as the one of quartz. Therefore the sensitivity of a piezoelectric sensor made of $GaPO_4$ is much higher.

The crystal structure of $GaPO_4$ is similar to that of α-SiO_2, only the Si is alternatingly replaced by gallium and phosphor atoms. As a result, the unit cell is doubled across the Z-axis. $GaPO_4$ also belongs to point group 32. Figure 2.9 shows the crystal lattice of gallium orthophosphate.

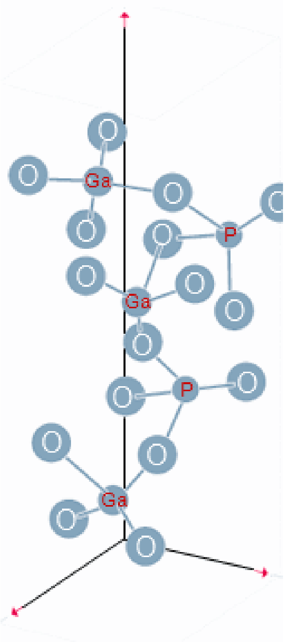

Figure 2.9: Schematic lattice structure of gallium orthophosphate [Pie10]

Gallium orthophosphate does not appear in nature and has to be fabricated by hydrothermal rearing. The most important technical applications of $GaPO_4$ crystals are high temperature pressure sensors and microbalances. [Pie10]

2.3.5 Temperature dependence of the oscillation frequency

The frequency change due to the crystal's temperature is a very important property of piezoelectric resonators. Most crystal cuts lead to a parabolic temperature dependence. When the temperature is increased, the frequency grows until it reaches a reversal point T_0. Above this point the resonant frequency decreases again. As a consequence, the frequency is almost independent of the temperature around T_0 and the resonator can be declared as temperature stabilized in this region. Because T_0 differs for each crystal cut, it is possible to create a resonator with stabilized oscillation behavior in a well defined temperature range by choosing a certain cut angle.

The temperature dependence of the frequency can in most cases be described by the equation of a parabola:

$$\frac{\Delta f}{f} = -a(T - T_0)^2 \tag{2.15}$$

The universal parabolic constant *a* is defined by the crystal cut and is additionally affected by the manufacturing process. [Neu97]

2.3.6 The equivalent circuit diagram

The electrical impact of a mechanical oscillation can be described by a equivalent circuit. The dynamic capacity C_1 equates with the elastic compliance and the inductance L_1 conforms to the oscillating mass of the resonator. The resistance R_1 stands for the dynamic oscillation loss. These devices are the components of an electric circuit, which has a static capacity C_0 connected in parallel.

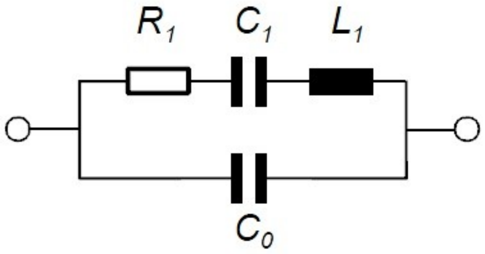

Figure 2.10: Equivalent circuit diagram of a resonator [Neu97]

The static parallel capacity C_0:

This capacity can be measured directly at the resonator electrodes. It is a combination of the electrode capacity C_E and the mounting capacities C_H in the resonator package. C_E can be calculated like the capacity of a plate condenser, where d is the thickness of the crystal and therefore also the space between the condenser plates. The factor A stands for the area of the electrodes on the crystal and ε for the dielectric constant of the medium:

$$C_E = \varepsilon_0 \varepsilon \frac{A}{d} \tag{2.16}$$

The mounting capacities are generally estimated with 0.8 pF.

The dynamic capacity C_1:

The dynamic capacity depends on the elastic constants s_{jj} and the piezoelectric constants d_{ij}. Additionally, the electrode area A, the thickness and curvature of the resonator and the order of the overtone are decisive factors. The elastic constants s_{jj} and the piezoelectric constants d_{ij} vary for different cut angels. Therefore a special crystal cut shows well defined values for the devices of the equivalent circuit.

The resonator resistance R1:

This resistance is an indicator for the damping of the oscillating resonator. Thereby the viscous damping of the material and the components caused by the finite geometry of the crystal and by the surrounding gas atmosphere are responsible for the resulting sensor damping. In most cases the electrical resistance of the electrodes plays a less significant role. The damping constant τ_1 can be calculated by using the sensor resistance and the dynamic capacity:

$$\tau_1 = R_1 \cdot C_1 \tag{2.17}$$

The damping constant is smaller for lenticular crystals than for plane-parallel ones.

The oscillation quality of a piezoelectric crystal:

The oscillation quality is the most important factor to characterize the oscillation behavior of a quartz resonator. The value can be calculated by using the components of the equivalent circuit:

$$Q = \frac{1}{2\pi f \cdot C_1 R_1} \tag{2.18}$$

The quality strongly depends on the resonant frequency f of the crystal. At high frequencies it decreases strongly. Therefore the resonators with very high qualities are usually oscillating in a frequency range from 2 to 5 MHz. [Neu97]

Another definition of the oscillation quality is the relationship between the resonant frequency and the bandwidth Δf:

$$Q = \frac{f}{\Delta f} \tag{2.19}$$

The bandwidth is defined by the full width at half maximum.

In practice the quality of a resonator is an indicator for the energy, which has to be provided to the crystal to guarantee a stable oscillation behavior. High quality crystals are oscillating with small energy input.

Part II: Research

3. Possibilities for selectivity increase of chemiresistor gas sensors

Well established methods for the detection of certain gas species are optical spectrometers, mass spectrometers and gas chromatographs. Compared to them, metal oxide chemical gas sensors offer a wide range of advantages. It is possible to fabricate sensor elements with very small size, low weight and simple configuration. Additionally, the manufacturing of semiconductor gas sensors is also marked by a low cost expenditure.

The major disadvantage of chemiresistor gas sensors is their very low selectivity. All reducing gases, adsorbed at the sensor surface, cause a decrease of the sensor resistance. Although the intensity of the sensor signal can vary according to different gas species, a certain sensor response due to a specific gas can not be identified. Also oxidizing gases cause an increase of the resistance, which can not be identified separately. If the components of a gas flow are unknown, it is not possible to achieve definite information about the gas flow elements or their concentrations by using chemiresistor gas sensors. Therefore a lot of research is carried out by universities and sensor manufacturers in order to increase the selectivity of chemiresistor sensing elements. The major approaches concerning this topic will be presented in this chapter.

3.1. Selection of a single gas species

There are several methods to increase the response of a chemiresistor gas sensor due to a certain target gas. If the sensor response to one species becomes much bigger than those to all other gases contained in a gas stream, the sensor can be considered as independent of background gases. In this way sensor elements for concentration measurements of one special gas species are created.

3.1.1. Deployment of chemical or physical filters

In many applications chemical gas sensors are used for the detections of certain gas species. If an application requires the sensor response to only one defined gas, catalytic filter materials can be applied above the sensing element. These filters are intended to prevent a unintentional reaction between the other gas species and the sensor surface. Catalytic reactions of the diffusing gas, due to the filter material, enable the presence of only one defined target gas at the sensor surface. The concentration of the target gas itself needs to stay as stable as possible. When the optimum operating temperature of the sensor element is defined, also the optimum temperature for the catalytic process has to be considered.

To give some examples for catalytic filter materials used in chemical gas sensors made of SnO_2, investigations concerning the analysis of breath gas are sketched [Par02]. When a Nb_2O_5 filter layer was applied to a tin dioxide sensor, the response to propane could be strongly decreased. Therefore the desired sensor response to ethylalcohol was unaffected by propane. An other approach was the deployment of SnO_2 mixed with 0.5wt.% Pt as filter material. This configuration was intended for iso-butane gas detection. The catalytic filter strongly decreased the sensor response to ethylalcohol. In another case M. Fleischer et al [Fle00] developed a catalytic filter for a Ga_2O_3 semiconductor gas sensor, by using very porous Ga_2O_3 ceramic above the sensing layer. This configuration strongly improved the detection of methane.

Additional to chemical catalytic filters, also investigations using physical filter layers have been performed. For example, the application of a SiO_2 layer on top of a Ga_2O_3 sensing element led to a strongly decreased sensor response to methane, ethane, carbon monoxide and nitrogen monoxide. In this way selective hydrogen sensors could be developed. The selectivity increasing effect of the filter occurs due to the prevented formation of hydroxyl groups at the sensor surface [Fle00, Weh00].

3.1.2. Sensor operation at optimum temperature

The selectivity of a certain sensor material to a certain target gas is strongly influenced by the operating temperature [Kau07, Iva00]. In many cases a special gas sensitive layer shows very different intensities of the sensor response to different gas species at a certain temperature. By measuring the sensor response to only one well defined gas over a wide temperature range, it is possible to identify the optimum temperature for the detection of a certain gas species. In this temperature region, the sensitivity to all other gases containing in the gas atmosphere has to be extremely low. If the sensor element contains a heating device, the optimum temperature can easily be achieved during measurements.

3.1.3. Doping of gas sensitive material

A very common method to increase the selectivity of a chemiresistor gas sensor is the doping of the sensing layer. The doping of a SnO_2 sensor with CuO to increase the sensor selectivity to hydrogen sulfide was described by J. Liu et al [Liu03]. Measurements at 200°C with H_2S, H_2, CH_3SH and CO led to the result that CuO doped tin dioxide shows a much higher sensitivity to hydrogen sulfide than to all other gas species investigated. The increased sensitivity to H_2S appears due to the fact that SnO_2 is an n-type semiconductor, while CuO is p-type. Therefore the sensor surface consists of many n-p-n junctions and the electronic band structure of the doped material shows a potential barrier at the interface of the different molecules.

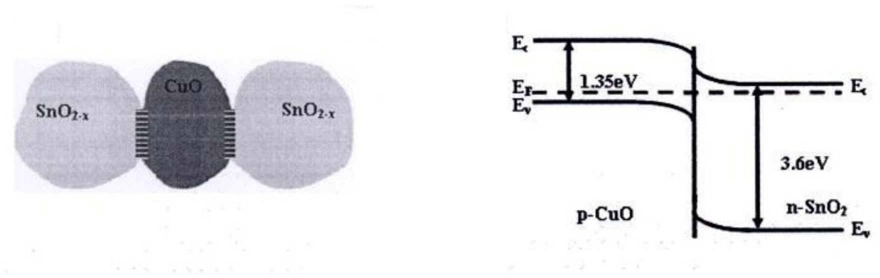

(a) (b)

Figure 3.1: (a) CuO grain located between two SnO_2 grains; (b) band structure at CuO and SnO_2 interface [Kau07]

The high amount of these potential barriers in the whole sensing material leads to a high basic resistance of the sensor. If hydrogen sulfide reacts with CuO it gets sulfurized to CuS, the potential barrier disappears and the sensor resistance strongly decreases.

According to the large number of doping materials for SnO_2 sensors, some more examples shall be mentioned. The doping of tin dioxide layers with fluorine atoms leads to an increased sensitivity to H_2 [Han06]. This effect appears, because the fluorine atoms offer favorable sites for the adsorption of hydrogen or due to the fact that the foreign atoms increase the n-type property of the sensing material. A hydrogen sensor, capable for room temperature applications using In_2O_3 doped SnO_2 layers, was developed by S. Shukla et al [Shu05]. The added In_2O_3 molecules lead to the formation of $InSn_4$ phases, which surround the SnO_2 phases and prevent the diffusion of carbon monoxide into the sensing material. By eliminating the sensor response to CO the sensitivity to H_2 was increased. Apart from hydrogen detection, it was investigated, that doping of SnO_2 layers with antimony atoms lead to strongly decreased water sensitivities [Kri09]. This is a big advantage for the sensor stability due to unintentional humidity in the considered gas flow.

3.1.4. Nanoparticles applied to sensor surface

Additional to doping of the sensing material the application of nanoparticles on the sensor surface was investigated. SnO_2 particles added to a fluorine doped SnO_2 layer strongly increased the sensors selectivity to hydrogen [Han06]. The very small H_2 molecules are able to pass the SnO_2 particles and reach the subjacent sensing layer, while bigger molecules like CH_4, C_3H_8 and CO are held off from the sensor surface.

3.2. Selectivity increase due to several gas species

The unknown components of a gas stream are difficult to analyze by using a common chemiresistor gas sensor. In such a situation the methods, mentioned above, can only generate information about one special gas species. To enable the identification of several gas stream components, other sensor configurations have to be applied.

3.2.1. Dynamic measurements

Investigations concerning the improvement of the sensor selectivity by performing dynamic measurements instead of static ones, have been performed to develop a measuring method for the identification of several components of an unknown gas stream [Sun04]. For this purpose a sensing layer containing of SnO_2 was located above a heating element. This heater enables a rapid variation of the operating temperature during measurements. Different temperature profiles can be achieved by applying different voltage surges to the heater. The adsorption of gases at the sensor surface strongly differs with the temperature. Test with gases like ethanol, methanol, formaldehyde and cyclohexanone showed very different sensor responses due to the varied temperature during the measurements. The sensor response of a certain gas can additionally be modified by changing the duty ratio or the waveform of the heating process. Rectangular, sinusoidal, saw-tooth and pulsed waveforms have been investigated. Using the characteristic sensor responses due to certain gases at varied temperature, duty ratio and waveform, the identification of certain gas mixture components became possible.

3.2.2. Multilayer sensing elements

The methods to increase the sensor sensitivity to one defined target gas, which have been described above, can be used for the creation of a multilayer sensor. In this concept the sensing element contains several different materials. Each material shows a strongly increased sensitivity to a certain gas species. Thereby the sensing element can consist of an area made of the same basic material, doped with different foreign atoms, or of totally different components. The different sensing layers have to be electrically contacted separately. If the cross-sensitivity of the several areas can be considered as insignificant, the response of each material can be related to one defined gas species. In this way the detection of certain gases in a gas stream and the determination of their concentration should be possible. The Finnish company Micronova is developing such multilayer semiconductor gas sensors, consisting of tin dioxide sensing areas doped with elements like platinum, palladium and nickel [Mic10].

3.2.3. Integration of gas sensitive layers on a microbalance

A totally different approach to increase the selectivity of a chemiresistor gas sensor, compared to the concepts mentioned above, was made by AVL, AIT, and NTCW. The companies AIT and NTCW both develop semiconductor gas sensors with the common disadvantage of very small selectivity. To enable the identification of certain gas species, metal oxide sensors, detecting conductivity changes, will be combined with a totally different sensing concept. A sensing element, which additionally contains a piezoelectric microbalance, enables a simultaneous detection of conductivity and mass changes due to the presence of certain gas species at the sensor surface. The electrical signal of the metal oxide chemical gas sensors is proportional to the number of exchanged charge carriers and therefore also to the number of adsorbed molecules, but the adsorbed species cannot be identified by this sensing concept. For example, the response of a SnO_2 sensor to H_2O and CO is very similar and cannot be separated without any additional information. As these two species show a different molecular mass (18 and 28 g/mol), the adsorption of water or carbon monoxide on a microbalance leads to distinct sensor signals. The piezoelectric microbalance directly reflects the masses of the adsorbed molecules and therefore increases the selectivity of such an integrated sensing system.

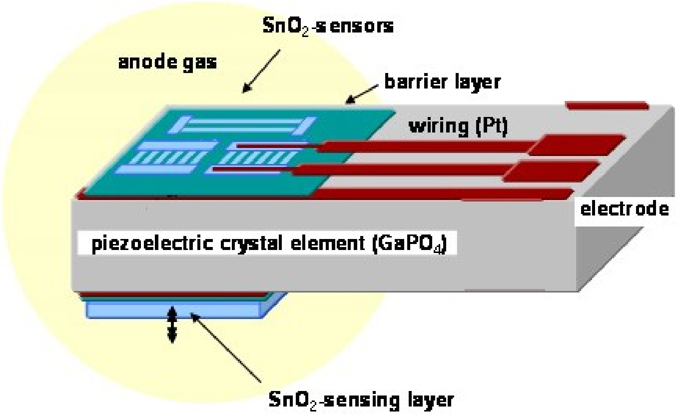

Figure 3.2: Detail of the possible geometry of a disc shaped piezoelectric microbalance with integrated chemical gas sensor layers made of SnO_2

The possible design of an integrated sensing system, containing a microbalance and several chemical gas sensitive nanolayers, is demonstrated in Figure 3.2. The concept involves using a disc shaped high temperature $GaPO_4$ microbalance. In order to show the two electrodes on both sides of the crystal, only a part of the disc resonator is illustrated here. The oscillation is induced by two electrodes forming an active area in the middle of the crystal. Conductive paths are leading to the edge of the resonator, where mounting and contacting takes place. After the creation of a barrier layer on top of the active area, different metal oxide sensing nanolayers can be located. These layers are realized in optimum conductive path geometries and are electrically contacted by contacting paths. These paths also lead to the edge of the crystal, where they can be connected to a potential supply. In this way conductivity changes of the nanolayers can be detected. In this possible sensor design the back side electrode of the microbalance is totally covered with a gas sensing material, as for example tin dioxide. In this way large-area adsorption of the investigated molecules can be performed and the detection of mass changes on the oscillating crystal becomes possible. This design is one possible geometry of an integrated sensor system. It can be modified according to the requirements imposed by the employed metal oxide nanolayers.

Part III: Sensor design and measurements

4. Sensor description

The aim of the project is the development of a highly sensitive and highly selective gas sensor, suitable for the implementation in fuel cell systems. Basic characterization measurements of different chemiresistor gas sensors, developed by the Austrian Institute of Technology AIT and the NanoTec Center Weiz NTCW, were performed to enable the comparison of the sensor responses in different gas atmospheres. Due to the fact that chemiresistors are very unselective, the integration of the gas sensitive layers of AIT and NTCW on a high temperature suitable microbalance of AVL is planned. The combination of these two different sensing methods will lead to an increase of the selectivity by simultaneous measurement of the adsorbed gas mass. In this chapter, the two different sensor designs of the investigated chemiresistors are described. Additionally, the AVL microbalance is introduced.

4.1. WO_3 and MoO_3 chemical gas sensors from NTCW

The NanoTec Center Weiz developed a new sensor concept by using nanoparticles as sensing material instead of common bulk geometries. The sensor design enables a four point measurement, which is independent of contact resistances. The development of these sensors has been performed by Markus Postl and is described in detail in his diploma thesis [Pos09]. I want to give a short overview of the sensor design and fabrication in this chapter. Additionally, some innovations made by NTCW are discussed.

4.1.1. Sensor design

- **Substrate:**

The previously used sensor substrate was common glass, due to its electrical insulating and temperature stability properties. In order to enable applications in temperature ranges above 500°C, also silicon substrates, with an insulating silicon dioxide layer on top, have been fabricated.

- **Conductive path structure:**

This sensor concept is basically a four point method, as described in chapter 1.4.6, to measure the resistance of a WO_3 nanoparticle layer. The four test prods are realised as four conductive paths arranged in a meander structure. The paths are not in touch with each other on the substrate. The electrical contact takes place only due to the nanoparticle layer on top of the paths. To enable an easy contacting of the paths, they lead to four pads, made of evaporated gold. The whole sensor area, including the Au pads, occupies 10 x 10 mm on the substrate.

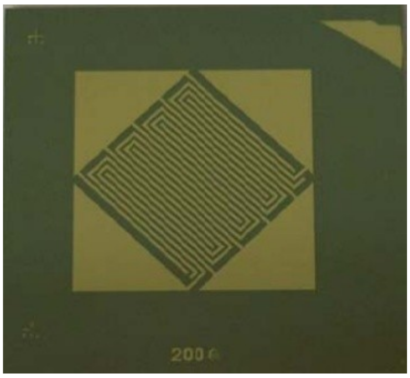

Figure 4.1: Meander structure of conductive paths on a Si/SiO_2 substrate with 200 µm line width

The primary path structure consisted of 200 µm wide paths. The line spacing between the paths showed the same width. Additionally the structure has been miniaturized by using a line width and spacing of 50 µm, by retaining the same sensor area. In this work sensors with both geometries have been investigated.

- **Conductive path layers:**

The undercoating and the conductive paths were applied to the substrate by physical vapour deposition. The path structure was produced by using photolithography. Therefore the path design was printed onto an overhead transparency with a common inkjet printer. By using this mask, only defined parts of a photoresist on the substrate surface are exposed to light. Depending on the kind of photoresist, it shows better or worse solubility due to interaction with light. After the exposure and removal of the exposed photoresist, the conductive paths consisting of an undercoating of 5 nm chrome and a 50 nm thick gold layer were deposited inside a vacuum chamber. The undercoating was necessary because gold does not adhere on the substrate. This primary used layer configuration showed defects caused by stress effects after the annealing procedure at 500°C. A gold layer, damaged in this way, is demonstrated in Figure 4.2.

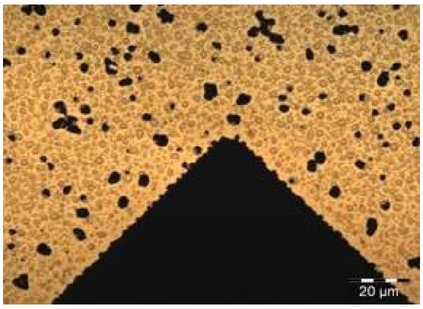

Figure 4.2: Defects in the gold conductive paths caused by stress effects

In order to protect the conductive paths against this effect an additional undercoating of 10 nm aluminium was evaporated between the chrome and the gold layer. This layer sequence prevents the destruction of the gold paths during the annealing process.

The last production step concerning the conductive paths is the photoresist lift off. The sensors are immersed in acetone and the metal layers between the conductive paths can be removed.

- **Application of WO_3 nanoparticle sensing layer:**

The WO_3 nanoparticles were fabricated by microwave plasma synthesis. Therefore a $W(CO)_6$ precursor was evaporated and mixed with argon gas containing oxygen molecules for the oxidation of tungsten. The species are ionized and/or dissociated in the microwave plasma, which leads to the creation of metal oxide clusters. The clusters build agglomerates which are collected at a cooling finger. To enable further processing the nanoparticles were dispersed in isopropanol. The nanoparticle diameter was investigated by a transmission electron microscope and showed a mean diameter of 3 nm.

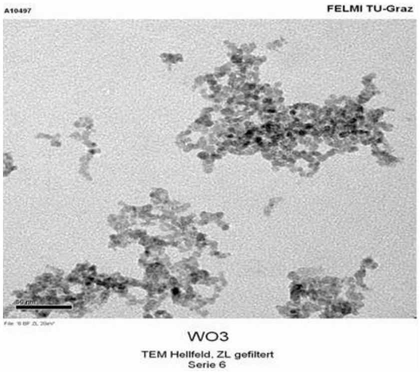

Figure 4.3: TEM picture of WO_3 nanoparticle agglomerates [Pos09]

This nanoparticle dispersion was dripped onto the conductive paths. In order to realize a homogenous layer the sensor was spin coated. During this procedure the isopropanol evaporated and only the WO_3 nanoparticle layer remained on the sensor surface.

- **Application of MoO_3 nanoparticle sensing layer:**

The deployment of molybdenum trioxide nanoparticles instead of tungsten trioxide was an innovation and therefore first tests with this sensing material were performed during the characterization at AVL.

The sensor design and fabrication was similar to the WO_3 sensors. A difference was the fabrication and application of the MoO_3 nanoparticles by using Pulsed Laser Deposition. Thereby the molybdenum is evaporated and ionized by a laser beam. In a certain gas atmosphere the metal ions are oxidized. The creation of MoO_3 clusters during the process is possible.

- **Annealing:**

After the nanoparticle application the sensors were annealed at a temperature of 500°C in air. This enables a good sensor behavior during measurements up to 400°C. During this process the agglomerates are connected to each other by the creation of sinter necks. Therefore the overall resistance is decreased.

4.1.2. Measuring chamber

In order to enable measurements with the sensor geometry mentioned above, it was necessary for NTCW to design and fabricate a special test chamber. Detailed information about it can be found in [Pos09]. As this measurement configuration was also used in our characterization measurements, it is also described shortly in this chapter.

The chamber itself is made of stainless steel and has a cylindrical geometry with a volume of about 120 cm³. Gas inlet and outlet are positioned at opposite sides of the chamber. A ceramic base with an integrated heating plate is located at the center. The sensor is positioned on this base and heated by the plate beneath. Therefore it is possible to work with very constant sensor temperatures. A temperature sensor could be optionally placed at the ceramic base or directly on the sensor.

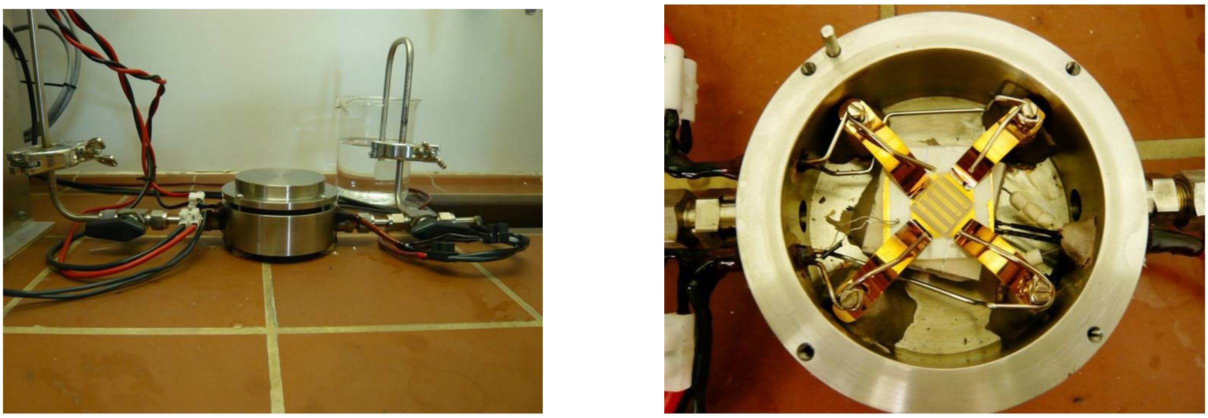
(a) (b)

Figure 4.4: NTCW measuring chamber (a) form outside and (b) the interior configuration [Pos09]

The electrical contacting of the gold pads is realized by using gold coated contact springs, made of stainless steel. Also the measurement connections are realized by stainless steel wires. The feedthroughs of the wires are tightened by using epoxy adhesive. The cover plate also includes a rubber gasket. Therefore the gas tightness of the measurement chamber is assured.

4.2. SnO_2 chemical gas sensors from AIT

The gas sensor developed by AIT contains SnO_2 as sensitive layer, which is a common material for chemiresistors. Unlike the NTCW sensors, in this configuration the sensing layer itself is realized as conductive paths. Nanoparticle layers are not employed in this sensor design.

4.2.1. Sensor design

- **Substrate:**

As sensor substrate AIT uses a silicon waver, with a 750 nm thick insulating SiO_2 layer on top. This enables applications in temperature ranges above 500°C.

- **Conductive path structure:**

For this sensor configuration an interdigital conductive path design is not necessary, because the sensing layer can be contacted directly. The sensing material tin dioxide is applied to the surface and structured into conductive paths. The electrical contact is performed by contacting pads. The schematical sensor structure and a scanning electron microscope image are illustrated in Figure 4.5. The arrows mark the direction of the current.

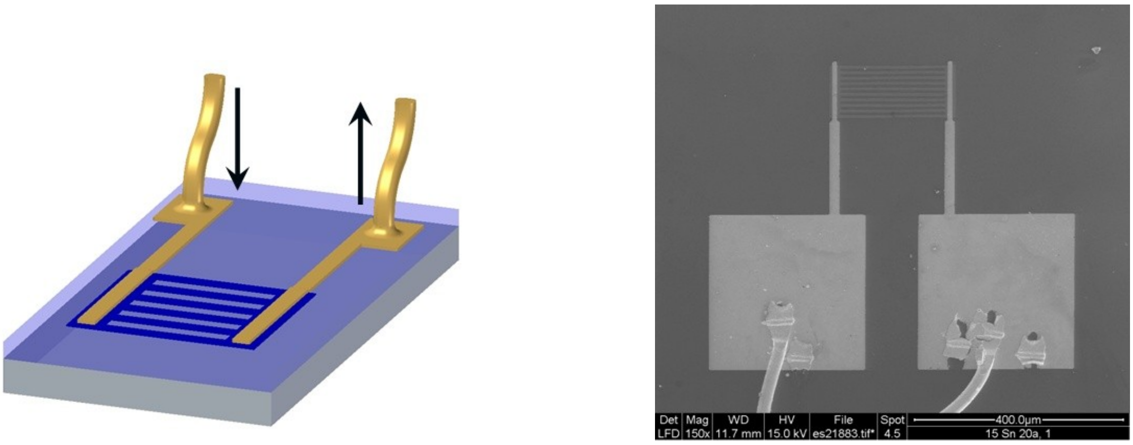

(a) (b)

Figure 4.5: (a) Schema of SnO_2 conductive paths (dark blue) and contacting pads (yellow) and (b) SEM image of a real sensing element with bonding wires on the contacting pads

The sensing area of these sensors is much smaller in comparison to NTCW. The conductive paths are about 200 µm long. The width of the hole sensing area amounts 100 µm. There are three different path geometries fabricated by AIT. Thereby the dimensions of the sensing element remain constant, while the number and width of the paths vary. The first available senor geometry contains ten conductive paths with line width and spacing of about

5.3 µm. A second geometry uses expanded paths with a line width of about 11 µm. According to the constant sensor area, only five instead of ten paths are realized. Finally, a sensor without conductive paths but with a conductive area was produced. In this case one 200 µm x 100 µm big area made of SnO_2 acts as sensing layer. The three different sensor geometries are illustrated by SEM images produced by ZfE in Figure 4.6.

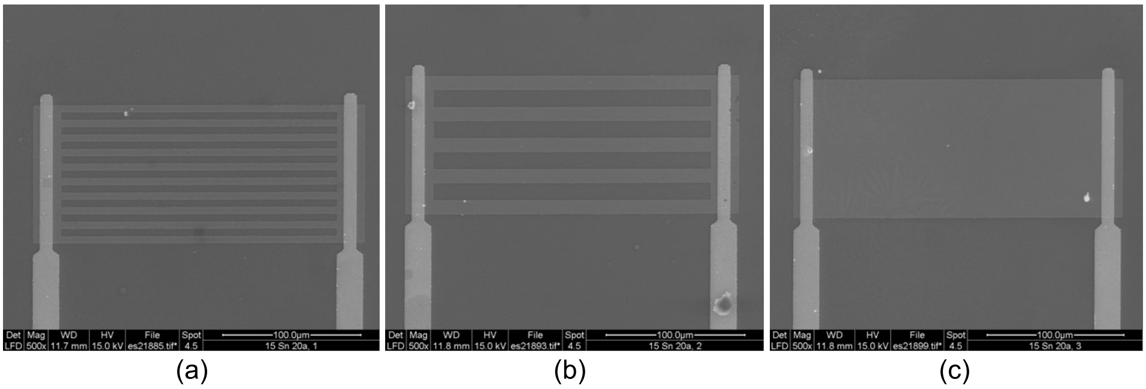
(a) (b) (c)

Figure 4.6: SEM images of the three different sensor designs of AIT using (a) ten paths, (b) five paths and (c) an area

Several of these sensor elements with different geometries were placed on a single sensor substrate. It is possible to electrically contact and investigate a certain sensor in different gas atmospheres.

- **Conductive path layers:**

The structuring of the conductive paths was performed with photolithography as already described in chapter 4.1.1. For the application of the SnO_2 layer on the substrate the method of spray pyrolysis was chosen. Thereby the sensor substrate is placed on a heating plate. $SnCl_4$ is combined with water and solved in ethyl acetate ($C_4H_8O_2$). The solution is mixed with a carrier gas in a spray head and expands through a nozzle. In this way the substrate gets covered with the solution. By shortly heating up the sensor to 500°C, a SnO_2 layer is generated on the surface due to the following reaction, caused only by the high temperature:

$$SnCl_4 + 2H_2O \rightarrow SnO_2 + 4HCl$$

In this way 50 nm thick sensing layers were created on the Si/SiO_2 substrate.
AIT currently investigates the influence of doped SnO_2 layers on the gas sensitivity. Therefore gas sensors with the same sensor geometry but different layer components were also produced. The solution used for the spray pyrolysis was mixed with $InCl_3$ to produce indium doped SnO_2. In other sensors $SbCl_3$ was used for doping. Therefore 10% indium and 10% antimony doped senor layers could be fabricated. The amount of foreign atoms in the SnO_2 lattice is very high. By using indium doped sensing layers, the sensor sensitivity due to methane could be strongly increased. In hydrogen atmosphere the antimony doped sensor

even showed the best performances. The sensor response according to carbon monoxide was improved by both foreign elements. The behaviour of the doped sensors in hydrogen sulphur was tested during our first characterization measurements.

When the sensing material was applied onto the surface and the conductive paths were structured, contacting pads were placed on the substrate to enable an easy electrical contacting of these very small sensor elements. The pads are made of 200 nm thick gold layers with a titanium undercoating. They occupy an area of 250 µm x 250 µm.

- **Annealing:**

Before measurements have been performed, the sensors were annealed at 400°C in air for about 15 minutes. This procedure enables stable sensor performances at operating temperatures up to 400°C.

4.2.2. Sensor mounting

For measurements performed at AIT the sensors were integrated onto a common chip carrier with a micro heater directly under the substrate. Therefore constant operating temperatures could be maintained during measurements by heating the sensor itself.

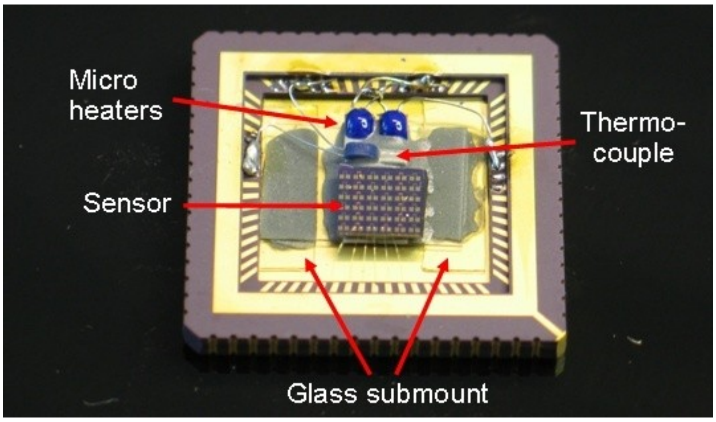

Figure 4.7: SnO_2 sensor integrated in chip carrier mounting

This heating plate is able to reach temperatures up to 400°C, which is the maximum temperature tolerable for the chip carrier. Our characterization measurements were planned to be performed at higher temperatures. Therefore a new sensor mounting suitable for applications above 400°C had to be developed.

The new mounting consists of a ceramic tube and a ceramic plate with a total length of 22 cm. On the ceramic plate eight conductive paths made of gold were applied by screen printing. The paths are connected to wires at the end of the ceramic plate by soldering.

Figure 4.8: High temperature sensor mounting from AIT

The wires were led through a ceramic tube, which was tightened with epoxy resin. The soldering connections are able to withstand temperatures up to 400°C. The very long geometry of the ceramic elements was chosen to enable a cooling of the soldering connections and wires. The sensor itself is placed at the very top of the ceramic plate and fixed with a ceramic adhesive. In this region of the mounting the temperature can reach values up to 800°C. The electrical contacting between the sensor elements on the substrate and the Au conductive paths was performed by using gold bonding wires. Due to the eight available conductive paths, it is possible to connect four sensor elements simultaneously. Therefore it is possible to change the measured sensor by shifting the current supply to two different wires.

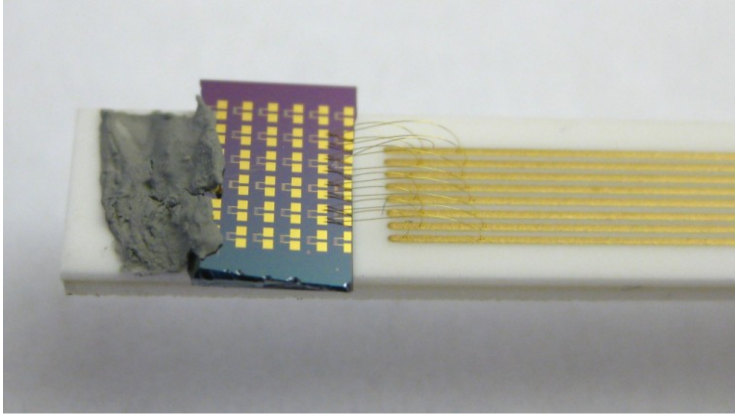

Figure 4.9: SnO_2 sensor fixed at the top of the mounting and connected by bonding wires

The disadvantage of this mounting concept is that the sensor can not directly by heated, because no heating plate can be used in this configuration. Therefore AIT is currently searching for possibilities to integrate a micro heater beneath the sensor. In our measurements it was necessary to heat up the gas stream to produce a certain sensor temperature.

The mounting shows a maximum diameter of 12 mm and can be integrated into a pipe system by using a Swagelock T-fitting. Due to the geometry of the ceramic tube, which is not perfectly round, it is very difficult to reach gas tightness with this configuration.

4.3. $GaPO_4$ microbalance from AVL

Piezoelectric microbalances made of gallium orthophosphate are able to operate in temperature region up to 970°C. This is a great advantage compared to quartz resonators, because the piezoelectricity disappears at 573°C in SiO_2. Also the piezoelectric effect is twice as high in $GaPO_4$ as it is in SiO_2. These properties make the resonator material very capable for high temperature application. Today gallium orthophosphate microbalances are prevalently used as pressure sensors in automotive engines.

The high temperature microbalance used by AVL is fabricated in a common disc shaped design with a diameter of 7.4 mm. The crystal thickness amounts to 200 µm in the middle of the disc. The resonator is grinded plan-convex, which leads to a decreased thickness at the outer side of the crystal. The grinding causes a smaller distribution of the oscillation amplitude. The discs are cut out of a $GaPO_4$ single crystal under a cut angle of Y-11.1°. Afterwards the surface is grinded, polished and finally lapped. According to the cut angle the resonator should show a defined temperature dependence of the oscillation frequency with maximum temperature stability around 400°C.

4.3.1. Resonator electrode material

To induce an oscillation in a thickness shear mode resonator, two electrodes must be placed on opposite sides of the crystal. An alternating potential is applied to these electrodes and causes a periodic deformation of the material. The resonators investigated in this project used the so called “dovetail geometry” for the electrode design. This configuration consists of a circular area in the middle of the crystal with a diameter of 3.6 mm. This region is the active area of the microbalance, where the oscillation takes place. In real resonators the oscillation is not totally limited to this area. To decrease the damping of the oscillation the crystal should only be mounted at the outer rim, with a maximum distance from the active area. For this purpose a dovetail formed electrode area leads the applied potential from the crystal edge to the active area in the middle.

Common electrode materials for piezoelectric microbalances are gold or platinum. If a gold layer is applied, it is necessary to use an undercoating, because gold adheres very badly to $GaPO_4$. Usually a very thin nickel-chromium undercoating of about 20 nm is located beneath a much thicker gold layer. For high temperature applications gold electrodes are not suitable because the undercoating diffuses into the gold layer easily. Therefore we chose a 500 nm platinum layer for our resonator electrodes, which was applied to the crystal by sputtering. In this case it is not necessary to use an undercoating because platinum adheres very well to gallium orthophosphate.

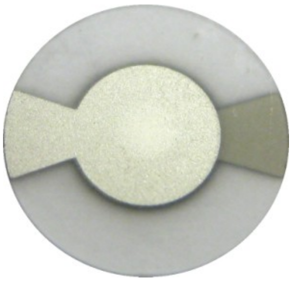

Figure 4.10: $GaPO_4$ microbalance with dovetail formed electrodes

In the course of several tests, concerning the use of microbalances as oxygen sensors, $GaPO_4$ crystals coated with 300 nm Pt electrodes and additionally 300 nm TiN and 300 nm

Ni were investigated. These extra layers were located in the active area of the sensor. The titanium nitride was used as undercoating, while the nickel layer increase the adsorption of oxygen atoms on the resonator surface. In order to investigate the mass change of the resonators in oxidizing and reducing atmospheres, thermo gravimetrical measurements were performed at the Montan Universität Leoben. This analysis enables the detection of mass changes in alternating oxidizing and reducing conditions up to 1 µg accuracy. 22 $GaPO_4$ crystals were stacked into a quartz cup and put onto the thermo gravimetric balance. The oxidizing atmosphere was generated by flooding the measurement chamber with argon and 20 vol-% O_2. Argon and 2.5 vol-% H_2 acted as the reducing gas atmosphere. The oxidizing and reducing phases were separated by flushing periods with pure argon.

A mass increase during the oxidizing phase due to the oxidation of the Ni layer and again a mass decrease under reducing atmosphere was expected. Theoretically the mass increase due to the oxidation of Ni was calculated with – 0.17mg by considering the volume of nickel at the crystals and the assumption that each nickel atom becomes oxidized. The mass increase during the first oxidation phase showed a similar value to the theoretical one. An extremely strong, almost linear, mass loss was registered under reducing conditions, which could not be explained by oxidizing or reducing processes. During a second oxidizing phase, again a mass increase was detected. Under reducing conditions the mass loss due to the reduced Ni was detected, followed by the same unexplainable decrease as during the first reducing phase.

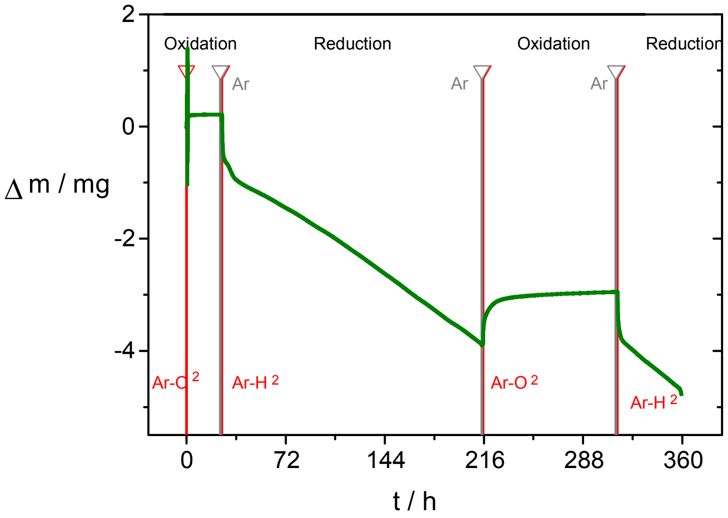

Figure 4.11: Relative mass change of 22 resonators with Pt-TiN-Ni electrodes detected with thermo gravimetric analysis at 800°C

In order to find out the reason for this unexpected behavior and to identify the concerned material, which could be $GaPO_4$, Pt, TiN or Ni, electron-microscopic analysis were performed. Even a light microscope investigation showed a mutation of the electrode layer. Scanning electron microscopy (SEM) investigations and an energy dispersive x-ray (EDX) analysis performed by ZfE indicated defects of the electrode layers. Three zones in the electrode area pictured in Figure 4.12 (b) were defined and investigated with EDX. Zone 2 and 3 consisted of $GaPO_4$, Pt, Ti and Ni, while zone 1 showed only gallium orthophosphate and therefore marks a hole in the electrode area. As consequence the electrical contacting of the resonators was impossible and no oscillation could be induced. This investigation however did not answer the question, which of the four concerning materials caused the unexpected mass decrease.

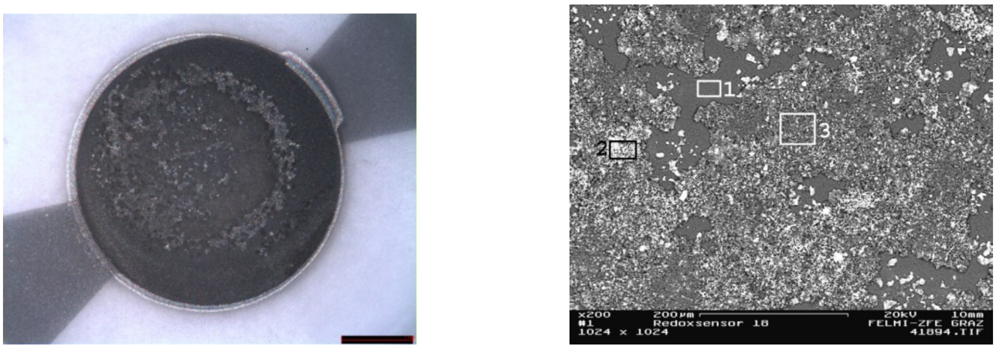

(a) (b)

Figure 4.12: (a) Light microscopy and (b) SEM image of Pt-TiN-Ni layers

In order to identify the reason, a second thermo gravimetrical measurement was performed. This time pure uncoated $GaPO_4$ crystals and resonators with 300 nm platinum electrodes were investigated. The conditions should lead to explicit conclusions about the behavior of the crystal and the platinum electrode at 800°C. At reducing atmosphere pure $GaPO_4$ showed a small mass decrease of -0.0002 %/h, caused by the reduction of the oxygen atoms out of the $GaPO_4$ crystal. The platinum coated crystals were subjected to the same nearly linear mass loss as in the first thermo gravimetrical measurement. The decrease has a value of -0.002%/h and is therefore much bigger than the one of pure $GaPO_4$. When the coated crystals were exposed to the reducing gas atmosphere, a temperature decrease to 700°C and afterwards to 600°C was performed. In these temperature regions the mass loss immediately stopped.

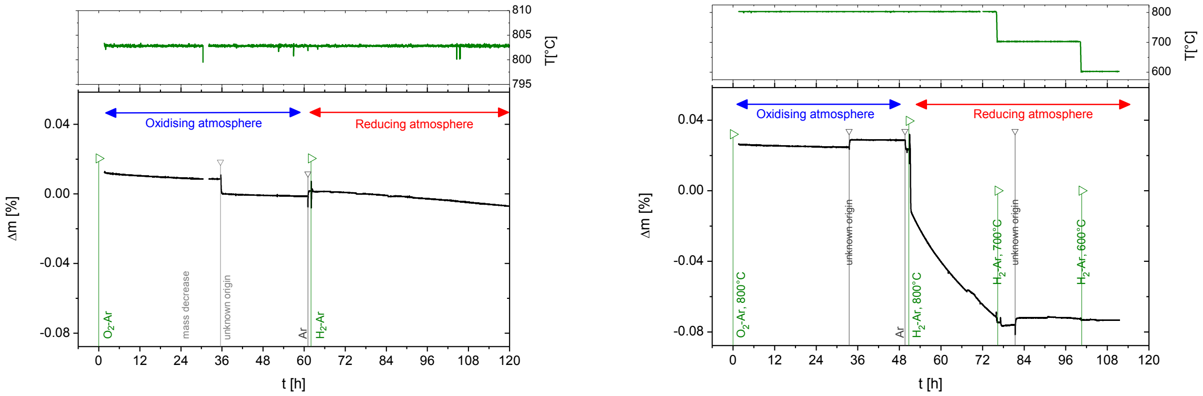

(a) (b)

Figure 4.13: Relative mass change and measurement temperature of (a) uncoated $GaPO_4$ and (b) crystals with 300 nm thick platinum electrodes at 600°C, 700°C and 800°C

The conclusion of this second thermo gravimetrical analysis is that the platinum electrode layer is unstable in reducing atmosphere above a temperature of 700°C. The possibility of an evaporation of the platinum layer was discussed, but this explanation is implausible considering the evaporation energy of platinum. The evaporation of platinum would only cause a mass decrease in the range of several picogram. Most probably catalytic reactions take places at the interface between the gallium orthophosphate and the platinum electrode layer. If atomic hydrogen is produced by these reactions, the reduction of oxygen contained in $GaPO_4$ is very probable.

After the thermo gravimetrical measurements the crystals were again investigated by ZfE using a scanning electron microscope and EDX analysis. In this case the defects in the electrode layers appeared to be even more dramatic, as can be seen in Figure 4.14. Consequently platinum electrodes are unsuitable for applications at temperatures above 800°C in reducing gas atmospheres.

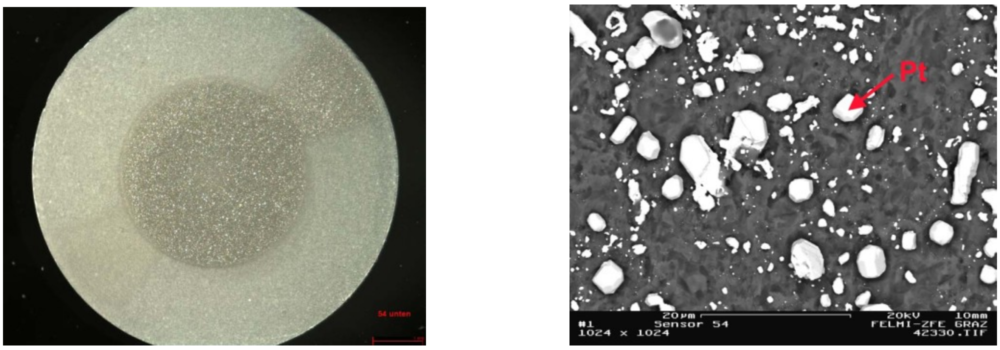

(a) (b)

Figure 4.14: (a) Light microscopy and (b) SEM image of platinum coated resonator

In order to realize a piezoelectric gas sensor applicable in reducing gas atmospheres at high temperatures, an alternative electrode material needed to be developed. This is a difficult challenge, because platinum is a very common material and very suitable for most microbalance applications. Therefore some first investigations have been performed according to high temperature electrodes applicable in reducing gas atmospheres. In cooperation with our crystal manufacturer Piezocryst several electrode and undercoating materials have been discussed. The most suitable electrode material on gallium orthophosphate for high temperatures, investigated by Piezocryst is an Indium Tin Oxide composition. However, this material cannot be used in reducing atmospheres, because it is easily reduced. Another possibility would be the deployment of a platinum iridium (10%) alloy, but this concept has never been tested before on gallium orthophosphate, because of the high costs. Also a composition of palladium and 13% chrome was discussed. This possibility was neglected because of the very high resistance of the material. It has also been considered to use a gold electrode with a titanium undercoating. However, this concept had already been tested by Piezocryst and had shown a strong oxidation of the titanium layer at temperatures above 600°C in air.

Other discussions led to the possibility to use a gold electrode layer with a molybdenum undercoating. This was a new approach because no experimental data is available for this layer configuration on $GaPO_4$ under such conditions. Molybdenum seems to be suitable because of its high ductility and therefore the ability to relieve mechanical stress between the crystal and the electrode layers at high temperatures, but the adhesion of molybdenum on $GaPO_4$ crystals had never been tested before. 18 gallium orthophosphate crystals were coated with a molybdenum undercoating and 500 nm gold electrodes by sputtering at AIT. Because the optimum layer thickness of the undercoating was unknown three different thicknesses were realized. Six crystals where coated with 25 nm Mo, another six with 50 nm Mo and the last six ones with 100 nm Mo.

The consistency of the coating was tested again with a thermo gravimetrical measurement. This time the testing temperature started at 600°C and was later increased to 700°C and 800°C. All $GaPO_4$ crystals were stacked into a quartz cup during the measurement. The sensors were exposed to argon and 20vol-% oxygen for a time period of 24 hours. Afterwards the chamber was flushed with pure argon for one hour. The reducing atmosphere containing of argon and 2.5vol-% H_2 was injected for the next 24 hours. During the next measuring circle the same gas conditions were arranged at 700°C and finally again at 800°C.

The oxidizing and reducing phases at 600°C and 700°C caused only insignificant mass changes due to unknown reactions, which were not further investigated. In reducing atmosphere at 800°C a rapid mass decrease over the whole 24 hours was detected, which slightly decelerated after the first 12 hours. Considering that the evaporation energy of gold is smaller than the one of platinum, an evaporation of the gold layer would be a possible explanation for this behavior. But since this effect would also occure in oxidizing atmosphere, the reason for the strong mass decrease at 800°C is most probable caused by catalytic processes.

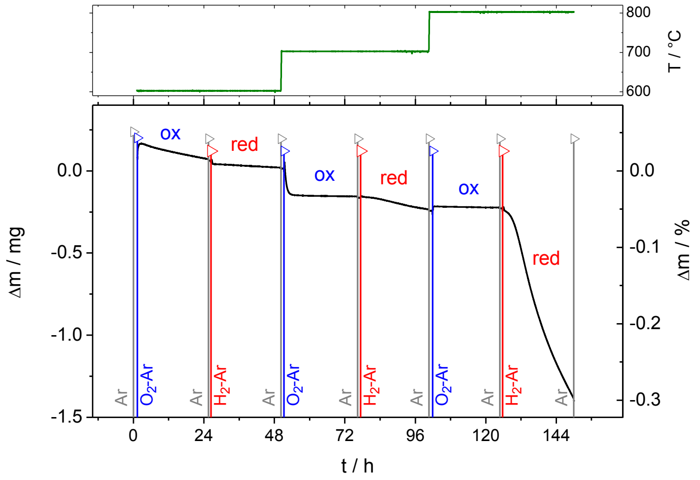

Figure 4.15: Relative mass change and measurement temperature of resonators coated with molybdenum and gold

Comparing the relative mass loss per unit time of the Mo/Au-coated crystals with those of the Pt-coated ones at 800°C in reducing atmosphere, a 4-6 times larger decrease of Mo/Au than of Pt was detected. The conclusion of these two thermo gravimetrical measurements is that Pt electrode layers are much more stable at 600°C and 700°C than Mo/Au electrodes. They also show a smaller mass decrease at 800°C.

According to these results and the current absence of an alternative electrode material for high temperature applications in reducing atmosphere, it was decided to use platinum electrodes but to avoid measurements at temperatures above 700°C in reducing gas atmospheres.

4.3.2. Sensor mounting

Common mountings for disc shaped microbalances are using clamping methods for stable fixation of the crystal. One big advantage of these concepts is the reversibility. The resonator in the mounting can easily be changed, because it is not fixed with any adhesive or bonding method. Therefore it is possible to produce one sensor mounting and use it for many different measurements. For our high temperature microbalance it was necessary to use a mounting, which is capable for temperatures up to 800°C in oxidizing and reducing atmospheres. The common mounting system, as it is illustrated in Figure 4.16 (a), is not suitable for such high temperatures. Additionally it can not be used in gas flows with high pressures.

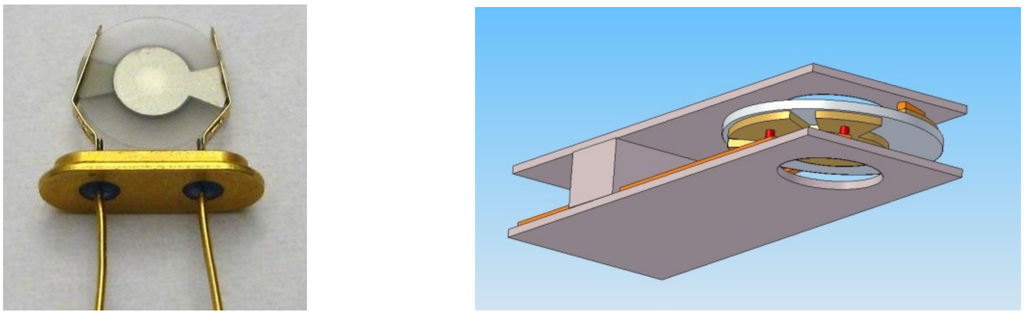
(a) (b)

Figure 4.16: (a) Common sensor mounting and (b) new concept for disc shaped resonators

According to these limiting factors a new mounting concept was designed by the Institute of Sensor and Actuator Systems (ISAS) at the Technical University in Vienna. It includes two ceramic elements on both sides of the crystal. Conductive paths are applied to the ceramic plates. The design enables the electrical contacting of three different electrodes on each resonator surface. This will be necessary when the gas sensitive metal oxide nanolayers are deposited onto the microbalance. A high frequency oscillation could be induced while simultaneously contacting the semiconductor gas sensing layer on the crystals surface. The most difficult part of the sensor mounting is the fixation of the resonator between the ceramic plates. Therefore two different methods have been investigated. The first one uses stencil printed bumps made of gold paste. The second fixation was planned with stainless steel micro spheres, which enable defined distances between the resonator and the ceramic plates.

The mounting concept was realized by using Al_2O_3 for the fabrication of the ceramic plates. The substrates need to be as long as possible, because the attached wires are not suitable to withstand such high temperatures as the resonator at the top. Conductive paths made of gold paste were screen printed on the ceramic plates and baked for one hour at temperatures up to 850°C. They are 12 µm high and show a width of 1 mm. Because it is not possible to apply layers longer than 8 cm by using screen printing, the length of the substrates was limited by this factor. If longer plates had been used, two separate printing processes would have been necessary, leading to several disadvantages. The top of the substrate was formed as a circle with a hole in the middle, to enable gas adsorption on the active area of the microbalance. The conductive path on the substrate leads to one of the fixation points, which also serves as electrical contact. When the crystal is placed on the ceramic plate, the electrode has to be connected to the conductive path. The two substrate plates belonging to one sensor mounting are illustrated in Figure 4.17.

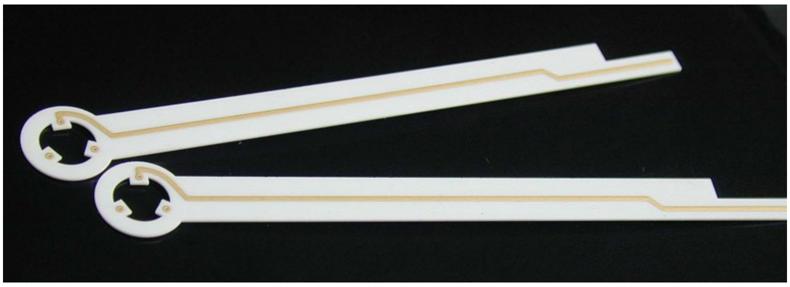

Figure 4.17: Ceramic substrates including conductive paths for high temperature microbalance mounting

In case of the first fixation method of the crystals between the two substrates, three bumps, with a diameter of 0.9 mm, were applied to the plates by stencil printing. One of the bumps is attached to the conductive path, while the other two are placed in defined distances around the ceramic circle. After the printing the 40 µm high bumps are baked for one hour at temperatures up to 850°C. This process was performed twice, what lead to a total bump height of 80 µm. This value was approved by investigations with a surface profilometer. Such a profile is illustrated in Figure 4.18.

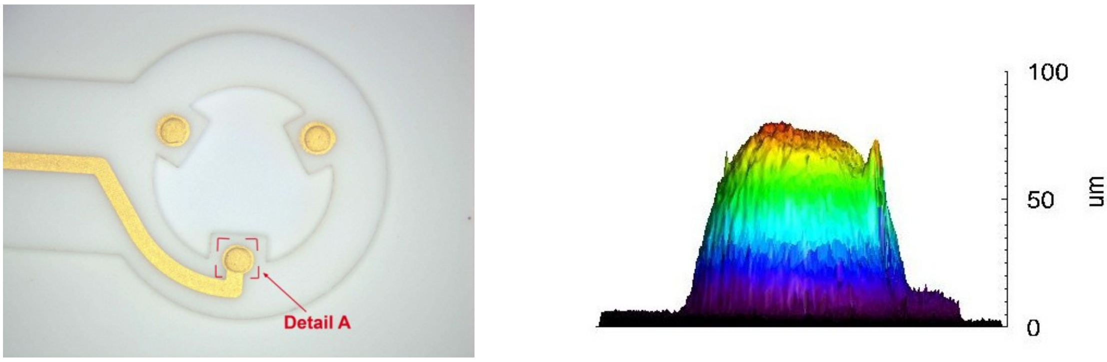

Figure 4.18: Gold bumps on the ceramic substrate and the height profile of detail A

In order to fix the gallium orthophosphate crystal on these bumps, a third gold layer with a diameter of 0.5 mm was applied to the bumps. Additionally the same bumps were printed onto the crystal. By using a vacuum forceps the crystal was placed onto the bumps on the substrate, while the gold paste was still wet. Now this part of the mounting including the resonator was baked together for one hour. Distance pieces made of Al_2O_3 were attached to the ceramic plate to produce a distance between the two ceramic parts of the mounting. The fixation procedure was repeated with the second ceramic plate and then the assembled mounting was baked again.

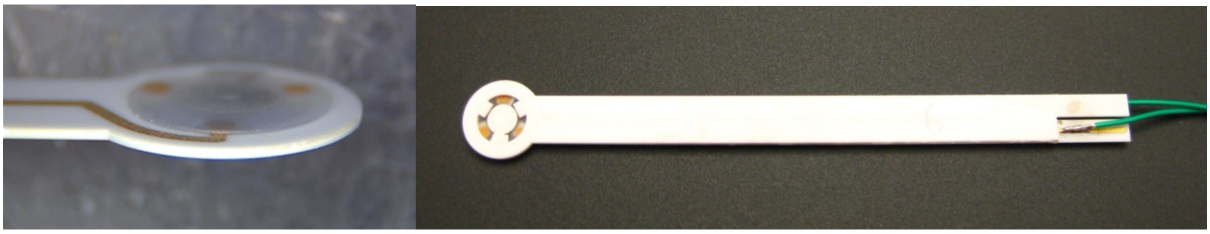
(a) (b)

Figure 4.19: (a) Crystal mounted on one ceramic substrate and (b) fully assembled mounting

On the opposite side of the ceramic substrate, the plate has a cut-out which enables the electrical contacting of the conductive paths. Teflon coated wires were soldered to the gold layers. Because Au/Sn was used as solder material, this connection is able to withstand temperatures up to 250°C.

The second fixation method investigated, uses micro spheres, with a diameter of 300 µm, as distance pieces and simultaneously as electrical connection. This concept was developed because it enables a well defined distance of 200 µm between the crystal and the ceramic substrates. Additionally, the contacting area on the crystal could be decreased, which causes lesser damping of the microbalance oscillation. For the assembly of the micro spheres modified ceramic substrates had to be fabricated. At those places where the bumps are located in the other concept, holes were drilled into the ceramic plates. The spheres were fixed in these borings with gold paste. This paste has also been used for the connection between the crystal and the spheres. The assembling and baking processes were the same as for the first mounting concept described above.

A disadvantage of the used metallization is the connection between the gold bumps and the platinum electrodes of the resonators. This leads to higher contact resistances and a diffusion of the gold atoms into the platinum layer at high temperatures. Alternatively, the use of platinum paste instead of gold was discussed. Tests with platinum paste on $GaPO_4$ resonators showed a high number of crystal damages, due to the lower ductility of platinum. Therefore gold was preferred as the more suitable metallization for this mounting concept. Furthermore the thermal expansion coefficient of gallium orthophosphate depends on the crystallographic axes but has a maximum value of 12.8 10^{-6} /K, while the micro spheres made of stainless steel show 16 x 10^{-6} /K. Gold is characterised by an expansion coefficient of 14 x 10^{-6} /K. Because gold shows the highest ductility of all metals, it is very suitable to compensate the different expansion of the materials in the mounting.

5. Measurements

The aim of the project is the development of a highly sensitive, highly selective and very rapid gas sensor for the detection of hydrogen sulfide and water. Two different chemiresistor gas sensor concepts were investigated in course of this thesis. Comparable characterization measurements were performed in an equal test setup. Therefore a test bench at AVL was utilized and the sensors produced by AIT and NTCW were characterized concerning their response to hydrogen sulfide and water.

The detected sensor responses included sensitivity, response time and recovery time as described in chapter 1.3.3. The response time was defined as the time period from the moment of H_2S inlet to the point when the resistance signal reaches 90% of its final value. Sensitivity values were calculated by dividing the difference of the last resistance value before the H_2S inlet and the smallest resistance value during the H_2S phase by the last value before the H_2S inlet. The sensitivity was indicated in percent by multiplying the result with a value of 100:

$$S = \frac{R_{air} - R_{gas}}{R_{air}} \cdot 100$$

5.1. AVL test bench setup

5.1.1. H_2S measurements

Hydrogen sulfide measurements with gas sensors of NTCW and AIT were performed at the AVL low temperature test bench, which is mostly instrumented for performance tests with low temperature fuel cells. The standard configuration of the test bench includes several gas connections and corresponding mass flow controllers. Gases like air, H_2, N_2 and synthetic air are always available. A new mass flow controller was installed in order to supply H_2S for the desired characterization measurements. It had been calibrated for 10 ppm H_2S in nitrogen, which was provided at the test bench in a 10 l gas bottle with 150 bar. The other required gases were nitrogen and synthetic air, which were available in 50 l gas bottles with 200 bar. The H_2S/N_2 gas mixture had to be combined with synthetic air (80% nitrogen and 20% oxygen) to provide enough oxygen to the sensor surface for the adsorption reactions described in chapter 1.2.2. The gas flow rate was fixed at 1000 sccm/min for each gas component, which leads to a total flow rate of 2000 sccm/min. Therefore the adjustable H_2S concentration was 5 ppm and the reference gas was a mixture of synthetic air and nitrogen with a total oxygen concentration of 10%. This configuration makes it possible to keep the oxygen concentration constant during the whole measurement.

Before the measurements started, several modifications had to be performed at the test bench, including a construction for preheating the gases. The gas inlet pipes leading to the measuring chamber were wrapped with heating cords und thermally insulated with half shells made of insulating material. This test assembling enabled preheating of the gas flow, which was necessary during the AIT sensor tests because the corresponding sensor mounting did not include a local heating unit. The gas outlet behind the sensor remained open. Therefore the pressure in the pipes was close to atmosphere. The gases were removed by a suction unit included in the test bench.

5.1.2. H_2O measurments

In order to produce a certain amount of humidity in the gas flow an evaporator had to be used. Synthetic air was used as totally dry reference gas into which a certain amount of water could be evaporated. The mass flow rate was again regulated to 2000 sccm/min and kept constant during the whole measurement. The H_2O-amount could be adjusted between 3.5 and 10 ml/min. The water was mixed into the air flow and therefore slightly changed the total gas flow rate at the sensor. The differences were considered as small enough to be neglectable.

The measurements with the gas sensors from AIT were performed with a different water evaporator than during the NTCW tests. Concerning the parameters of this evaporator the air flow rate had to be increased to 3000 sccm/min. This modification is considered to have no significant influence on the results.

5.2. Characterization measurements of WO_3 sensors

These gas sensors, using tungsten trioxide nanoparticles as sensing material, were developed by NTCW. The sensor response to hydrogen sulfide had already been tested, but the test parameters were different to those of our characterization. 10 ppm hydrogen sulfide in synthetic air had been used as measuring gas by NTCW. As enough oxygen is present at the sensor surface in this way, a gas mixture was not necessary and the total H_2S concentration in the gas flow was constantly at 10 ppm. Also a much smaller gas flow rate of 10 sccm/min had been used. Concerning the sensor response to water, the tungsten trioxide sensors of NTCW have never been investigated before. Considering the adsorption processes mentioned in chapter 1.3.2 and investigations concerning water at WO_3 surfaces described in [Poh00], reactions caused by water molecules should lead to measurable conductivity changes of the sensor.

5.2.1. H_2S measurements

In order to prove the basic applicability for H_2S sensing of tungsten trioxide nanosensors developed by NTCW, characterization measurements were performed at the AVL test bench as described in chapter 5.1.1. The intention was to prove a definite sensor response at the presence of H_2S in a gas flow. Additionally, the response time was of great interest. The measurement chamber constructed by NTCW and mentioned in chapter 4.1.2, was attached to the heatable gas inlet pipes at the test bench. A heating plate control and a Keithly Sourcemeter were connected to the relating electrical connections of the measuring chamber and also to a computer, which contains special LabVIEW software as described in [Pos09]. A temperature sensor was placed inside the chamber close to the sensor, to verify the measurement temperature.

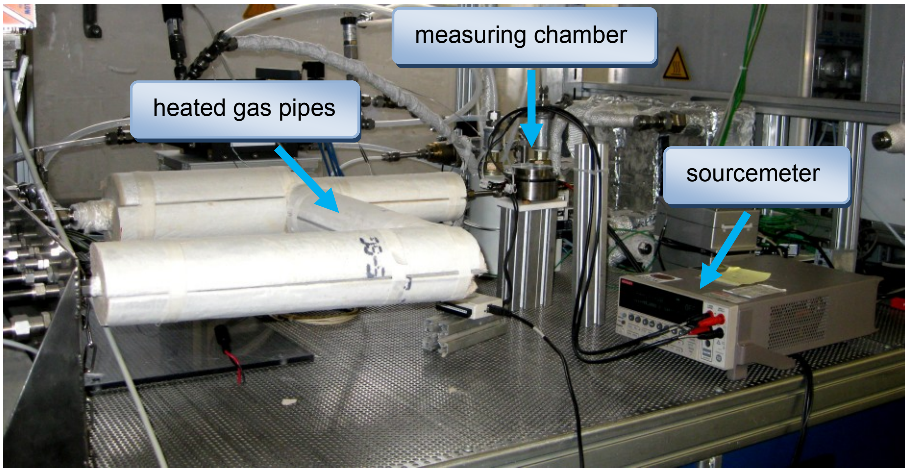

Figure 5.1: NTCW measuring chamber connected to AVL test bench

Two WO_3 sensors with different conductive path geometries were tested. One sensor was fabricated with the formerly used geometry, using gold conductive paths with a line width and spacing of 200 µm. The other one showed a miniaturized geometry with a line width of 50 µm. In both cases the conductive paths were applied on top of a Si/SiO_2 substrate and WO_3 nanoparticles were placed upon the conductive paths.

At the beginning of the measurement a background gas atmosphere consisting of synthetic air and nitrogen was generated in the measuring chamber. During the H_2S phase the nitrogen support was switched off and instead 10 ppm H_2S in N_2 were mixed with the same amount of synthetic air. The O_2 concentration during the following flushing period had to stay constant to produce reasonable test results. The increase of oxygen at the sensor surface would have led to a strong decrease of the sensor conductivity. Therefore the background atmosphere was generated by the same amount of synthetic air and nitrogen as during the H_2S phase, just without containing any hydrogen sulfide. The gas mixture always consisted of 1000 sccm/min synthetic air and 1000 sccm/min pure nitrogen or alternatively 10 ppm H_2S in nitrogen. Therefore the O_2 concentration remained constant at a value of 10%.

The tests were performed without preheating the gas flow. The measuring temperature was generated locally by a heating plate beneath the sensor substrate. The response to H_2S was tested at five different temperatures: 100°C, 150°C, 200°C, 300°C and 400°C.

All measurements showed a clear decrease of the sensing layer resistance during the presence of H_2S in the gas flow. A typical resistance signal of a tungsten oxide gas sensor is demonstrated in Figure 5.2. This measurement was performed with a sensor using the common conductive path geometry with a line width of 200 µm. The measurement was performed at 200°C. The strong decrease of the sensor resistance at the beginning of the H_2S phase, which produced resistance values beneath all other values measured in H_2S atmosphere, appeared due to an electrical input, caused by switching the mass flow controllers at the test bench. This unrequested effect could be avoided at later measurements. Concerning this measurement a mean response time of 10 sec and a mean sensitivity of 87% was achieved. The mean values were calculated by using the parameters of all three H_2S phases during the measurement.

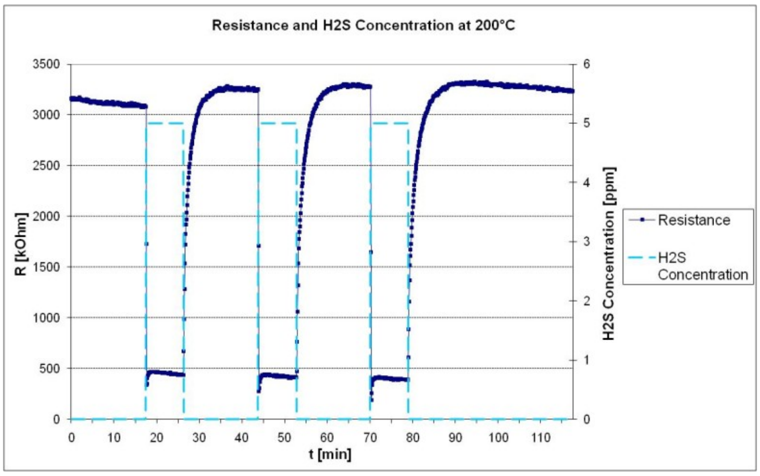

Figure 5.2: Sensor response to H_2S of a 200 µm geometry sensor at 200°C

The sensitivity values for both sensor geometries are compared in Figure 5.3. Both sensors showed very high sensitivities at low temperatures up to 200°C. At higher temperatures the sensitivity of the 200 µm geometry sensor decreased down to 28% at 400°C. However the minimized geometry sensor showed the maximum sensitivity of all performed measurements at 300°C with a value of 89% and decreased only slightly at 400°C to 71%. As only two different sensors have been investigated, it is not possible to give a secure statement about better sensor behaviors of minimized geometry sensors at high temperatures. More research would be necessary concerning the advantages of minimized conductive path geometries.

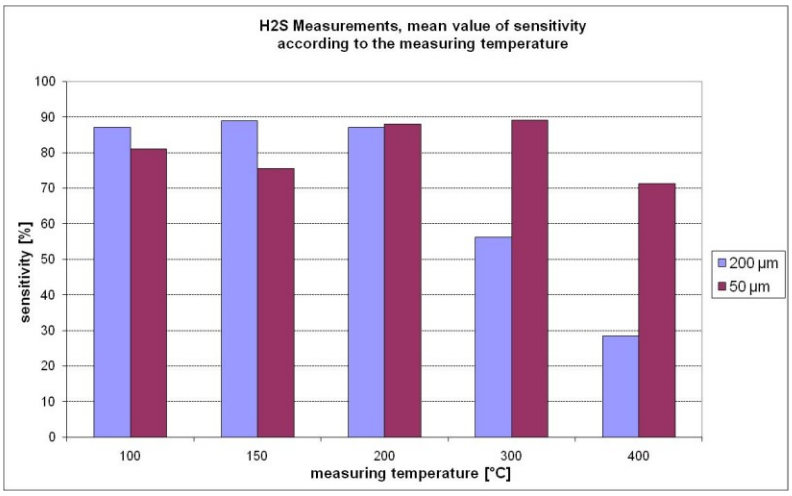

Figure 5.3: Mean sensitivity of two sensors with different conductive path geometries at different measurement temperatures

As expected, the detected response time strongly varied at different measuring temperatures. The minimum response time of the considered WO_3 sensors amounted to 7 sec and could be achieved at an operating temperature of 200°C. Formerly performed tests at NTCW showed response times in the range of several minutes, due to the much smaller gas flow rate in the chamber (10 sccm/min). Therefore the measurements proved the possibility to fasten the sensors response by increasing the gas flow rate. Generally the sensor responses were very fast at high temperatures. As expected, the recovery times were much longer than the response times, according to the strong adhesion of H_2S to the surfaces. A significant difference between the two investigated sensors, concerning the response and recovery times, could not be detected upon 200°C. The 200 µm geometry sensor showed a quite bad behavior during the measurement at 400°C. The signal was noisy and showed a small sensitivity to H_2S. Therefore the recovery time could not be defined reasonably and is missing in the diagram below.

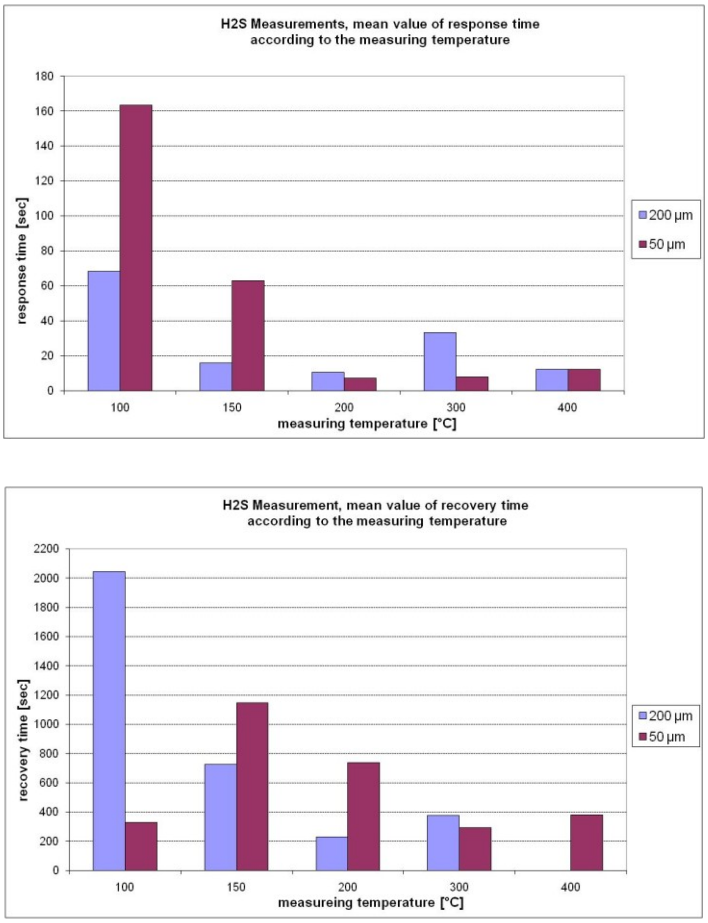

Figure 5.4: Mean response and recovery times of the two investigated WO_3 sensors according to the measuring temperature

The sensor response at low temperatures was rather slowly. This behavior was expected, because of the bigger adhesion of hydrogen sulfide to the metal oxide surface at low temperatures. Beneath 150°C, H_2S molecules are mostly adsorbed by physisorption. At these temperatures the basic resistance of the sensors strongly increases [Pos09]. Therefore tungsten trioxide sensors are usually used in temperature ranges above 150°C. During the characterization measurements, tests were performed at 100°C. They led to high sensitivity values, but to very slow sensor reactions.

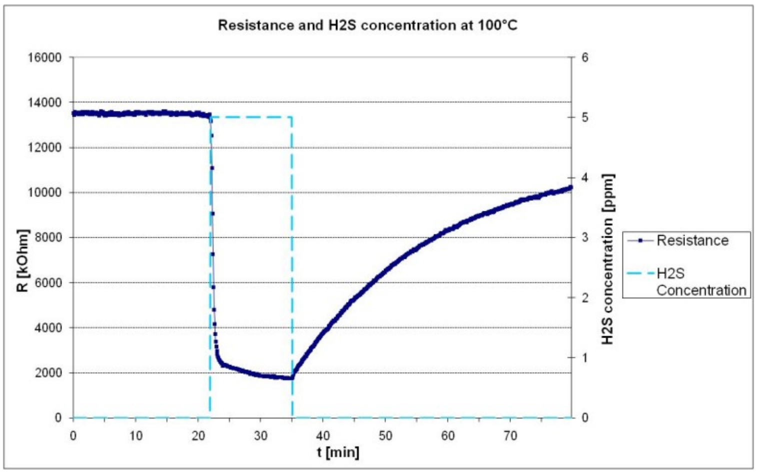

Figure 5.5: 200 µm geometry sensor response to H_2S at 100°C

A typical sensor response to H_2S at 100°C is demonstrated in Figure 5.5. The corresponding response time of the investigated 200 µm geometry sensor amounts to 68 sec. Compared with measurements at higher temperatures this value is very high. However, the 50 µm geometry sensor showed an even longer response time at 100°C, as can be seen in Figure 5.4. According to the physisorpion of hydrogen sulfide molecules, the recovery of the sensor was extremely slow. In the case of the second investigated sensor with the 50 µm geometry, the resistance did not fully recover after the H_2S phase. Therefore the resistance signal showed a saturation value lower than the basic resistance before the H_2S phase. This behavior led to a much smaller recovery time of the sensor, but it is not significant, because the sensor surface was probably not fully void of the hydrogen sulfide molecules.

These measurements were performed in a range too small to produce really significant results. Additional testing of sensors with different line spacing would be necessary to definitely prove the higher sensitivities of miniaturized sensor elements at high temperatures. A second problem is the reproducibility of the tests. Because the measuring chamber is still a prototype, the electric conduction of the conductive paths is influenced by user specific circumstances. A similar electric conduction at measurements with different sensors can not be guaranteed, which leads to varying values of the basic resistance. The characterization measurements led to important results, though. The general qualification of WO_3 nanoparticle layers for detecting very small concentrations of H_2S could be proved. Very high sensitivities up to 89% could be achieved. The sensing effect was monitored down to a temperature of 100°C, which was lower than expected. Additionally, the response times were successfully decreased by using a bigger gas flow rate. All these results showed the great capability of WO_3 nanoparticles for highly sensitive and extremely fast H_2S sensors.

5.2.2. H_2O measurements:

The tungsten trioxide gas sensors from NTCW had never been tested concerning their sensitivity to water adsorption before. The general influence of humidity on metal oxide gas sensors is well known. This explains why measurements in certain gas atmospheres are always performed in synthetic air instead of ambient air. Water adsorption can also lead to coadsorption of other gases at the metal oxide surface and therefore influence the sensor response.

During the corresponding measurements the gas flow was heated by the heating plate beneath the sensor, which guaranteed a constant sensor temperature. Measurements in humid gas atmospheres were performed at 200°C and 300°C with three different WO_3 sensors. The water amount in this configuration was limited by the parameters of the evaporator and could be varied between 3.3 and 10 ml/min.

Although the presence of water at the metal oxide surface should lead to a measurable change in the sensor conductivity, no clear responses could be detected in these measurements. At low H_2O amounts of about 3.3 ml/min the sensors did not show any change of resistance. Only when the amount of water was increased to values higher than 4.2 ml/min, a very small reaction could be detected. Water amounts above 5 ml/min always led to short circuits at the sensor surface and therefore to a loss of the resistance signal. Generally, reproducible sensor responses due to the presence of water molecules at the metal oxide surface could not be achieved.

5.3. Characterization measurements of MoO_3 sensors

Additionally to the already demonstrated applicability of WO_3 nanoparticles as H_2S sensors, MoO_3 nanoparticles were developed by NTCW as new sensing material. Like tungsten trioxide also molybdenum trioxide is a well known material for chemiresistor gas sensors, but conventionally used in bulk geometries. These sensors were planned to be characterized at the AVL test bench for the first time. Unexpectedly the electrical contacting of the MoO_3 sensors failed and no reasonable sensor resistance could be detected. In order to identify the reason for the contacting problem an electron microscopic analysis was performed. The pictures generated by a scanning electron microscope showed damages in the conductive path layers. Figure 5.6 shows a back scattered electron picture of the molybdenum trioxide applied to one of the conductive paths.

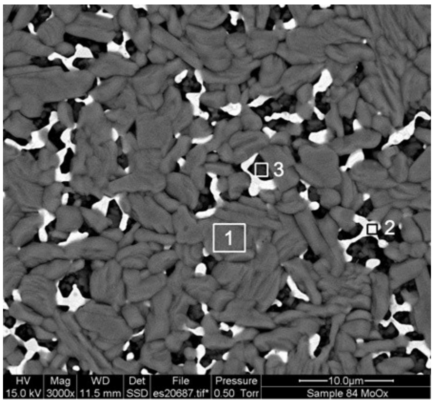

Figure 5.6: SEM image of conductive path and MoO_3 nanoparticle layer (zone 1: mainly Mo, zone 2: mainly Au, zone 3: mainly Si)

Three different areas can be identified due to the atomic number of the containing elements. Therefore an energy dispersive x-ray analysis was performed at the three positions marked in Figure 5.6. In zone 1 the analysis mainly showed molybdenum. Therefore these grey areas illustrate the MoO_3 on the surface. In zone 2 the major element was gold. These two elements were expected to be at the sensor surface, due to the gold conductive paths and the molybdenum nanoparticles. An inappropriate result was however found in zone 3, where a big amount of silicon was detected. This is only possible if the gold layer is incomplete. Obviously the conductive paths beneath the MoO_3 nanoparticles had been damaged. It is very probable that the destruction was caused by the pulsed laser deposition process, employed for production and application of the molybdenum nanoparticles. Additionally, the EDX analysis showed a contamination of the MoO_3 layer with sodium, magnesium, calcium and potassium. These impurities also must have been applied to the sensors during the pulsed laser deposition. According to these results the application process of MoO_3 on the sensor elements has to be reconsidered.

5.4. Characterization measurements of SnO_2 sensors

The gas sensing material used by AIT is tin dioxide, which is a very common bulk material for chemiresistor gas sensors. Here the focus lies on the detection of small concentrations of hydrogen, methane and carbon monoxide. So far, only little investigations have been performed concerning the detection of water, hydrogen sulfide and sulfur dioxide. Therefore the results of our characterization measurements were of great interest. The few experiments with H_2S on tin dioxide layers at AIT were performed at very different measurement parameters compared to the measurements at AVL. A gas flow of 950 sccm/min synthetic air was mixed with 50 sccm/min nitrogen containing 50 ppm H_2S. This configuration leads to a H_2S concentration of 2.5 ppm. The total gas flow rate stayed 1000 sccm/min during the whole measurement. Therefore the total gas flow rate and the H_2S concentration were smaller than during our measurements. The response of SnO_2 sensors to water has also been tested before by AIT, but not with the same sensor design as investigated at AVL.

5.4.1. H_2S measurements

The suitability of tin dioxide as gas sensitive material for the detection of hydrogen sulfide has been investigated. The sensor sensitivity to 5 ppm H_2S, the response and recovery time were characterized. Additionally to a sensor using conductive paths made of pure SnO_2, it was also possible to investigate the effect of hydrogen sulfide on tin dioxide nanolayers doped with 10% indium and with 10% antimony. These doped materials had never been tested before concerning their response to H_2S. Because the positive effect of doping was proved in methane and carbon monoxide atmospheres the influence on H_2S sensing was of great interest.

The sensors were fixed on the high temperature mounting, described in chapter 4.2.2. Because a direct heating of the sensor was not possible, the gas pipes before the sensor where brought to a certain temperature by using heating cords. Additionally, the pipes were thermally isolated. The sensor mounting was integrated into the pipe system by using a

Swagelock T-fitting. The sensor, at the top of the ceramic substrate, was placed in the middle of the fitting, which had an inner diameter of 18 mm. A photography of this construction can be seen in Figure 5.7.

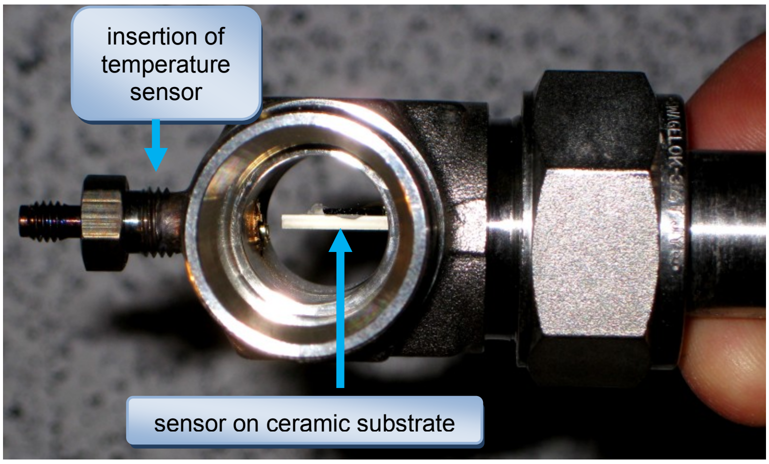

Figure 5.7: Swagelock T-fitting with inserted SnO_2 sensor

The T-fitting including the sensor mounting was also heated with a heating cord and thermally insulated. The sensor temperature was controlled by a thermocouple located close to the sensor. The temperature sensor was applied into the T-fitting opposite to the gas sensor. The ceramic tube of the mounting was clamped by a Swagelock fitting. Because the diameter of the tube was not exactly 12 mm, this connection was not gas tight. Therefore a certain part of the gas flow was leaking from the pipe, next to the sensor mounting, instead of leaving at the gas outlet. Due to the fact that this outlet remained open, the missing gas tightness was irrelevant for the measurements. As four sensors on the Si/SiO_2 substrate could be connected simultaneously, eight wires had to be attached to a circuit board. Thus it was possible to select a certain sensor for the measurements and also change it if necessary. For all measurements concerning the pure SnO_2 sensor a sensor element containing of five conductive paths, as described in chapter 4.2.1, was electrically connected. The measurements concerning antimony doped SnO_2 were performed with a sensor element containing of ten conductive paths, while the indium doped one consisted of one sensing area instead of conductive paths. The selection of the sensor elements was performed by choosing the most stable resistance signal at the beginning of the measurements. The circuit board was connected to a Keithly Sourcemeter. A measuring computer containing a LabVIEW data acquisition software was used for test controlling and data saving.

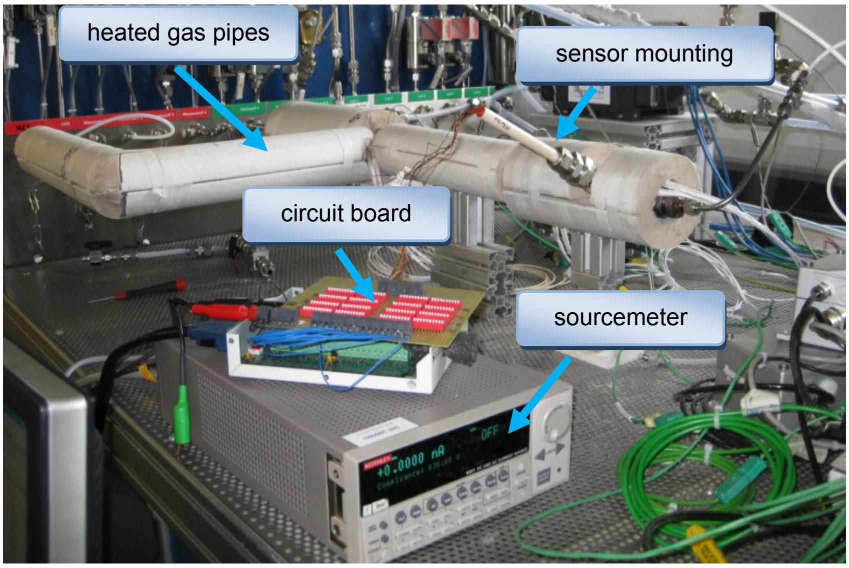

Figure 5.8: Measurement setup for experiments with SnO_2 sensors from AIT

The sensor responses were tested at four different temperatures: 200°C, 300°C, 400°C and 475°C. The test procedure was almost the same as during the NTCW measurements. The experiments started with a flushing period (synthetic air and nitrogen) of about 20 min. The following H_2S phases took about 10 min. Because the sensors showed strong resistance drifts at first, they were heated up to 400°C for about 15 min before the measurements started. This annealing procedure led to more stable sensor signals. In reducing gas atmospheres like H_2S, the tin dioxide sensor should have shown the same reaction as the tungsten trioxide one. A definite decrease of the sensor resistance was expected, but the sensor response was different. All measurements of the SnO_2, $InSnO_2$ and $SbSnO_2$ sensors at 200°C, 300°C and 400°C showed increasing resistance signals due to the presence of hydrogen sulfide in the gas flow. Such a reaction was expected to occur only if oxidizing gases are adsorbed at the sensor surface. The H_2S tests performed by AIT did not lead to such unexpected results, but showed the usual resistance decrease. These measurements were performed with similar sensors, which had been investigated at the AVL test bench. Therefore the unexpected results were most likely not caused by the sensing layer itself. The only difference between the two measuring setup was the new sensor mounting and therefore the heating of the gas flow. At AIT the sensor was integrated in a chip carrier including a heating plate. Therefore most probably the unexpected sensor response to H_2S was caused by an unknown reaction in the heated gas flow. Because the gas sensor temperature was monitored by a thermocouple close to the sensor, the possibility of a temperature divergence was eliminated.

Regardless of the unexplained sensor response the sensor sensitivity to hydrogen sulfide strongly varied due to the sensing material and the operating temperature. All measurements at 200°C showed a high noise level in the resistance signal and very low sensitivities of about 2%. The antimony doped sensor hardly showed any reaction to the presence of H_2S in the gas flow. The highest sensitivity to H_2S occurred at 300°C. The sensor containing pure SnO_2 conductive paths reached a maximum sensitivity of 73%. The doped sensors showed much smaller sensitivity values. A typical measurement with the SnO_2 sensor at 300°C is illustrated in Figure 5.9. In spite of the high sensitivity, the sensor response of SnO_2 at 300°C was very slow, with a response time of 240 sec.

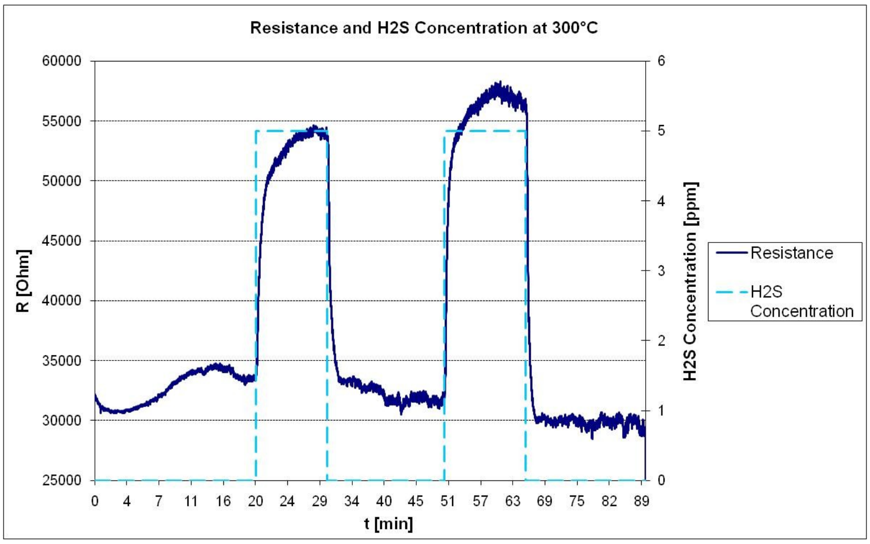

Figure 5.9: Sensor response to H_2S of pure SnO_2 sensor at 300°C

The indium doped sensor showed a smaller response time of 58 sec at 300°C, but the sensitivity was also much smaller than the one of pure tin dioxide. Sensitivity values, which could be evaluated and the response and recovery times of the different sensor materials at certain temperatures are compared in Figure 5.10 and Figure 5.11. Some of the sensor signals showed too much noise to identify the desired parameters. Therefore the values are missing in the comparison below.

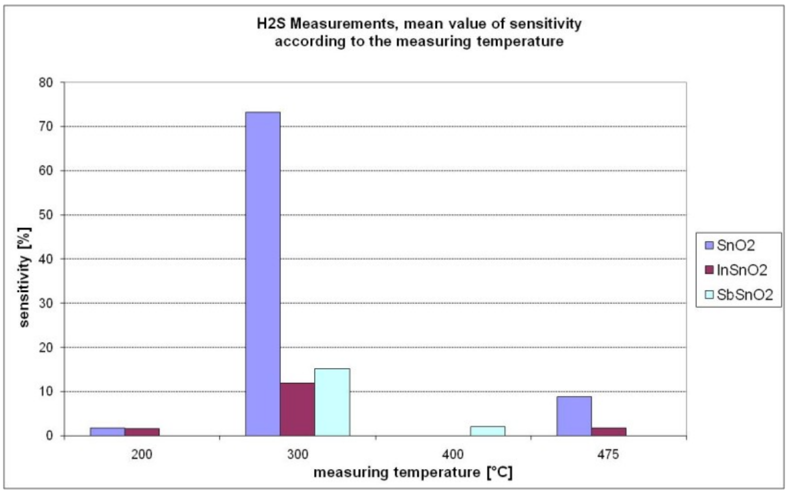

Figure 5.10: Mean sensitivity values of the three investigated SnO_2 sensors at different temperatures

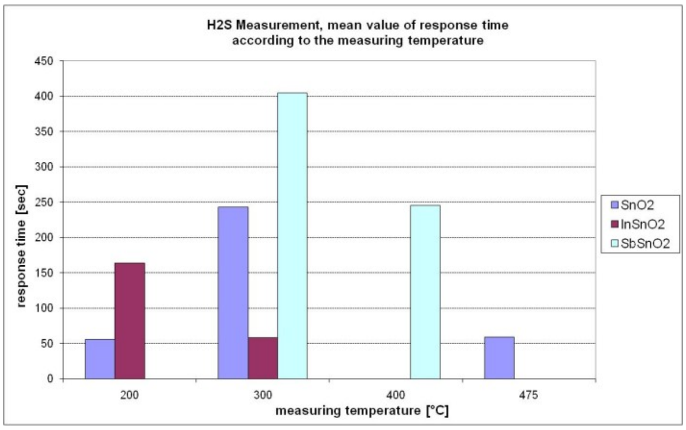

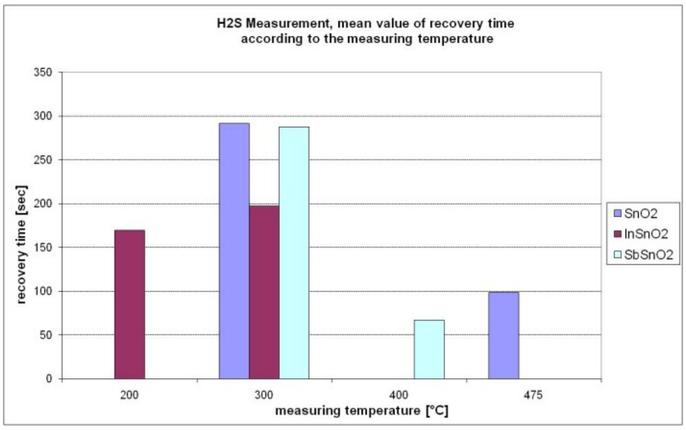

Figure 5.11: Mean response and recovery times of the three investigated SnO_2 sensors at different temperatures

The sensor response was clear and reproducible, even though the resistance increased. At a temperature of 400°C all sensors showed bad behavior. Although the signal was strongly drifting, again a resistance increases due to hydrogen sulfide could be detected. The sensitivity was extremely small and only reached 2%. The highest possible operating temperature during the measurements was 475°C. Tests at this temperature showed surprising results. Due to the high temperature a strong signal drift influenced the measurements. Maybe a certain annealing period at higher temperatures could have decreased this interference, like mentioned above. Because at 475°C the maximum temperature of the measurement setup was reached, it was not possible to perform an annealing at higher temperatures. Regardless of the drifting signal the sensors showed a clear response. Surprisingly at such high temperatures the expected resistance decrease due to the presence of hydrogen sulfide in the gas flow occurred. The detected sensitivities of all sensors were very small at 475°C. Pure SnO_2 reached the highest value of 8.8%. The best resistance signal at such high temperatures was achieved with this sensor and is illustrated in Figure 5.12.

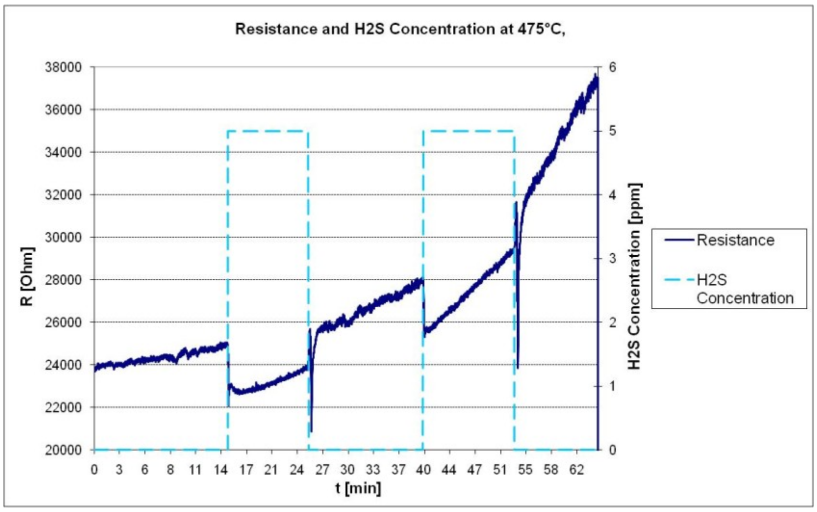

Figure 5.12: Sensor response to H_2S of pure SnO_2 sensor at 475°C

The short but strong decreases of the sensor resistance at the beginning of the flushing periods after the H_2S phases were caused by short temperature fluctuations. Our current state of knowledge does not enable a satisfying explanation for the unexpected behavior of all three tin dioxide sensors. Therefore further investigations will be necessary to define the unknown reaction in the heated H_2S gas flow.

5.4.2. H_2 measurements

In the course of the characterization measurements of the AIT tin dioxide sensors additional tests investigating the sensors sensitivity to hydrogen were performed. As 5% hydrogen in a nitrogen gas bottle was available at the low temperature AVL test bench, a short test series was carried out. These additional measurements were not possible during the testing period of the NTCW tungsten trioxide sensors, because the gas support had not been available. The hydrogen measurements were performed similar to the H_2S tests at 200°C, 300°C and 400°C. 1000 sccm/min nitrogen containing 5% H_2 were mixed with 1000 sccm/min synthetic air. Therefore a total hydrogen concentration of 2.5% was achieved. During the flushing periods the air was again mixed with pure nitrogen to guarantee a constant oxygen concentration of 10%. The measurement setup was kept similar to the one of the H_2S measurements. The only difference was the employment of the H_2/N_2 gas mixture instead of the H_2S/N_2 mixture.

Former measurements at AIT showed good sensor responses to H_2 with pure tin oxide as sensing material. Doping the sensing layer with antimony led to even better responses. Indium doped SnO_2 only showed very little resistance changes due to the presence of hydrogen. Due to the already known differences according the hydrogen sensitivity of the three different sensor materials it was not necessary to investigate all three sensor materials in the course of our H_2 measurements at the AVL test bench. Therefore only the sensor consisting of pure tin dioxide was investigated in hydrogen atmosphere.

The SnO_2 sensor signal showed definite reactions to the presence of 2.5% hydrogen in the gas flow. This time the sensor response to the reducing gas showed the expected behavior.

The sensor resistance decreased when H_2 was present at the sensor surface. The response time however was very slow at low temperatures (200°C and 300°C). According to the strong adsorption of H_2 at the SnO_2 surface it also took a long time to remove the hydrogen from the sensor during the flushing period, which leads to a long recovery time. Only when the temperature was increased up to 400°C the sensor showed a quick mean response time of 33 sec and a quite small mean recovery time of 198 sec. A mean sensitivity value of 32% could be evaluated. The according resistance developing is plotted in Figure 5.13.

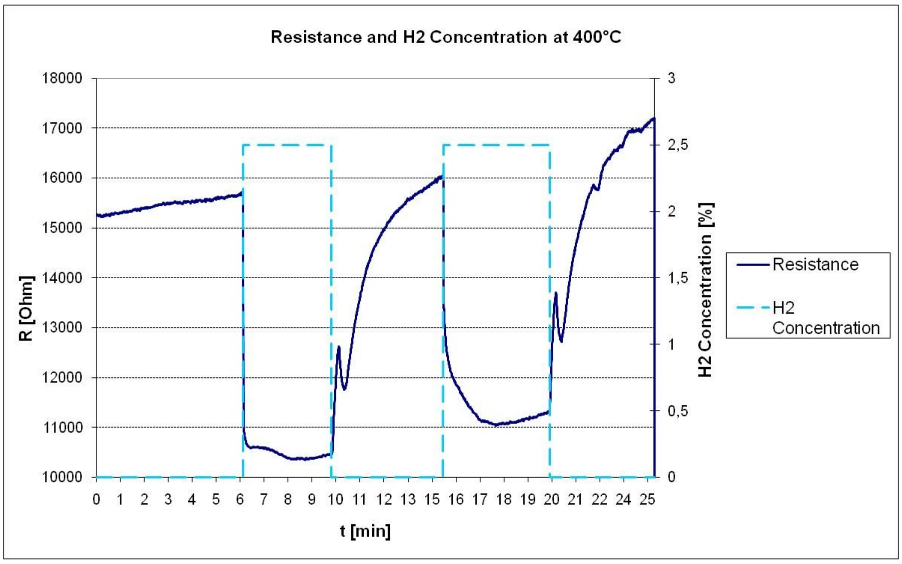

Figure 5.13: Sensor response to H_2 of pure SnO_2 sensor at 400°C

The peaks in the sensor resistance signal at the beginning of the flushing periods were caused by short temperature fluctuations. The additional hydrogen tests proved the suitability of tin dioxide chemiresistor gas sensors for the detection of H_2 in a gas flow. The sensor performance was strongly improved by high temperatures.

5.4.3. H_2O measurements

The characterization of tin dioxide sensors developed by AIT also included the detection of water in a humid gas flow. The tests were performed with a different water evaporator than during the measurements with the NTCW sensors. The new evaporator could not be used at such low gas flow rates. Therefore it was necessary to slightly increase the synthetic air flow rate from 2000 sccm/min up to 3000 sccm/min. This increase was still too small for an optimum performance of the evaporator, but larger values would have disabled the comparability with the water measurements performed with the NTCW sensors.

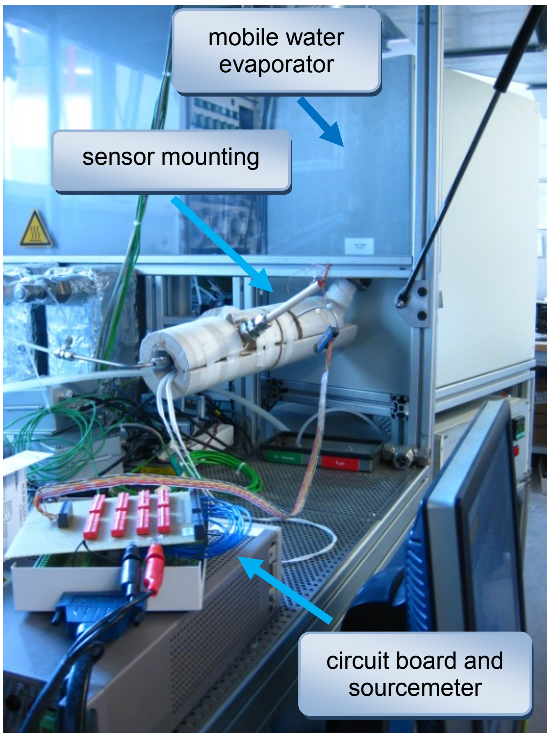

Figure 5.14: Measurement setup for water tests at the AVL test bench

According to the small synthetic air flow rate, temperature and also flow rate fluctuations occurred during the measurements. The possible water amount was limited by the water pump integrated in the low temperature test bench. The minimum pumping capacity was 7 ml/min. The maximum value produced during this characterization measurement was 10 ml/min. Generally the air and water parameters in this measurement setup were not ideal for an efficient operation of the employed water evaporator, which led to fluctuations of the resistance signal during the measurements.

Only the sensor containing pure SnO_2 was investigated in humid atmosphere. The tests were performed at 200°C, 300°C, 400°C and 470°C. Although former humidity measurements with similar SnO_2 sensors lead to good results at AIT, most tests at AVL were unsatisfactory. The sensor signal was strongly influenced by the fluctuating temperature and gas flow rate inside the evaporator. As the temperature dependence of the sensor resistance was unknown and the stability of the gas flow rate at the sensor could not be monitored, it was very difficult to identify the resistance changes due to changing amounts of water in the gas flow. The temperature changes on the other side were detected by the thermocouple next to the gas sensor. By considering the resistance values at a certain temperature in a diagram, it was possible to eliminate the temperature dependence of the sensor signal to some degree. The temperature compensated resistance only showed very small sensitivities to water. Two details of temperature compensated measurement data are illustrated in Figure 5.15. These details show the only reasonable results detected during the humidity tests. Concerning the measurement at 200°C a sensitivity value of about 4% could be detected.

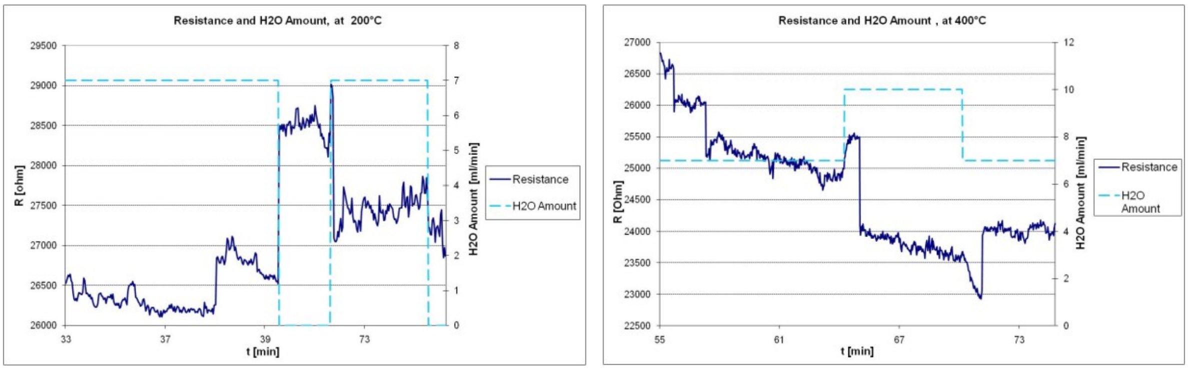

(a) (b)

Figure 5.15: Details of water measurements with pure SnO_2 sensor at (a) 200°C and (b) 400°C

In Figure 5.15(a) the increase of the sensor resistance is depicted, for a change of the water amount in the gas flow to zero. When 7 ml/min water was evaporated into the gas flow for a second time the resistance showed a small decrease, but as mentioned before the sensitivity was extremely low. The detail in Figure 5.15(b) shows an increase of the water amount from 7 ml/min up to 10 ml/min. A very small resistance decrease was detected due to the water increase. The two peaks at the beginning and the end of the 10 ml/min H_2O phase are most probably caused by gas flow rate fluctuations.

Generally the H_2O measurements of the tin dioxide sensor from AIT at the AVL test bench showed unsatisfactory results. Most tests led to unreasonable sensor signals according to varying operating temperatures and total gas flow rates. The suitability of tin dioxide chemiresistor gas sensors for the detection of H_2O in gas flows could therefore not be proved in the course of these measurements. Further tests with a more suitable water evaporator would be necessary to enable a definite statement about the sensitivity of SnO_2 sensors to water.

5.5. Frequency/temperature dependence of $GaPO_4$ resonators

The oscillation behavior of a piezoelectric microbalance is strongly influenced by the mounting and electrical contacting. A resonator oscillating in thickness shear mode must at least be fixed at two positions on opposite sides of the crystal to enable a current supply of the two electrodes. In most cases microbalances are mounted at these two points by clamping. In order to avoid any disturbance of the oscillation in the active area of the crystal, these two mounting positions are placed at the very edge of the disc resonator. Concerning the high temperature sensor mounting, developed by the Institute of Sensor and Actuator Systems (ISAS) of the Technical University in Vienna, the resonator was fixed at three positions on each crystal side. These positions were not located at the very edge of the crystal, but at half of the distance between the edge and the active area of the resonator. According to these facts a strong damping of the oscillation frequency due to the sensor mounting was expected. In order to verify the quality decreases of the mounted $GaPO_4$ resonators the equivalent circuit parameters, described in chapter 2.3.6, were evaluated with the help of a network analyzer. These characterizations were performed before and after the crystals were fixated in the sensor mounting. The quality values of the first crystals mounted by ISAS / TU Vienna are illustrated in Figure 5.16. The values were calculated by using the measured equivalent circuit parameters and equation 2.18. The first four sensors were fixed in the mounting by using the bump design, described in chapter 4.3.2. The other three crystals were mounted due to the micro sphere concept.

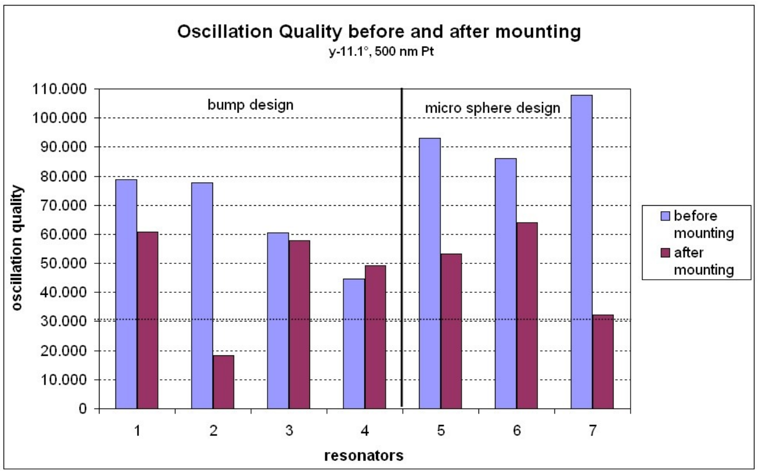

Figure 5.16: Quality values of the first resonators mounted by ISAS / TU Vienna before and after mounting

The oscillation quality of a piezoelectric crystal describes the relation between the resonant frequency and the band width of the signal. It also indicates the necessary energy input to enable a stable oscillation behavior. According to practical experiences, quality values higher than 30,000 guarantee very stable oscillation. Therefore this value was defined as threshold between good and bad sensor behavior. As can be seen in Figure 5.16, all sensors showed satisfying qualities before the mounting process. In most cases the expected quality decrease due to the sensor mounting did occur, but although the resonator qualities were clearly affected by the mounting, the decrease was much smaller than expected. Only in one case the oscillation quality fell beneath the limit of 30,000. The comparison of the two mounting concepts does not lead to any clear preference yet, although the quality decrease caused by the mounting process is much larger for the micro sphere approach. This effect may however occur due to the very high quality values before the assembly. Generally, the mounted crystals showed much better oscillation qualities than expected. The sensor elements produced in this way proved to be very capable for microbalance applications. Both mounting concepts enable stable oscillations at room temperature in air atmosphere.

According to the desired applicability of the sensor mounting at high temperatures, measurements investigating the sensor frequency during a heating process up to 800°C in air were performed. Therefore the assembled sensors were placed in the quartz tube of a laboratory furnace (LK 1100-70-500-1 by HTM Reetz GmbH). This furnace enables the generation of temperatures up to 1100°C. The sensor mounting was located at the edge of the furnace because the solder connections at the end of the ceramic substrates are not able to withstand temperatures higher than 250°C. As the top of the mounting was extended into the furnace, temperatures of 800°C could be achieved at the crystal.

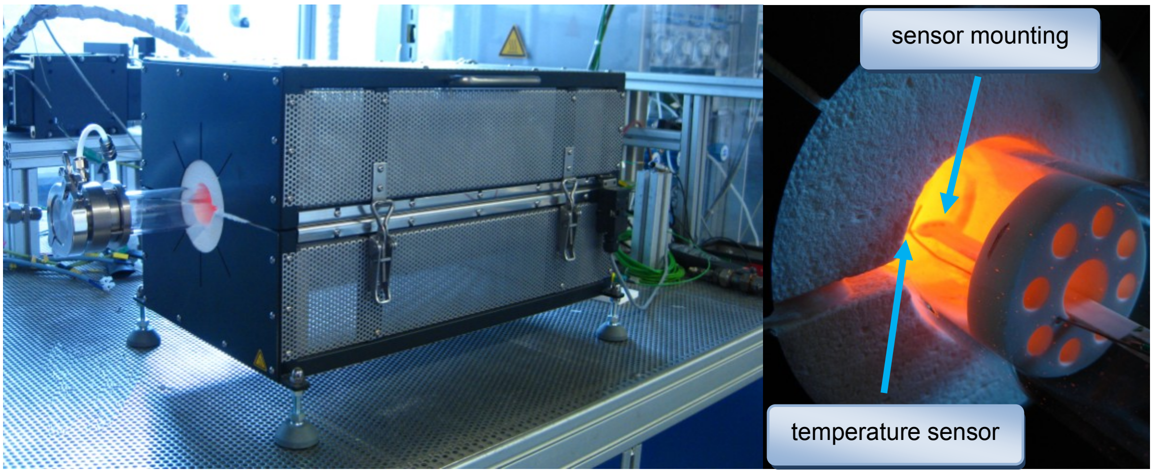

Figure 5.17: Laboratory furnace and quartz tube with integrated sensor mounting at 800°C

In order to monitor the temperature at the microbalance, a thermocouple was placed next to the sensor. The resonant frequency was detected by using an oscillator, a frequency counter and a LabVIEW data acquisition software. The laboratory furnace offers sealings at the end of the quartz tube. They include gas inlets in order to generate a certain atmosphere inside the tube. During our measurements one of these sealings had to be removed, because the thermocouple and the gas sensor had to be placed inside the tube. Therefore one end of the tube stayed open and the furnace was filled with air atmosphere at normal pressure.

Due to the fact that no sensor mounting, capable for such high temperatures, was available until now, the results of the heating process were of great interest. Generally, the resonant frequency of piezoelectric microbalances is strongly influenced by the operating frequency. To eliminate this distracting factor most microbalances operate at constant temperatures. If this solution is not applicable, it is necessary to know the exact temperature dependence of the frequency. By monitoring the sensor temperature with a thermocouple, the measured frequency can consequently be temperature compensated with suitable software. For this reason the detection of frequency temperature curves is very important in the field of microbalance applications. Concerning the disc shaped microbalances employed in this project, the temperature dependence had only been calculated. The measurements with the new sensor mounting generally showed very stable oscillations up to 800°C. A typical change of the oscillation frequency due to increasing temperature is illustrated in Figure 5.18.

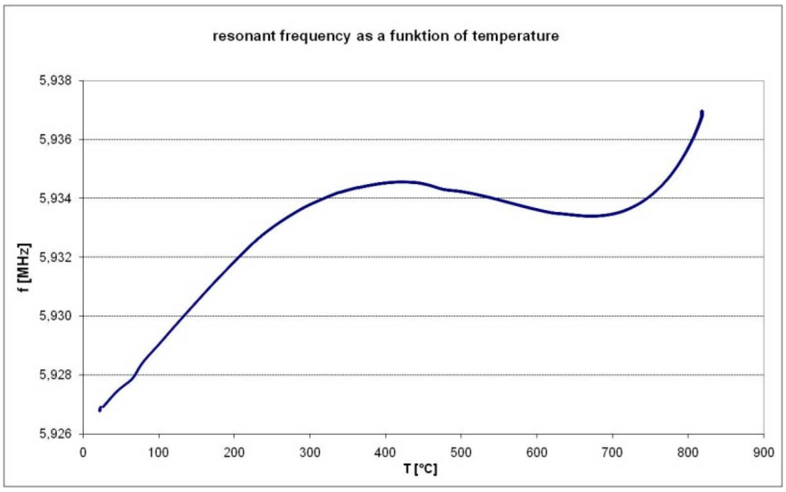

Figure 5.18: Temperature dependence of the resonance frequency of a Y-11.1° $GaPO_4$ microbalance

The heating process from room temperature up to 800°C caused a frequency change of about 10 kHz. As expected, the oscillation frequency of the microbalance is strongly influenced by temperature. At temperatures beneath 600°C the frequency showed a nearly parabolic behavior. This is usual for most microbalance cuts and geometries. Above 700°C the frequency increased again. Therefore the microbalance showed a quite stable oscillation frequency at operating temperatures between 300°C and 750°C. The frequency change in this region has a maximum value of just 1 kHz. The slight irregularities in the frequency signal at 70°C and 470°C are probably caused by spurious modes, appearing in these temperature regions. The measured data was compared with a calculated temperature dependence curve from Piezocryst and shows similar characteristics. This comparison is illustrated in Figure 5.19. Thereby delta f indicates the difference between all frequency values and the maximum position frequency value at about 400°C.

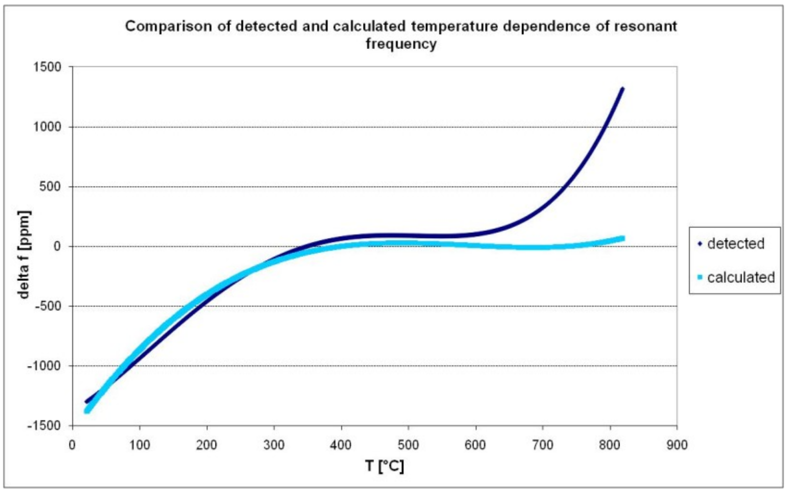

Figure 5.19: Comparison of detected and calculated frequency/temperature dependence

The calculated data also showed the parabolic behavior at the beginning and then indicates a further increase of the frequency. This calculated increase was smaller than it appeared in the measurements. Generally, the detected frequency change corresponds to the calculated one very well. Considering the frequency/temperature dependence of both mounting concepts no difference was detected. Both methods led to very stable frequencies at temperatures up to 800°C.

A second point of interest was the stability of the sensor mounting in reducing atmospheres at high temperatures. Therefore both mounting concepts were tested in the laboratory furnace, while the quartz tube was flushed with 2500 sccm/min nitrogen containing 5% H_2. The maximum temperature was limited at 700°C because of the instability of the platinum electrode layer of the microbalance at 800°C in reducing atmosphere, as discussed in chapter 4.3.1. Both mounting concepts led to stable frequency behaviors in reducing atmosphere at 700°C for several hours. The frequency/temperature dependence showed the same characteristics as in air. After several hours in reducing atmosphere it was planned to perform a third characterization with the network analyzer to identify the effect of reducing gases to the oscillation quality. This could only be realized with one sensor element, because all others could not be electrically contacted any more after the heating process. This single sensor showed a very bad oscillation behavior. The quality decrease could have been caused by contacting problems due to the mounting or by damages of the crystal during the heating process. In order to identify the appropriate factor an electron microscopic analysis was performed. Thereby a crack in the gallium orthophosphate resonator was detected. Figure 5.20 shows the top of the sensor mounting from the side. The green circle marks the position where the crystal is broken. Due to these results, the small oscillation quality after the heating tests was caused by a damage of the resonator. It will have to be investigated in further measurements, if all mounted crystals are exposed to destructive forces in the mounting at high temperatures.

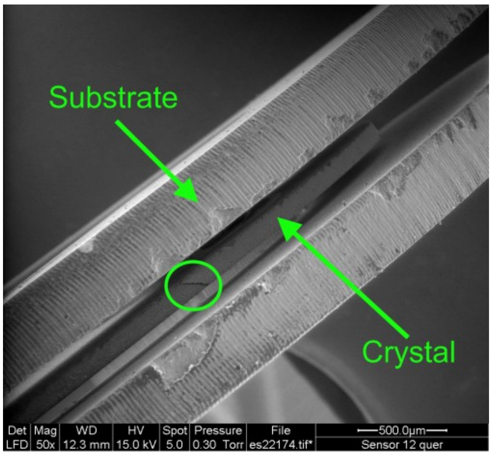

Figure 5.20: SEM picture of crystal assembled in sensor mounting (looked at from a side)

When the sensors were removed from the laboratory furnace, mechanical forces were applied to the solder connections at the end of the mounting substrates. Probably because of too high temperatures at the solder connections during the tests, the connected wires were removed unintendedly from the sensor mounting during handling. Therefore it was not possible to define the more suitable sensor mounting concept for measurements in reducing atmospheres yet. Additional measurements will be performed to produce enough information for a clear favoritism of one mounting concept. Therefore the solder connections will be strengthened by the additional use of an adhesive.

5.6. First tests with sensing nanolayers on microbalances

After the suitability of metal oxide nanolayers for the detection of hydrogen sulfide was proved during our characterization measurements, the next project step was the integration of gas sensitive nanolayers onto the high temperature microbalance of AVL. The first realization of this intention was the application of tungsten nanoparticles to the active area of the gallium orthophosphate resonators, without an electrical contacting of the sensing layer. It was expected that the tungsten trioxide would increase the adsorption of H_2S on the microbalance. Therefore a mass change due to adsorbed hydrogen sulfide molecules should become measureable. Electrodes where evaporated onto the crystals in the usual way and geometry. Due to the fact, that the NTCW tungsten trioxide sensors are using conductive paths made of gold under the nanoparticle layer, gold electrodes were applied to the microbalance instead of platinum ones. As mentioned in chapter 4.3.1, gold adheres very badly on $GaPO_4$. Therefore an additional nickel-chromium undercoating was necessary. These microbalances were sent to NTCW, where tungsten nanoparticles solved in isopropanol were applied by drop casting. In this first application process it was very difficult to define the most adequate amount of solution. Therefore the nanoparticles are not only located inside the active area, but in a bigger area in the middle of the crystal. Seven resonators were coated with nanoparticles in this way. Three of them were subjected to the annealing process at 500°C, which is performed routinely for the NTCW gas sensors. A WO_3 coated crystal after the annealing process is illustrated in Figure 5.21(b). In comparison to the unannealed resonators (a), the nanoparticle layer shows a green discoloration, which was probably caused by reactions between WO_3 and the gold electrodes at high temperatures.

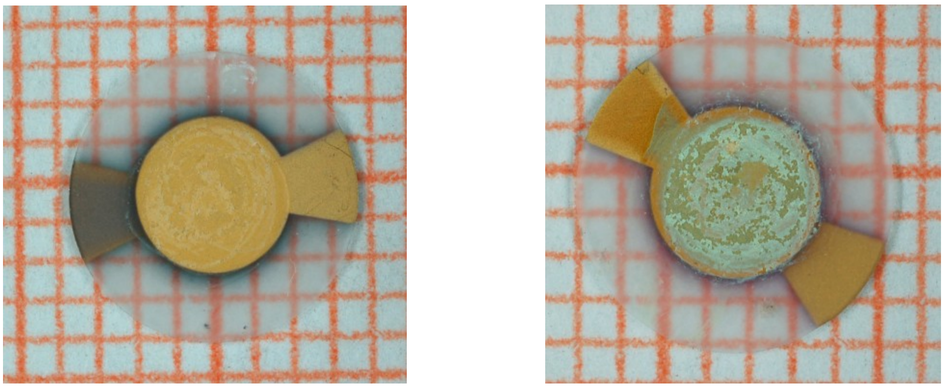
(a) (b)

Figure 5.21: Microbalances covered with WO_3 nanoparticles (a) before annealing and (b) after annealing

The coated resonators were investigated with a network analyzer in order to identify oscillation quality decreases due to the additional material. All crystals showed extremely bad oscillation behaviors. Therefore electron microscopic investigations of an unannealed and an annealed crystal were performed. This analysis showed a strong irregularity of the sensing layer thickness.

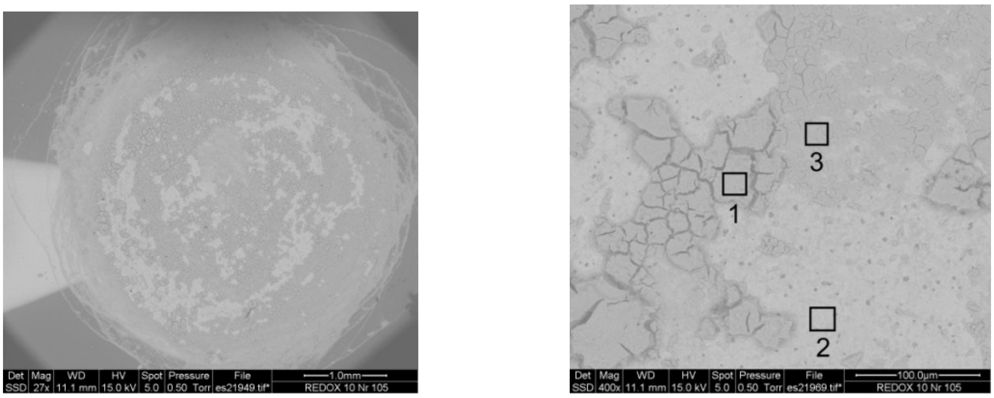

(a) (b)

Figure 5.22: SEM pictures of an annealed WO_3 layer on microbalance with (a) low and (b) high magnification

In Figure 5.22 (b) three different zones indicate the positions where EDX analysis was performed. The investigations showed different amounts of tungsten trioxide at the surface. While the tungsten concentration in zone 1 and 3 was very high, zone 2 showed a much higher amount of gold than of tungsten. Therefore the WO_3 layer in zone 2 has a much lower thickness than in the other two zones. Such an inhomogeneous coverage of the microbalance leads to bad oscillation behaviors and therefore explains the very low sensor qualities. The annealed and unannealed sensing layers showed the same inhomogeneities. In order to enable an accurate sensing behavior of tungsten trioxide coated microbalances, the coating method has to be modified.

6. Outlook

6.1. Improved electrode material for $GaPO_4$ resonators

To enable the deployment of gallium orthophosphate microbalances in reducing atmospheres at temperatures above 700°C, a new electrode material has to be developed. As described in chapter 4.3.1, platinum electrodes are very well suitable for such high temperatures in air, but not in reducing atmospheres. The resonator manufacturer Piezocryst is carrying out a lot of research in this field. New electrode materials will be tested on gallium orthophosphate crystals.

6.2. Ongoing measurements with chemical gas sensors

The scope of this work was too small to provide a total overview of the gas sensitive properties of the investigated chemical gas sensors. Further tests are necessary to characterize cross-sensitivities to other gas species included in fuel cell gas supplies, e.g. carbon monoxide. Since the adsorption of H_2 on tungsten trioxide sensors could not be tested in the course of this work, this process will be the topic of further measurements. Another interest lies in the capability of molybdenum trioxide nanoparticles as sensing material. Corresponding investigations will be performed as soon as an optimum MoO_3 sensor fabrication can be guaranteed. Additionally, the sensor response of all investigated materials to lower H_2S concentrations shall be proved because the application of the sensors in fuel cells demands the detection of at least 1ppm hydrogen sulfide. The sensor responses to water will also be a topic of further investigations in a new project phase. Sensitivities to H_2O could probably be detected under optimized test conditions.

6.3. Integration of gas sensitive nanolayers on $GaPO_4$ microbalances

In order to increase the selectivity of semiconductor chemical gas sensors by including the sensing method of a piezoelectric microbalance, gas sensitive materials will be applied on gallium orthophosphate resonators. The characterization measurements, described in chapter 4, proved the capability of the tungsten trioxide as H_2S sensing material. The behavior of SnO_2 in H_2S containing atmosphere will be investigated again during the next project steps.

At first, unstructured layers of WO_3 and SnO_2 will be created on the crystals active areas. They will not be contacted electrically. Measurements concerning the mass increase of the microbalance due to the adsorption of hydrogen sulfide at the gas sensitive layers will be performed. The application of tin dioxide will be achieved by AIT by using spray pyrolysis. At the moment, AIT is working on a mask to prevent the application of SnO_2 outside the active area of the resonator. Due to the fact, that coating of $GaPO_4$ crystals with tungsten trioxide did lead to a bad oscillation behavior, caused by very inhomogeneous WO_3 layers, the drop casting process has to be modified. Using special masks, the creation of thin films with almost homogenous thicknesses will be possible by performing spin coating after the drop casting. As the resonator surface outside the active area could not been covered by masks during the coating tests described in chapter 5.6., only drop casting was possible. A strong increase concerning the homogeneity of the WO_3 layer is expected according to the additional spin coating.

When the measurements concerning the mass changes due to adsorbed and desorbed hydrogen sulfide on microbalance surfaces are finished, gas sensitive layers will be applied to the resonators in the form of conductive paths. The high temperature sensor mounting, described in chapter 4.3.2, enables the electrical contacting of one nanolayer on each side of the crystal. The sensor elements will be investigated concerning the simultaneous detection of conductivity and mass changes due to adsorbed H_2S. These tests will prove if the integration of semiconductor gas sensitive nanolayers on piezoelectric microbalances leads to the expected selectivity increase.

6.4. Identification of optimum resonator mounting concept

According to the handling problems concerning the microbalance high temperature mountings, described in chapter 5.5, the optimum fixation method could not be identified yet. Further tests in reducing atmospheres at temperatures up to 700°C will show if the bump or the microsphere concepts lead to higher stabilities under harsh conditions. To prevent damages of the solder connections, these sensitive spots will be strengthened further by using adequate adhesives. Additionally, mountings including platinum conductive paths, instead of gold will be fabricated. This modification enables higher stability of the solder connections, but possibly leads to disadvantages at the fixation points at the crystals, because platinum shows a much smaller ductility than gold. Both methods to improve the mountings stability will be tested at AVL.

7. Summary

In order to protect fuel cell systems from the influence of hydrogen sulfide, this project was focused on the development of a highly sensitive, highly selective and rapid gas sensor. For this purpose, two different sensor designs fabricated by the Austrian Institute of Technology (AIT) and the NanoTecCenter Weiz (NTCW) where characterized at AVL under similar test conditions. Comparable results concerning the sensor response to H_2S and water were achieved. The operating temperature was between 100°C and 475°C during the measurements.

The chemical gas sensors consisting of WO_3 nanoparticles developed by NTCW showed very high sensitivities to hydrogen sulfide. A signal-to-background-ratio of 89% was achieved. Additionally, the sensor reaction was extremely rapid, with response times of about 7 sec. The miniaturized sensor geometry, with a conductive path width and spacing of 50 µm instead of 200 µm, showed much higher sensitivities at high temperatures. But the general validity of this observation has yet to be proved in further investigations. The sensor response to water showed unclear results. Additional to tungsten trioxide, sensors containing MoO_3 nanoparticles were investigated at AVL. But due to damages of the conductive path structure, the sensors could not be contacted electrically.

AIT developed chemical gas sensors made of SnO_2. Additionally to such a pure state sensor, also one indium doped and one antimony doped sensor was characterized at AVL. All these sensors showed unexpected but reproducible responses to H_2S which could not yet be explained. Instead of the expected sensor resistance decrease, a resistance increase due to the presence of hydrogen sulfide was detected. Most probably this behavior was caused by an unknown reaction of the gas components in the heated gas flow. This heating was necessary because the sensor mounting did not include a heating plate to generate the operating temperature directly at the sensor. Measurements in humid atmospheres showed only extremely small sensitivities of the three different SnO_2 sensors to H_2O. Additionally performed H_2 measurements lead to sensitivities of about 32% and short response times in the range of 33 sec. Due to the fact that the response time depends on the gas concentration, the values are not directly comparable with the response times to H_2S, but they generally demonstrate the capability of SnO_2 sensors for rapid H_2 detection.

Since the project includes the integration of the investigated nanolayers on piezoelectric microbalances and the application of these sensor elements at temperatures up to 800°C, a high temperature resonator mounting had to be developed. Tests with assembled piezoelectric crystals showed that the mounting only leads to very small decreases of the oscillation quality. These results were much better than expected. The new mounting enabled the detection of the frequency/temperature dependence of the resonators up to 800°C in air. The measured data strongly corresponds to the calculated temperature depending information. First tests in reducing gas atmospheres also showed very stable oscillation behaviors. Further tests will be necessary to guarantee the long time stability of the mounting concept in such harsh environments.

List of figures

Literature

[Alf08] D. Alfonso, *First-Principles studies of H_2S adsorption and dissociation on metal surfaces*, Surface Science 602 (2008) 2758-2768

[Dun06] J. K. Dunleavy, *Sulfur as a Catalyst Poison*, Platinum Metal Rev., 50 (2006) 110

[Fle00] M. Fleischer, S. Kornely, T. Weh, J. Frank, H. Meixner, *Selective gas detection with high-temperature operated metal oxides using catalytic filters*, Sensors and Actuators, B 69 (2000) 205-210

[Fra04] J. Fraden, *Handbook of Modern Sensors*, Springer-Verlag New York (2004)

[Gal03] I. J. Gallardo, *Tungsten oxide nanocrystalline powders for gas sensing applications*, Dissertation, University of Barcelona (2003)

[Gie05] M. Giesen, H. Ibach, (L. Bergmann, C. Schäfer), *Lehrbuch der Experimentalphysik – Festkörper*, Walter de Gruyter Berlin New York (2005)

[Gon04] J. Gong, Q. Chen, W. Fei, S. Seal, *Micromachined nanocrystalline SnO_2 chemical gas sensors for electronic nose*, Sensors and Actuators, B 102 (2004) 117-125

[Han06] C.-H. Han, S.-D. Han, S.P. Khatkar, *Enhancement of H_2-sensing properties of F-doped SnO_2 sensors by surface modification with SiO_2*, Sensors 6 (2006) 492-502

[Iva00] M. Ivanovskaya, P. Bogdanov, G. Faglia, G. Sberveglieri, *The features of thin film and ceramic sensors at the detection of CO and NO_2*, Sensors and Actuators, B 68 (2000) 344-350

[Kas05] R. Kassing, (L. Bergmann, C. Schäfer), *Lehrbuch der Experimentalphysik – Festkörper*, Walter de Gruyter Berlin New York (2005)

[Kau07] M. Kaur, D. K. Aswal, J. V. Yakhmi, (D. K. Aswal, S. K. Gupta), *Science and Technology of Chemiresistor Gas Sensors*, Nova Science Publishers New York (2007)

[Kiu57] K. Kiukkola, C. Wagner, Journal of Electrochemical Society 105 (1957) 387

[Kri09] T. Krishnakumar, R. Jayaprakash, et al., *Sb-SnO_2-nanosized-based resistive sensors for NO_2 detection*, Journal of Sensors, Article ID 980965 (2009) 7

[Liu03] J. Liu, X. Huang, G. Ye, et al., *H_2S detection sensing characteristic of CuO/SnO_2 sensors*, Sensors, 3 (2003) 110-118

[Ma05] X. Ma, S. Velu, J. H. Kim, C. Song, *Deep desulfurization of gasoline by selective adsorption over solid adsorbents and impact of analytical methods* *on ppm-level sulfur quantification for fuel cell applications*, Applied Catalysis, B 56 (2005) 137-147

[Mad89] M. Madou, S. Morrison, *Chemical Sensing with Solid State Devices*, Academic Press Inc. San Diego (1989)

[Mei27] A. Meissner, Über piezoelektrische Krystalle bei Hochfrequnez, Z. Tech. Phys., 8(74) (1927)

[Mic10] Micronova Center of Micro and Nanotechnology, Url: http://micronova.tkk.fi/files/Micronova%20Seminar%202005/Gas%20Sensors.pdf, dated as of 2010

[Neu97] B. Neubig, W. Briese, *Das Quarzkochbuch*, Franzis-Verlag (1997)

[Nit76] T. Nitta, J. Terada, *Ceramic Humidity Sensitive Resistor Device*, National Tech. Rept. 22 (1976) 885-894

[Our03] K. Oura et al., *Surface Science*, Springer Verlag (2003)

[Par02] C. O. Park, S. A. Akbar, J. Hwang, Selective gas detection with catalytic filters, Material, Chemistry and Physics, 75 (2002) 56-60

[Pie10] Piezocryst Advanced Sensorics GmbH, *Piezoelectric Materials*, Url: http://www.piezocryst.com/piezoelectric_materials.php, dated as of 2010

[Poh00] R. Pohle, *In-Situ-Untersuchungen gassensitiver Prozesse an Metalloxidoberflächen mit infrarotspektroskopischen Methoden*, Dissertation, Technical University München (2000)

[Pos09] M. Postl, *Untersuchungen an gassensitiven Sensoren basierend auf durch Mikrowellen-Plasma-Synthese (MPS) hergestellten nano-skaligen Oxidschichten*, Diploma Thesis, Technical University Graz (2009)

[Rai99] W. Raith, (L. Bergmann, C. Schäfer), *Lehrbuch der Experimentalphysik – Elektromagnetismus*, Walter de Gruyter Berlin New York (1999)

[Ren94] K. D. Rendulic, A. Winkler, *Adsorption and desorption dynamics as seen through molecular beam techniques*, Surface Science 299-300 (1994) 261-276

[Rey06] L. Reyes, A. Hoel, S. Saukko, P. Heszler, V. Latto, C. Granqvist, *Gas sensor response of pure and activated WO_3 nanoparticle films made by advanced reactive gas deposition*, Sensors and Actuators, B 117 (2006) 128-134

[Sau59] G. Sauerbrey, Verwendung von Schwingquarzen zur Wägung dünner Schichten und zur Mikrowägung, Zeitschrift für Physik 155 (1959) 206-222

[Sei62] T. Seiyama, A. Kato, K. Fujiishi, M. Nagatani, *A New Detector for Gaseous Components Using Semiconductive Thin Films*, Anal. Chem. 34 (1962) 1502-1503

[Sun04] Y. Sun, X. Huang, F. Meng, J. Liu, *Study of influencing factors of dynamic measurements based on* SnO_2 *gas sensor*, Sensors, 4 (2004) 95-104

[Tag62] N. Taguchi, Puplished Patent Application in Japan, S37-47677 (1962)

[Weh00] T. Weh, M. Fleischer, H. Meixner, *Optimization of physical filtering for selective high temperature* H_2 *sensors*, Sensors and Actuators, B 68 (2000) 146-150

[Wei89] Ch. Weißmantel, C. Hamann, *Grundlagen der Festkörperphysik*, VEB Deutscher Verlag der Wissenschaften Berlin (1989)

[WiM10] Wikipedia, the free encyclopedia: *Molybdenum Trioxide*, Creation Date: Unknown, Url: http://en.wikipedia.org/wiki/Molybdenum_trioxide, dated as of 2010

[WiP10] Wikipedia, the free encyclopedia: *Piezoelectricity*, Creation Date: Unknown, Url: http://en.wikipedia.org/wiki/Piezoelectricity, dated as of 2010

[WiT10] Wikipedia, the free encyclopedia: *Tungsten Trioxide*, Creation Date: Unknown, Url: http://en.wikipedia.org/wiki/Tungsten_trioxide, dated as of 2010

[WiV10] Wikipedia, die freie Enzyklopädie: *Vier-Punkt-Methode*, Creation Date: Unknown, Url: http://de.wikipedia.org/wiki/Vier-Punkt-Methode, dated as of 2010

[Yam07] N. Yamazoe, K. Shimanoe, (D. K. Aswal, S. K. Gupa), *Science and Technology of Chemiresistor Gas Sensors*, Nova Science Publishers New York (2007)

Deutsche Fassung:
Beschluss der Curricula-Kommission für Bachelor-, Master- und Diplomstudien vom 10.11.2008
Genehmigung des Senates am 1.12.2008

EIDESSTATTLICHE ERKLÄRUNG

Ich erkläre an Eides statt, dass ich die vorliegende Arbeit selbstständig verfasst, andere als die angegebenen Quellen/Hilfsmittel nicht benutzt, und die den benutzten Quellen wörtlich und inhaltlich entnommene Stellen als solche kenntlich gemacht habe.

Graz, am …………………………… ………………………………………………..
(Unterschrift)

Englische Fassung:

STATUTORY DECLARATION

I declare that I have authored this thesis independently, that I have not used other than the declared sources / resources, and that I have explicitly marked all material which has been quoted either literally or by content from the used sources.

…………………………… ………………………………………………..
date (signature)